THREE-DIMENSIONAL ANALYSIS OF WAVE ATTENUATION BY ANCHORED HEMICYLINDRICAL SHELL

by

Fata D.E. Dewi

Thesis submitted to the Faculty of the

Virginia Polytechnic Institute and State University

in partial fulfillment of the requirements for the degree of

Master of Science

in

Ocean Engineering

APPROVED:

_____	_____
Dr. Stergios I. Liapis, Chairman	Dr. Raymond H. Plaut, Co-Chairman

_____

Dr. Wayne L. Neu

August, 1997

Blacksburg, Virginia

Keywords: Breakwater, Inflatable, Vibration, Wave

THREE-DIMENSIONAL ANALYSIS OF WAVE ATTENUATION BY ANCHORED HEMICYLINDRICAL SHELL

Fata D.E. Dewi

(ABSTRACT)

The performance of a flexible structure as a breakwater is investigated numerically. The structure is a hemicylinder and is filled with water of uniform pressure. It is anchored along the sides. Only flexural modes are present.

The structure is modeled as an elastic shell using the finite element program ABAQUS. The fluid is assumed to be inviscid and incompressible. The fluid flow is analyzed using a boundary integral method and the integral equation is solved numerically by a panel method.

The vibration characteristics of the structure are analyzed both in the absence and presence of water. The hydrodynamic coefficients, forces, and the dynamic response of the structure in waves are obtained as a function of the wave number. Two different water depths of 5 m and 6 m are considered. For each water depth, normal and oblique incident waves are considered. The free surface elevation in front of and behind the structure is evaluated for different wave frequencies and directions. The results indicate that the flexible structure is effective in reducing the incident wave intensity over a wide range of frequencies.

ACKNOWLEDGEMENTS

I would like to thank those who helped to make this work possible:

- Dr. Liapis and Dr. Plaut for their advice, guidance and patience in this research and thesis,
- Dr. Neu for being on my graduate committee,
- my research group, Guruprasad Mysore and Jeremy Trowbridge, for their tremendous help and support,
- the System Administrator of the Aerospace and Ocean Engineering Department, Josh Durham, for his assistance and cooperation with the computer,
- my family and friends for their constant encouragement.

I also want to acknowledge the financial support from the National Science Foundation under Grant No. BES-9521425.

TABLE OF CONTENTS

LIST OF FIGURES

LIST OF TABLES

CHAPTER 1 INTRODUCTION

1.1 MOTIVATION

In view of the increasing number of activities in the ocean environment, the role of breakwaters has become more significant. Built to break the force of the waves, breakwaters can stop beach erosion as well as damage to a harbor. Presently, most existing breakwaters are fixed rigid structures such as the rubble-mound breakwater.

In this study we will investigate the use of inflatable, flexible structures as breakwaters. The use of inflatable structures for breakwaters has a number of advantages. First, they have relatively low cost and little weight compared to rigid structures. Their cost does not increase substantially with depth, while the cost of a fixed structure increases exponentially with depth. Second, they are relatively easy to install, do not corrode, require little maintenance, and can handle extreme temperatures. Third, they can be filled with air, water, or a combination of air and water which can be done in a relatively short time, so they can be efficient in assembly and disassembly. Fourth, they are easily transportable because, when deflated, the inflatable structures can be compressed into a small volume. Lastly, inflatable breakwaters can be anchored to the ocean floor and inflated only in the event of a severe storm. This is an attractive alternative to a fixed breakwater, since in calm weather the inflatable structures are deflated and will not obstruct marine life or navigation.

Recent developments in materials science have contributed significantly to opening an opportunity for the development of flexible, inflatable structures as breakwaters. Problems of material degradation and failure have been largely overcome. With the use of modern materials, inflatable structures might be extremely effective as breakwaters, absorbing or reflecting much of the wave energy.

In the present day of ocean exploration, inflatable breakwaters can also support a number of operations at sea, such as oil and gas extraction, fish farming, ocean mining, and recreation. These structures can also be used to protect floating airports or portable ports and to support temporary operations such as pollution control, salvage operations, and construction and maintenance of offshore platforms. In addition, inflatable breakwaters can alternatively act as sacrificial structures in the event of large storms, reducing the size of waves incident on fixed breakwaters, shores, or offshore structures.

1.2 HISTORY

According to archaeological work, a sea-wall or breakwater was a common feature in many Egyptian, Greek, and Roman ports. During the Roman Empire, numerous breakwaters were constructed because of the scarcity of natural bays that could be formed into harbors. The remains of these breakwaters have been found and they resemble the present-day rubble mound breakwaters.

Contrary to the old concept of fixed breakwaters for coastal protection, the idea of transportable breakwaters is more recent. The most famous use of this type of breakwater was during the Normandy invasion of World War II, where the Bombardon floating breakwater and the Phoenix caisson were deployed to form artificial harbors. These structures performed well and their failures were caused by unexpected waves 5 m high which produced stresses eight times greater than those of the design loads.

Other innovative designs of transportable breakwaters include the scrap tire floating breakwater (where tires are chained to form a breakwater that can reach 600 m in length), a single floating pontoon moored to the bottom, multiple pontoons, and floating membrane, sheet, or blanket structures that can be filled with air, water, or a viscous

liquid. The merits of these designs have been discussed by Jones (1971), Hales (1981) and Jenkins and Leonard (1991).

Pirelli, an Italian tire company, have proposed the use of rubber structures to protect Venice, Italy, from periodic flooding due to high tides. These structures would be attached to the bottom of the channels. In the event of a storm, they would be inflated with water thus protecting the historic city (Scott, 1976). Unfortunately, these tidal barriers have not yet been constructed because of economic considerations, and Venice continues to be flooded during high tides.

1.3 INFLATABLE DAMS

The research effort on the potential use of inflatable structures as breakwaters was inspired by research studies done on inflatable dams. These dams can be used in many applications such as: diversion of water for irrigation, hydroelectricity, tidal control, or flood control; raising the height of fixed dams to increase reservoir capacity; creating recreational basins; preventing contamination; and increasing groundwater supply.

Typically, inflatable dams are cylindrical in shape and are used as low-rise dams, not exceeding a 6 m height. The length to height ratios can vary, ranging from 0.5 to 229. The dams can be filled and inflated with air, water or a combination of both. These dams may be anchored to a specifically made reinforced-concrete foundation strip or an existing base, e.g. the crest of a dam or a breakwater. Anchorage can be a single or a double strip system.

The early dams were called Fabridams, manufactured by Firestone (Firestone Tire and Rubber Company, 1964; Firestone Coated Fabrics Company, 1968). A few failures of these early dams were caused by the low durability of the structure, the small

thickness of the material and the anchoring system that was not well developed, i.e. the dam was anchored by bolts which made holes in the rubber, causing stretching to occur at the bolts.

Most of the newer dams are built by two Japanese companies, Sumitomo Electric Industries and Bridgestone Corporation. These more developed dams have material thickness that ranges from 4 to 23 mm. They are made of rubber, reinforced with several layers of a synthetic fiber such as nylon. Sometimes, ceramic chips are embedded in the lamination to increase the strength of the outer resistance of the structure. The manufacturers claim that these dams have an expected lifetime of 30-40 years.

1.4 PRESENT STUDY

The proposed inflatable breakwater has the shape of a half circular cylinder. It is anchored to the ocean floor and filled with water. The structure is totally submerged at a small distance beneath the free surface. The three-dimensional motions of the structure are analyzed and the flexibility of the structure is described using a finite element numerical model. The linear fluid-structure interaction was investigated numerically by computing the wave field around the structure. The effects of three-dimensionality and flexibility of the structure on the reflected and transmitted waves were investigated, and the structural performance as a breakwater was analyzed over a range of wave frequencies. It was found that the flexible structure as a breakwater is very effective in reducing the wave amplitude over a wide range of wave frequencies.

The material in this thesis will be presented in the following manner. Chapter 2 describes previous research studies on the interaction of waves with rigid and flexible structures. Next, in Chapter 3, the mathematical formulation of the boundary value problem is discussed. Chapter 4 contains the validations performed on the finite element

software ABAQUS and on the fluid program used for computing the wave field around the structure. Chapter 5 discusses the results of the investigation on the effectiveness of the proposed inflatable breakwater. Conclusions and suggestions for further research are presented in Chapter 6. The figures and tables are presented at the end of each chapter.

CHAPTER 2 LITERATURE REVIEW

This chapter is divided into two sections. First, earlier works on the dynamics of free surface waves over a rigid structure beneath the free surface will be discussed briefly. The second section will describe previous analytical, experimental and numerical works on the interaction of flexible structures and water waves.

2.1 INTERACTION OF SURFACE WAVES WITH SUBMERGED OBSTACLES

The dynamics of ocean surface waves is a topic that has been studied extensively. Some of the well known results are contained in the books by Dean and Dalrymple (1991), Mei (1992) and Sorensen (1993). When analyzing the problem of surface waves over rigid obstacles, the viscous effects are usually neglected. Therefore, the flow is analyzed using potential flow theory.

Newman (1965) obtained an approximate solution for surface waves elevation in the limit of a long submerged obstacle. Kobayashi and Wurjanto (1989) obtained the approximate solution in the limit of long waves.

Mei and Black (1969) presented numerical results on the investigation of the scattering of waves by rectangular obstacles in two dimensions using a variational formulation. Similarly, Williams and Darwiche (1988) analyzed the three-dimensional scattering of waves by elliptical breakwaters using eigenfunction expansions. The numerical results from both works are valid for the entire wavelength spectrum and finite obstacle lengths.

Subcritical and supercritical solutions for surface waves over circular bumps were given by Shen, et al. (1989).

Chakrabarti and Naftzger (1989) evaluated the wave forces on a submerged semi-cylinder resting on the bottom using a boundary integral method. The non-dimensional horizontal and vertical forces were obtained at different values of the wave number.

In all of these works, the nonlinear effects are neglected, that is the free surface boundary condition is linearized. A recent study by Grue (1992) on the diffraction of waves by a slightly submerged obstacle or a bottom topography showed that nonlinearity is important. For the submerged obstacles, horizontal circular cylinders of radius 100 mm and 200 mm were used. For the bottom topography, a rectangular shelf with a cross section 500 mm long and 410 mm high was used. All geometries, the circular cylinders and the rectangular shelf, span the whole width of the wave channel of 14.2 m long and 0.47 m wide where the experiments were performed. Grue's study showed that nonlinearity can introduce subharmonic waves which can carry up to 25% of the incoming energy flux.

2.2 FLEXIBLE STRUCTURES AND SURFACE WATER WAVES

Fluid-filled floating bags, wave blankets, fluid-filled circular cylinders and flexible underwater mounds are examples of flexible structures used for wave control. Their effectiveness in reducing wave intensity is due to structural damping which absorbs energy, or structural motions generating waves that may cancel the incoming waves.

Ohyama, et al. (1989) performed a numerical and experimental study of the transmission and reflection characteristics of waves over a submerged flexible mound. The structure was modeled as a thin flexible membrane filled with water. It was fixed on the

seabed and the water inside the membrane was hermetically sealed. In the numerical analysis, the flexible membrane was modeled as a lumped-mass system and was discretized equally in the initial condition without stretching. The fluid was assumed to be incompressible, inviscid and irrotational so that the velocity potential could be used to describe the fluid motion. Linear theory was applied, assuming that the membrane and the fluid motion were sufficiently small. The boundary value problems were formulated and transformed into boundary integral equations using Green's function and Green's formula that satisfies the boundary conditions on both the free surface and the seabed. Equations of motion were written for each nodal point on the membrane, containing the mass of the element, density of the membrane's material, membrane's thickness, and hydrostatic and hydrodynamic forces. The unknowns, i.e. the potential values and the displacement magnitudes at nodal points and the potential values at any arbitrary point in the fluid region, were found by solving the linear equations of motion. The results of the numerical analysis were validated against experimental results.

Ohyama, et al. (1989) tested a model of a flexible mound in a wave tank 40.0 m long and 4.0 m wide. The model was made of a rubber membrane with Young's modulus = 58,000 kN/m^2, ρ_m = 1260 kg/m^3 and material thickness = 1.65 mm. It had a base width of 1.6 m and breadth of 4.0 m. The height of the flexible mound was varied. The water depth was 0.8 m and the incident wave height was 4.0 cm. The reflected and transmitted wave heights were recorded at three points along the membrane's length. The transmission and reflection coefficients obtained from the numerical analysis and experiments agreed well, except at wave periods where reflection and transmission coefficients become maximum and minimum, respectively. It was stated that the discrepancies were caused mainly by the influence of the side membrane. The wave periods at which the coefficients differed significantly may be the natural periods of the structure; then the response motion is amplified considerably and differs from the two-dimensional motion. In this case, the numerical analysis is no longer valid. It was found that at several wave periods, the

transmission coefficient was zero. At these wave periods, the radiation waves had the same height but inverse phase as those of the transmitted waves when the structure was not moving. It was also observed that the stationary component of the internal pressure increased considerably from the initial added pressure under the action of waves. If this internal added pressure was adequate, the flexible membrane was effective in reducing the transmitted waves over a wide range of wave frequency.

Fathi, et al. (1994) studied the interaction between free-surface waves and a floating flexible container. Three-dimensional linear potential theory (Newman, 1994), which will be discussed extensively in Chapter 3, was used to solve the radiation-diffraction problem. The container was modeled as a circular cylinder with spherical caps at the ends. A total length of 30.48 m and a diameter of 1.46 m were used to give a length to diameter ratio of approximately 20. Several hydroelastic mode shapes were added to the conventional six rigid body modes to account for the motion of the container. Natural modes for a uniform beam with free ends were chosen for these hydroelastic mode shapes. An infinite depth was used for the analysis and the structural behavior was assumed to be linear and elastic. A panel program named WAMIT was used to compute the amplitude of the motions, the exciting forces and the hydrodynamic coefficients (added mass and damping coefficients) for specified modes. One of the important results was that the response amplitudes of the generalized modes (i.e. hydroelastic modes) are largest for the first bending mode and decrease with increasing order.

Evans and Linton (1989) showed that a submerged body, allowed to move subject to a restoring force, could reduce the wave intensity by utilizing the body's induced motion to generate waves which exactly canceled the incident waves. Assuming the body and its motion to be symmetric, this cancellation of waves could be accomplished without adding energy or taking energy out of the system if the velocity of the moving body was chosen such that the incident waves were totally reflected. Theoretical

calculations were performed for a submerged circular cylinder held down by two inextensible cables at each end. The transmission coefficients for varying incident wavelength were obtained at three different submergence levels. It was found that the performance of the structure improved as its distance to the free surface was reduced (e.g. at a clearance of 1/3 of its radius, the circular cylinder reflected 95% of the incident wave energy over a very wide range of wavelengths). For a given specific gravity, the "tuned" frequency (i.e. the frequency at which the body totally reflected the incident wave) was discovered to be a function of the length of the cables and the water depth. At this tuning frequency, the free surface profile showed that there were no transmitted waves downstream. The maximum displacement of the cylinder, which occurred at a wavelength longer than the tuned wavelength, was found to be slightly over twice the incident wave amplitude. This relatively large displacement was stated to be necessary for the submerged body to generate canceling waves. An experimental study was carried out on a polystyrene cylinder of 51 mm radius and specific gravity of 0.06 which confirmed these theoretical predictions.

Broderick and Leonard (1992) studied the nonlinear interaction between a highly deformable fluid-filled membrane and surface water waves. The finite element model of the membrane was used to predict its nonlinear dynamic behavior such as large displacements, surface rotations, nonlinear stress-strain relationships and non-conservative loadings. The boundary element method was used to model the fluid domain and to compute the hydrodynamic loading induced by water waves on the structure. Ideal fluid flow was assumed in solving the diffraction/radiation problem. To treat the nonlinear kinematic and dynamic free surface boundary conditions iteratively, either linear waves or finite amplitude waves were assumed in the boundary element model. Volterra's method was used to include time implicitly in the governing field equations. The finite element model and the boundary element model were coupled and an iterative procedure was utilized to investigate the wave-structure interaction. Numerical calculations of the

reflection and transmission coefficients showed that the membrane cylinder can be an effective wave barrier for certain wave periods. The membrane's effectiveness as it moved closer to the free surface was not evaluated. A circular cylinder of 3-ft diameter and 12-ft length was used in the experimental study to verify the numerical results.

CHAPTER 3 LINEAR ANALYSIS: FORMULATION

The analysis is divided into two parts. First, the structure is modeled using a finite element program. It is assumed that initially the structure is filled with water until the hydrostatic pressure of the internal water is equal to that of the external water. At this point, the structure has an exact semi-cylindrical shape because the internal pressure is canceled by the external one. Then, more water is added into the structure until the internal pressure is uniformly 5% higher than the maximum external hydrostatic pressure. This pressure addition is treated as air pressure and is included in obtaining the vibration frequencies and mode shapes. These mode shapes are called the "dry" mode shapes.

Second, the "dry" mode shapes of the structure are used as basis functions to describe the displacement of the body surface. Then, the effects of internal and external added mass are included in the analysis.

3.1 WITHOUT EXTERNAL AND INTERNAL WATER

The governing equations of motion for this analysis have the form:

$$M\ddot{U} + KU = 0 \tag{3.1}$$

where $U(t)$ is the vector of the nodal displacements and M and K are, respectively, the mass and stiffness matrices of the structure. The matrices M and K are real, symmetric and positive definite. The numerical values of the mass matrix are obtained from the finite element software ABAQUS (Hibbitt, et al., 1994) along with the vibration frequencies and mode shapes. The "dry" natural frequencies ω_{dry} satisfy:

$$\left| K - \omega_{dry}^2 M \right| = 0 \tag{3.2}$$

For the ABAQUS analysis, a shell element S4R (4-node doubly- curved thin or thick shell) is chosen. This element allows large deflections, large rotations and small

strains. Each node of the element has six generalized displacements ($u, v, w, \theta_1, \theta_2\ \theta_3$), resulting in a total of 24 degrees of freedom per element (see Fig. 3.1).

3.2 WITH EXTERNAL WATER AND INTERNAL WATER

The fluid is assumed to be inviscid and incompressible. The fluid motion is assumed to be irrotational, so that we can write the velocity field as the gradient of a velocity potential Φ. A linear analysis is used in which the boundary conditions on the free surface and the body boundary are linearized.

A coordinate system is defined such that z is positive upwards and the xy-plane is coincident with the bottom surface (see Fig. 3.2.a). Incident waves will interact with the submerged body, causing it to have small vibrations about the equilibrium position. It is assumed that the body motion is sinusoidal at the radial frequency ω of the waves with displacement $\xi(t) = \hat{\xi}\, e^{-i\omega t}$. In general, the body can have both rigid and flexural motions. For this configuration, only the flexural modes are present. In this study, the "dry" mode shapes $S_j(\vec{x})$ with Cartesian components (u_j, v_j, w_j) are used as basis functions to describe the displacement of the body surface. Other choices of basis functions to define the flexural displacement include orthogonal polynomials such as Chebychev or Legendre polynomials (Newman, 1994). We then approximate the displacement γ at any point of the body surface as:

$$\gamma(x, y, z, t) = \sum_{j=1}^{J} \xi_j(t)\ S_j(x, y, z) \tag{3.3}$$

The governing equations of motion can be written as:

$$\left(M_g + A + A_{\text{internal}}\right)\ddot{\xi} + B\dot{\xi} + K_g\,\xi = F^I + F^D \tag{3.4}$$

where

- $\xi(t) = \{\xi_j(t)\}$ is the $J \times 1$ vector the nodal displacement factors,
- A and B are the added mass and damping matrices, respectively, which represent the influence of the external water,
- $J = 15$ is the total number of flexural modes used in the analysis,
- A_{internal} is the added mass matrix due to the internal water,
- F^I and F^D are the hydrodynamic forces due to the incident and diffracted waves, respectively,
- M_g and K_g are, respectively, the generalized modal mass and modal stiffness matrices obtained from ABAQUS. M_g and K_g are diagonal and $(K_g)_{ii} = (\omega^2_{dry})_i \ (M_g)_{ii}$.

The velocity potential can be decomposed into:

$$\Phi(x, y, z, t) = \text{Re}\left[\left(\phi_I + \phi_D + \sum_{j=1}^{J} \phi_j(x, y, z)\, \hat{\xi}_j\right) e^{-i\omega t}\right] \tag{3.5}$$

where

- $\phi_D \, e^{-i\omega t}$ is the potential of diffracted waves,
- $\phi_j \, e^{-i\omega t}$ is the radiation potential for mode j,
- $\hat{\xi}_j$ is the complex amplitude of body motion in the j^{th} mode, $\xi_j(t) = \hat{\xi}_j \, e^{-i\omega t}$,
- $\phi_I \, e^{-i\omega t}$ is the potential of incident waves, defined as (Newman, 1994):

$$\phi_I = \frac{igA_{\text{incident}}}{\omega} \frac{\cosh(k\,z)}{\cosh(k\,d)} \, e^{ik(x\cos\beta + y\sin\beta)} \tag{3.6}$$

where

- A_{incident} is the incident wave amplitude,
- d is the water depth,

- ω is the incident wave frequency ($\omega = \frac{2\pi}{T}$),
- k is the wave number, defined to be a positive root of the dispersion relation:

$$\frac{\omega^2}{g} = k \tanh(kd) \tag{3.7}$$

- β is the angle of wave propagation (see Fig. 3.2.b).

In order to solve equation (3.4), we need to determine the fluid flow outside the structure as well as inside the structure.

In the external fluid domain, each of the potentials ϕ_j must satisfy Laplace's equation, $\nabla^2 \phi_j = 0$. On the fluid boundaries, the following linearized boundary conditions must be satisfied (see Fig. 3.3):

- On the mean water surface, $z = d$: $\quad -\frac{\omega^2}{g}\phi_j + \frac{\partial \phi_j}{\partial z} = 0 \qquad j = 1,2,\ldots, J$
- On the bottom: $\quad \frac{\partial \phi_D}{\partial z} = 0, \qquad \frac{\partial \phi_j}{\partial z} = 0$
- On the body surface, S_b : $\quad \frac{\partial \phi_D}{\partial n} = -\frac{\partial \phi_I}{\partial n}$

$$\frac{\partial \phi_j}{\partial n} = -i\omega n_j \qquad j = 1,2,\ldots, J$$

where $n_j = S_j . \vec{n} = u_j n_x + v_j n_y + w_j n_z$ and the unit normal $\vec{n} = \left(n_x, n_y, n_z\right)$ points out from the body surface to the external fluid domain.

The exterior fluid flow is analyzed using a boundary integral method. The appropriate Green's function for this problem, which is the potential of a submerged source of oscillatory strength in water of depth d (Wehausen and Laitone, 1960), is written as:

$$G(P,Q)=\frac{1}{\sqrt{R^2+(z-\zeta)^2}}+\frac{1}{\sqrt{R^2+(2d+z+\zeta)^2}}+ \tag{3.8}$$

$$2\int_0^\infty \frac{\left(k+\frac{\omega^2}{g}\right)\cosh k(z+d)\cosh k(\zeta+d)}{k\sinh(kd)-\frac{\omega^2}{g}\cosh(kd)}\, e^{-kh} J_0(kR)\, dk$$

where

- $P=(x,y,z)$ is the coordinate of the field point,
- $Q=(\xi,\eta,\zeta)$ is the coordinate of the source point,
- $R=\sqrt{(x-\xi)^2+(y-\eta)^2}$.

Application of Green's second identity provides a Fredholm equation of the second kind for the values of the potential on the body surface:

$$-2\pi\phi_j(P)+\iint_{S_b}\phi_j(Q)\frac{\partial G(P,Q)}{\partial n_Q}\, dS_Q=\iint_{S_b}\frac{\partial \phi_j}{\partial n_Q}(Q)\; G(P,Q)\; dS_Q \tag{3.9}$$

The integral equation is solved numerically by a panel method in which the body surface is approximated by an ensemble of flat quadrilateral panels and the value of the potential is assumed to be constant over each panel. This assumption reduces the problem of finding a continuous potential distribution to determining a finite number of unknown potential strengths. Utilizing a collocation method in which the integral equation is satisfied at one point for each panel, the problem is reduced to solving a linear system for the values of the velocity potential on each panel.

The efficient calculation of the Green's function G defined by equation (3.8) is central to the effectiveness of the present numerical method. In order to analyze each

structure, the program needs 10^8 to 10^9 Green's function evaluations The subroutine FINGREEN developed by Newman (1985) was used to evaluate the Green's function.

The incident wave potential ϕ_I and the diffracted wave potential ϕ_D are used to find the hydrodynamic force:

$$F_i^I + F_i^D = -i\omega\rho_w \iint_{S_b} (\phi_I + \phi_D) n_i \, dS \tag{3.10}$$

where $\rho_w = 1025.9$ kg/m^3 is the density of water. For the vertical and horizontal forces, equation (3.10) can be written as follows:

$$F^I_{\text{horizontal}} + F^D_{\text{horizontal}} = -i\omega\rho_w \iint_{S_b} (\phi_I + \phi_D) n_x \, dS \tag{3.11}$$

$$F^I_{\text{vertical}} + F^D_{\text{vertical}} = -i\omega\rho_w \iint_{S_b} (\phi_I + \phi_D) n_z \, dS \tag{3.12}$$

The radiation potentials ϕ_j provide the values of the added mass and damping matrices A and B as follows:

$$[A]_{ij} = \frac{1}{\omega^2} \text{Re}\left(-i\omega\rho_w \iint_{S_b} \phi_j n_i \, dS \right) \tag{3.13}$$

$$[B]_{ij} = \frac{1}{\omega} \text{Im}\left(-i\omega\rho_w \iint_{S_b} \phi_j n_i \, dS \right) \tag{3.14}$$

For the internal fluid analysis, each of the potentials ϕ_j must satisfy Laplace's equation, $\nabla^2\phi_j = 0$, in the fluid domain. On the fluid boundaries, the following linearized boundary conditions must be satisfied (see Fig. 3.4):

- On the bottom: $\dfrac{\partial \phi_j}{\partial z} = 0$
- On the body surface, S_b : $\dfrac{\partial \phi_j}{\partial n} = -i\omega n_j \qquad j = 1,2,\ldots,J$

The internal fluid flow is also analyzed using a boundary integral method as discussed previously for the analysis of the external fluid flow. A Rankine source Green's function is chosen for this problem:

$$G(P,Q) = \frac{1}{\sqrt{R^2 + (z-\zeta)^2}} \tag{3.15}$$

where P, Q and R are as defined earlier.

Application of Green's second identity provides a Fredholm equation of the second kind for the values of the potential on the body surface as written in equation (3.9). The values of the internal added mass are obtained from equation (3.13). There is no damping.

The amplitudes $\hat{\xi}_j$ of the structural response are obtained by solving equation (3.4). Then the flexural displacement of a point on the surface of the structure is determined from equation (3.3). Green's theorem gives the values of the velocity potentials ϕ_j on the free surface:

$$\phi_j(P) = \frac{1}{4\pi} \iint_{S_b} \left[\phi_j(Q) \frac{\partial G(P,Q)}{\partial n_Q} - G(P,Q) \frac{\partial \phi_j(Q)}{\partial n_Q} \right] dS_Q \tag{3.16}$$

The total potential Φ is determined from equation (3.5). Given the values of the velocity potential on the free surface, the free surface elevation is found as:

$$\zeta = -\frac{1}{g} \frac{\partial \Phi}{\partial t} = \frac{i\omega \Phi}{g} \tag{3.17}$$

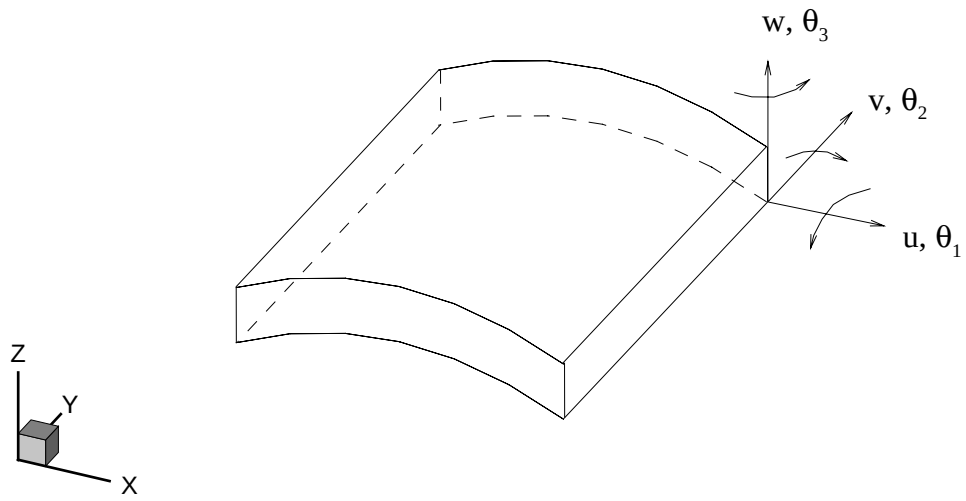

Figure 3.1 A shell finite element.

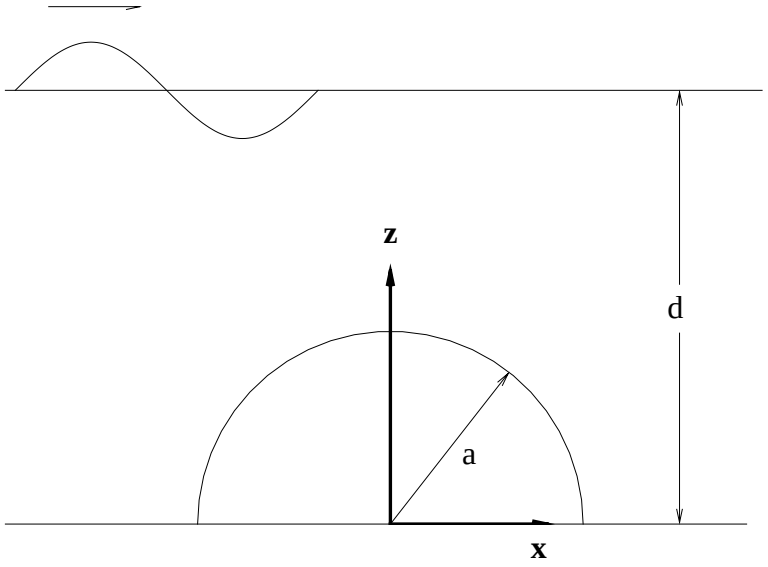

Figure 3.2.a Schematic diagram of the coordinate system.

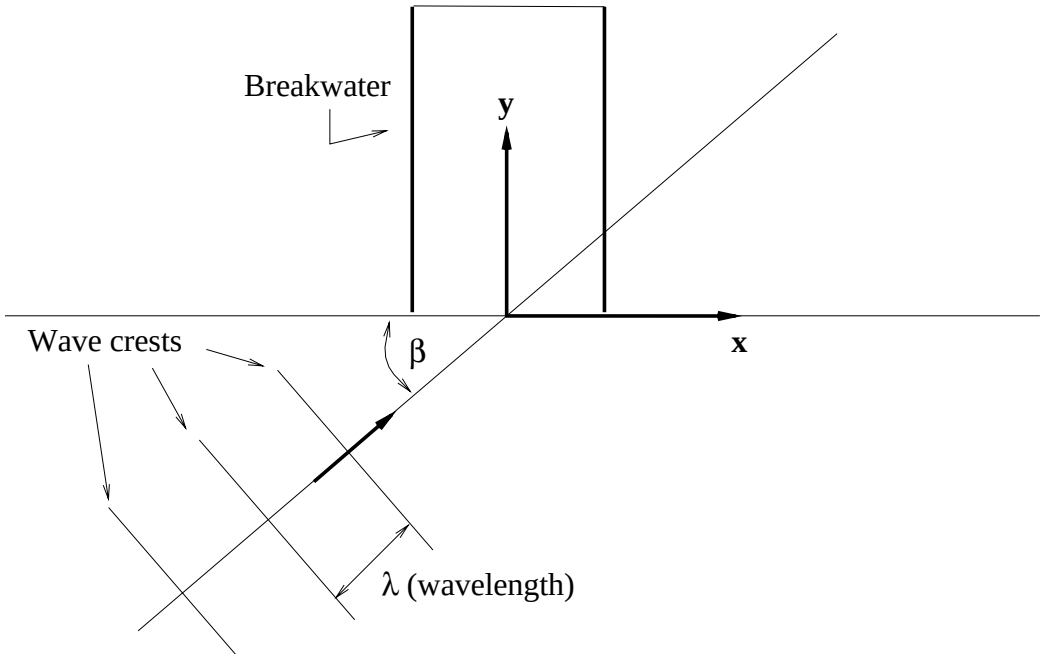

Figure 3.2.b Definition of incident wave direction of propagation.

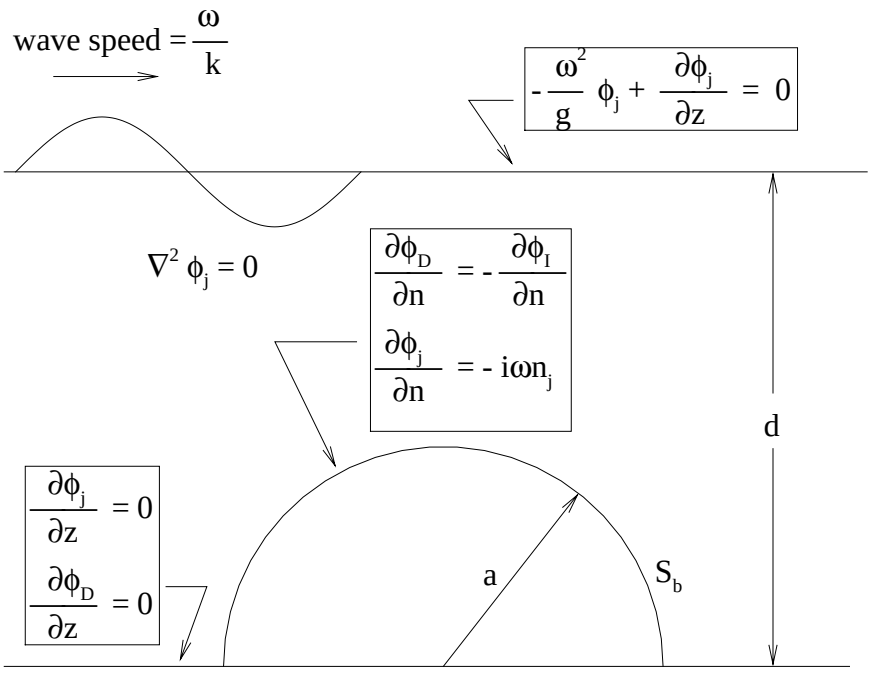

Figure 3.3 Linearized boundary conditions for external fluid analysis.

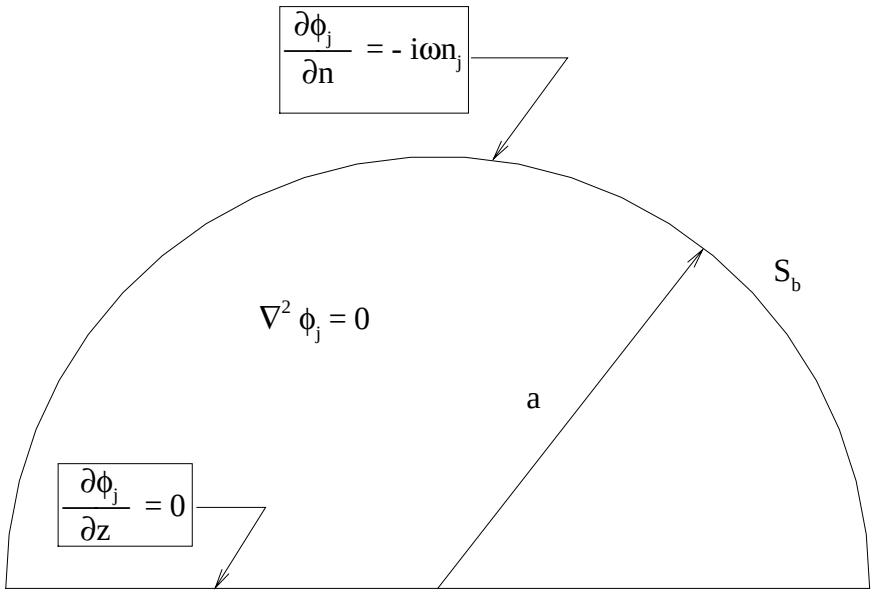

Figure 3.4 Linearized boundary conditions for internal fluid analysis.

CHAPTER 4 PROCEDURE VALIDATIONS

This chapter is divided into two sections. Section 4.1 describes the verifications that were performed on the finite element software ABAQUS which is used to find the vibration characteristics of the structure without the presence of external water. Section 4.2 explains the validation of the fluid-flow program which is used to determine the effects of external water on the structure.

4.1 WITHOUT EXTERNAL WATER

In this research, the finite element software ABAQUS (Hibbitt, et al., 1994) is used to model the breakwater structure. From ABAQUS, we obtain:

- the vibration frequencies and mode shapes of the structure,
- the numerical values for the mass and stiffness matrices of the structure.

In order to validate ABAQUS's analysis on a structure's vibration characteristics, several 2-D and 3-D structures were modeled and their vibration characteristics were obtained.

4.1.1 2-D STRUCTURE

Analytical solutions for the vibration frequencies of clamped and pinned circular arches can be found in Chidamparan and Leissa (1993). Using ABAQUS, we modeled a half circular arc segment (Fig. 4.1) and obtained the vibration frequencies. The radius of the arc was 4 m and it was modeled by 100 quadrilateral panels of shell element S4R. The following boundary conditions were applied to the model:

- no translation in the y-axis direction and no rotation about the x- and z-axes for all nodes,
- the nodes at the ends of the arc were either clamped or pinned.

The first four vibration frequencies obtained from ABAQUS were non-dimensionalized and compared to those obtained by Chidamparan and Leissa (1993). These vibration frequencies are presented in Table 4.1 (for the clamped arc) and Table 4.2 (for the pinned arc). For the clamped arc, the largest difference is 6.5% at mode number 3, while for the pinned arc, the maximum difference is 14.2% at mode number 3. These diferences may be attributed to the number of panels used for ABAQUS analysis.

Moorthy, et al. (1995) performed a finite element analysis of the vibration frequencies of a two-dimensional dam structure (Fig. 4.2) with the following characteristics:

- $E = 2.1 \times 10^9$ N/m^2
- $\nu = 0.3$
- $\rho = 960$ kg/m^3
- h = 7.6 mm
- perimeter = 13.7 m
- height = 4.9 m
- base length = 6.1 m

In ABAQUS, we modeled the 2-D dam structure with 100 quadrilateral panels of shell element S4R (Fig. 4.3). The following boundary conditions were applied to the structure:

- the nodes at the structure's ends are pinned,
- no translation in the y-axis direction and no rotation about the x- and z-axes for all nodes.

A uniform internal pressure of 28 kPa was applied to the structure and the natural vibration frequencies of the structure were obtained. Table 4.3 shows the first six vibration frequencies obtained by Moorthy, et al. (1995) and those obtained from ABAQUS. The values agree fairly well, with the largest difference being 13.6% for mode

number 2. These differences may be attributed to the following : Moorthy, et al. used a 9-node shell element to model the structure, while the ABAQUS analysis used a 4-node shell element.

4.1.2 3-D STRUCTURE

The vibration characteristics of a three-dimensional dam have been studied numerically by Moorthy, et al. (1995). The cross-section of this 3-D dam structure was described in the previous section (Fig. 4.2). In ABAQUS, we modeled the 3-D dam as a 40 m long structure using 980 quadrilateral panels of shell element S4R (Fig. 4.4). A uniform internal pressure of 28 kPa was applied to the structure. The boundary conditions were applied to the structure in the following manner:

- all nodes at the structure's ends (y=0 and y=L) are clamped,
- all nodes along the sides parallel to the y-axis are pinned.

Table 4.4 contains the values of the vibration frequencies from the previous study and from ABAQUS. It can be seen that ABAQUS's frequencies are higher than those of Moorthy, et al. (1995). The largest difference is 16.9% for mode number 3. Similar to the 2-D structure, the difference may be caused by the number of nodes in the shell element.

From Soedel (1993), the frequency of an open circular cylindrical shell is written as follows:

$$\omega_{mn}^2 = \frac{E}{\rho a^2}\left\{\frac{\left(\frac{m\pi a}{L}\right)^4}{\left[\left(\frac{m\pi a}{L}\right)^2+\left(\frac{n\pi}{\alpha}\right)^2\right]^2}+\frac{h^2}{12(1+\nu)a^2}\left[\left(\frac{m\pi a}{L}\right)^2+\left(\frac{n\pi}{L}\right)^2\right]^2\right\} \qquad (4.1)$$

where m and n are the numbers of half waves in the axial and circumferential directions, respectively. The following parameters were used for ABAQUS's analysis:

- $E = 103.425 \times 10^6$ N/m^2
- $\nu = 0.499$
- $\rho = 1000$ kg/ m^3
- $h = 13$ mm
- $L = 40$ m
- $\alpha = 180^0$
- $a = 4$ m

The ABAQUS model of the structure is shown in Fig. 4.5. It has 500 quadrilateral panels of shell element S4R. The following boundary conditions were applied:

- no translation in the radial and circumferential directions and no rotation about the radial and axial axes for all nodes at the four corners and all nodes at the structure's ends (y=0 and y=L),
- no translation in the radial and axial directions and no rotation about the circumferential axis for all nodes along the sides parallel to the y-axis (except the corner nodes).

Table 4.5 presents the first eight frequencies obtained from equation (4.1) and from the finite element analysis using ABAQUS. Number of panels used for ABAQUS analysis may contribute to the discrepancies between the two results. The largest difference is 11.6% for mode number 3. The corresponding vibration mode shapes obtained from ABAQUS are presented in Fig. 4.6 and Fig. 4.7.

4.2 WITH EXTERNAL AND INTERNAL WATER

The fluid-flow code computes the added mass and damping matrices, the hydrodynamic forces and the wave elevation. Verifications of each of these output variables were performed to validate the program.

4.2.1 HYDRODYNAMIC FORCE VALIDATION

Chakrabarti and Naftzger (1989) evaluated the wave-induced horizontal and vertical forces on a rigid hemicylinder resting on the bottom using a boundary integral method. The same problem (see Fig. 4.8) was analyzed numerically using the present method. A hemicylinder of 100 m length and 4 m radius was modeled for the program using 1072 quadrilateral panels (Fig. 4.9). Other input variables for the program are listed below:

- wave amplitude, 0.5 H = 1 m,
- water depth, d = 12.68 m,
- ρ_w = 1025.9 kg/m^3,
- g = 9.80665 m/s^2.

The results from Chakrabarti and Naftzger (1989) and the computed hydrodynamic forces from the fluid-flow code are plotted in Fig. 4.10 and Fig. 4.11. These plots show that the hydrodynamic forces computed from the fluid-flow code compare well with the results from Chakrabarti and Naftzger (1989).

4.2.2 ADDED MASS VALIDATION

Kwak and Kim (1991) performed an analytical study on the axisymmetric vibration of circular plates in contact with fluid (Fig. 4.12). In their study, the added virtual mass incremental factor (β) was defined as the ratio of the kinetic energy of the fluid due to the motion of the plate to the kinetic energy of the plate itself :

$$\beta = \frac{T_f^*}{T_p^*} = \Gamma \left(\frac{\rho_w}{\rho_p} \right) \left(\frac{a}{h} \right) \tag{4.2}$$

where ρ_w is the density of the fluid, ρ_p is the mass density of the plate and, respectively, *a* and *h* are the radius and the thickness of the plate. Kwak and Kim (1991) calculated the values of the non-dimensionalized added virtual mass incremental (NAVMI) factor, Γ, for circular plates vibrating axisymmetrically on the free surface. For circular plates vibrating axisymmetrically submerged in the fluid, the NAVMI factor should be multiplied by 2. The same problem was analyzed using the fluid-flow code. We obtained the added mass values for a simply supported vibrating circular plate of radius 1 m, thickness 13 mm and mass density 960 kg/m^3 submerged in water of 40 m depth. The added virtual mass incremental factor is calculated from:

$$\beta = \frac{T_w^*}{T_p^*} = \frac{0.5 \int_s (M_A + m_p)\, \omega_n^2\, \psi_n^2(s)\, ds}{0.5 \int_s m_p\, \omega_n^2\, \psi_n^2(s)\, ds} \tag{4.3}$$

where ω_n is the natural vibration frequency of the plate, ψ_n is the vibration mode shape (Fig. 4.13 and Fig. 4.14), M_A is the dimensional added mass and m_p is the generalized mass of the plate for a specific mode shape. Since the vibration mode shapes in the water change very little compared to those in the air, $\beta = \frac{M_A + m_p}{m_p}$. The values of Γ are calculated accordingly from equation (4.2) and the results from both studies are compared and presented in Table 4.6 for six vibration frequencies. As Table 4.6 indicates, the agreement is very good with the maximum difference being 6.89% for $\omega_{dry} = 124.27$ rad/sec.

4.2.3 DAMPING AND RESPONSE AMPLITUDE VALIDATION

We verified the values of damping due to the influence of fluid indirectly by verifying the response amplitudes $\hat{\xi}_j$. The result of Newman's (1994) analysis on bending of a vertical column (see Fig. 4.15) was used for comparison. With reference to Newman's study, we used an identical vertical circular cylinder of radius 10 m extending the entire depth of 200 m. It has a constant bending stiffness, EI, and a uniform distribution of mass m along its length. A concentrated mass m_o is placed at the free surface to account for the 'superstructure'. The concentrated mass is equal to the total displaced mass, $m_o = \rho_w \pi a^2 d$, and the distributed mass is defined to be half of its displaced mass, $m = 0.5\rho_w \pi a^2$. The stiffness of the cylinder is defined such that $EI / d^3 = 0.41 m_o \sec^{-2}$. A set of orthogonal polynomials was used to define the "dry" vibration mode shapes of the vertical cylinder (Fig. 4.16). These polynomials are defined as follows (Newman, 1994):

$$f_j(z) = q^2 P^*_{j-1}(q), \qquad j = 1,2,3,\ldots \tag{4.4}$$

where $q = \frac{z}{d}$ and P^*_j is a polynomial of degree n defined as:

$$P^*_n(q) = \sum_{m=0}^{n} (-1)^m \frac{(4+2n-m)!}{m!(n-m)!(4+n-m)!} q^{n-m} \tag{4.5}$$

The governing equations for the linear system are defined as follows:

$$\sum_j \xi_j \left[-\omega^2 (a_{ij} + M_{ij}) + i\omega b_{ij} + C_{ij} \right] = X_i \tag{4.6}$$

The values of added mass a_{ij}, damping b_{ij} and hydrodynamic forces X_i were obtained from the fluid-flow program and are listed below for a wave period of 6.5 sec:

$$[a_{ij}] = 10^6 \times \begin{bmatrix} 10.07 & -1.31 & -0.27 & 0.007 \\ -1.31 & 7.81 & -0.525 & 0.04 \\ -0.27 & -0.526 & 5.94 & -0.402 \\ 0.005 & 0.04 & -0.402 & 4.49 \end{bmatrix}$$

$$\left[b_{ij}\right] = 10^6 \times \begin{bmatrix} 3.87 & 2.76 & 1.76 & 1.00 \\ 2.77 & 1.97 & 1.26 & 0.71 \\ 1.77 & 1.26 & 0.80 & 0.46 \\ 1.00 & 0.72 & 0.46 & 0.26 \end{bmatrix}$$

$$\left\{X_i\right\} = 10^6 \times \begin{Bmatrix} 1.403 - 3.793\,i \\ 1.002 - 2.703\,i \\ 0.641 - 1.723\,i \\ 0.365 - 0.976\,i \end{Bmatrix}$$

The values of M_{ij} and C_{ij} were given (Newman, 1994) as follows:

$$\left[M\right]_{ij} = md\,\frac{\delta_{ij}}{2i+3} + m_0 \tag{4.7}$$

$$\left[C\right]_{ij} = \left(EI / d^3\right) \begin{bmatrix} 4 & 16 & 32 & 52 \\ 16 & 172 & 380 & 640 \\ 32 & 380 & \frac{7356}{5} & \frac{12496}{5} \\ 52 & 640 & \frac{12496}{5} & \frac{220652}{35} \end{bmatrix} \tag{4.8}$$

Solving equation (4.6), we obtained the response amplitudes ξ_j for wave periods 5.0, 6.5 and 7.0 sec as presented in Table 4.7.

4.2.4 WAVE AMPLITUDE VALIDATION

There are only a few exact analytical solutions for diffraction (scattering) of waves due to the presence of a sufficiently large body in the water. One of these solutions can be found in Mei (1992) for the problem of wave diffraction by a vertical cylinder of circular cross section which extends from the sea bottom to the free surface. In this case, the free-surface displacement is given by:

$$\eta = A_{\text{incident}} \sum_{m=0}^{\infty} \varepsilon_m (i)^m \left\{ J_m(kr) - H_m(kr) \frac{J'_m(ka)}{H'_m(ka)} \right\} cos(m\theta) \tag{4.9}$$

where

- A_{incident} is the amplitude of the plane incident wave, r is the distance between any point on the free surface and the origin of the coordinate system and a is the radius of the cylinder,
- $\varepsilon_0 = 1$ and $\varepsilon_m = 2,\ m = 1,2,3,\ldots,$
- $J_m(kr)$ are Bessel functions of the first kind,
- $H_m(kr) = J_m(kr) + i\,Y_m(kr)$, where $Y_m(kr)$ are Bessel functions of the second kind,
- $J'_m(ka) = -\,J_{m+1}(ka) + \dfrac{m}{ka} J_m(ka)$ and $H'_m(ka) = -\,H_{m+1}(ka) + \dfrac{m}{ka} H_m(ka)$

A vertical cylinder of 1 m radius and of 5 m height (Fig. 4.17), discretized into 1000 quadrilateral panels, was used as an input geometry for the fluid-flow code. The free-surface displacements were obtained from equation (4.9) and from the fluid-flow code using an incident wave amplitude 1 m and different values of the wave number, k. Fig. 4.18 and Fig. 4.19 show the wave amplitude on the cylinder surface (r = a). The solid line was obtained from equation (4.9) while the circles are numerical results from the program. Fig. 4.20 shows the wave amplitude for points on the x-axis. The solid line was obtained from equation (4.9) while the dashed line was obtained from the fluid-flow code. In all cases, the agreement between the analytical and the numerical results was very good.

The validations performed on ABAQUS show that its analysis of structural vibration frequencies and mode shapes compares relatively well with previous studies. Similarly, verifications of the fluid-flow code confirm that it can produce accurate results.

Table 4.1 Vibration frequencies of clamped half circular arc.

Mode number	Present Study with ABAQUS		Chidamparan and Leissa (1993)
	ω (rad/sec)	$\lambda = \omega a^2 \sqrt{\rho bh / EI}$	$\lambda = \omega a^2 \sqrt{\rho bh / EI}$
1	11.437	4.899	4.6
2	24.464	10.45	10.0
3	44.760	19.17	18.0
4	64.454	27.61	26.8

Table 4.2 Vibration frequencies of pinned circular arc.

Mode number	Present study with ABAQUS		Chidamparan and Leissa (1993)
	ω (rad/sec)	$\lambda = \omega a^2 \sqrt{\rho bh / EI}$	$\lambda = \omega a^2 \sqrt{\rho bh / EI}$
1	6.0083	2.574	2.5
2	18.087	7.748	7.0
3	35.989	15.42	13.5
4	56.992	24.41	22.0

Table 4.3 Natural Frequencies of 2-D dam (rad/sec).

Mode #	Moorthy et al.	Present study with ABAQUS
1	28.5	27.612
2	51.8	58.837
3	83.9	90.676
4	113.1	119.48
5	142.8	148.49
6	171.2	176.12

Table 4.4 Natural frequencies of 3-D structure (rad/sec).

Mode #	Moorthy et al.	Present study with ABAQUS
1	47.3	53.776
2	55.7	63.019
3	65.5	76.598
4	74.2	84.572
5	82.5	93.378
6	88.2	98.095

Table 4.5 Vibration frequencies of 3-D structure (rad/sec).

Mode #	(m,n)	Soedel	Present study with ABAQUS
1	(1,3)	1.1780	1.0743
2	(1,4)	1.4854	1.4016
3	(1,2)	1.9686	1.7402
4	(1,5)	2.2074	2.1843
5	(2,4)	2.4051	2.3281
6	(2,5)	2.5393	2.5144
7	(1,6)	3.1498	3.2463
8	(2,6)	3.2857	3.2937

Table 4.6 Added mass values of a simply supported vibrating circular plate.

ω_{dry} (rad/s)	Generalized mass (kg)	Added mass (kg)	Γ (Present)	Γ (Kwak and Kim)
20.295	11.135	852.56	0.94358	0.98916
124.27	4.2843	124.16	0.36471	0.39168
301.60	5.9982	118.60	0.25270	0.24344
527.01	6.0655	87.389	0.18743	0.17636
925.99	5.5564	57.347	0.13772	0.13822
1336.0	4.0897	34.259	0.11407	0.11366

Table 4.7 Response amplitudes $\hat{\xi}_j$ for a vertical circular cylinder.

Period = 5.0 sec		Period = 6.5 sec		Period = 7.0 sec	
$\hat{\xi}_j$ (Newman)	$\hat{\xi}_j$ (Present)	$\hat{\xi}_j$ (Newman)	$\hat{\xi}_j$ (Present)	$\hat{\xi}_j$ (Newman)	$\hat{\xi}_j$ (Present)
0.04813	0.04761	1.14505	1.14021	0.44875	0.44743
0.00423	0.00418	0.09698	0.09658	0.03795	0.03785
0.00010	0.00010	0.00135	0.00135	0.00046	0.00047
0.00002	0.00001	0.00024	0.00024	0.00008	0.00010

$E = 0.103425 \times 10^{9}$ N/m^2
$\nu = 0.499$
$\rho = 1000$ kg/m^3
$a = 4.0$ m
$h = 0.4$ m ($h/R = 0.1$)
$b = 56.3$ mm
$I = bh^3/12 = 3.0 \times 10^{-4}$ m^4
$\rho bh = 22.52$ kg/m

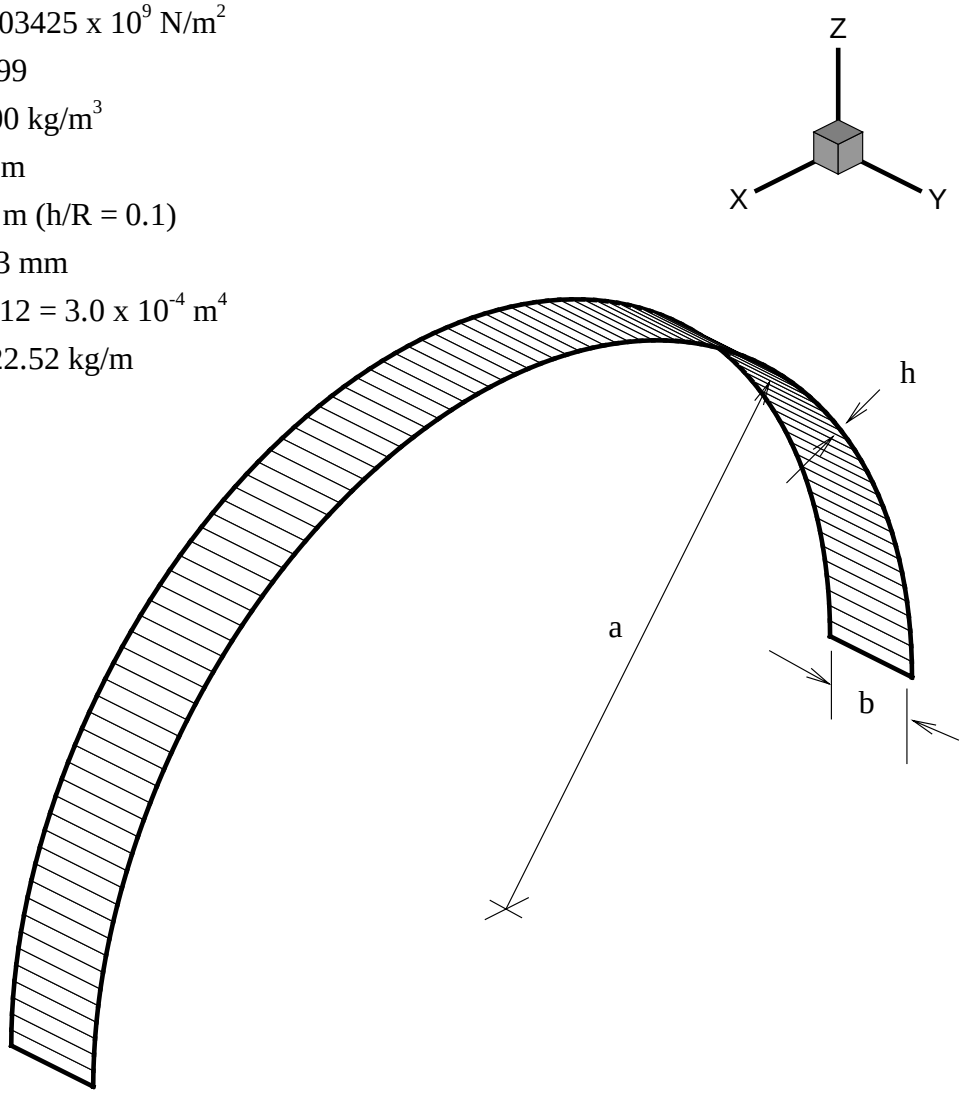

Figure 4.1 ABAQUS model of a circular arc.

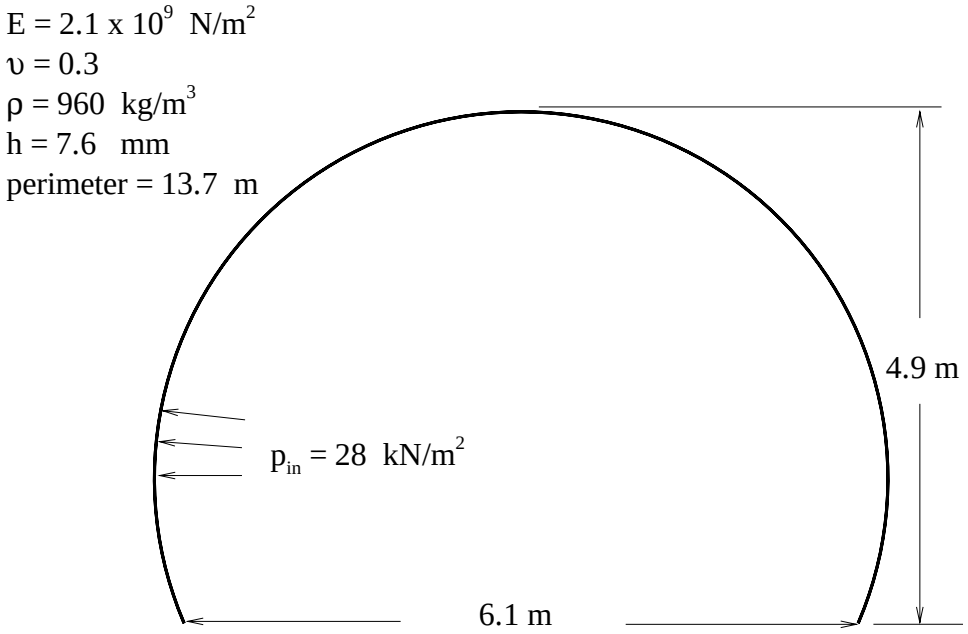

Figure 4.2 2-D dam structure (Moorthy et al., 1995).

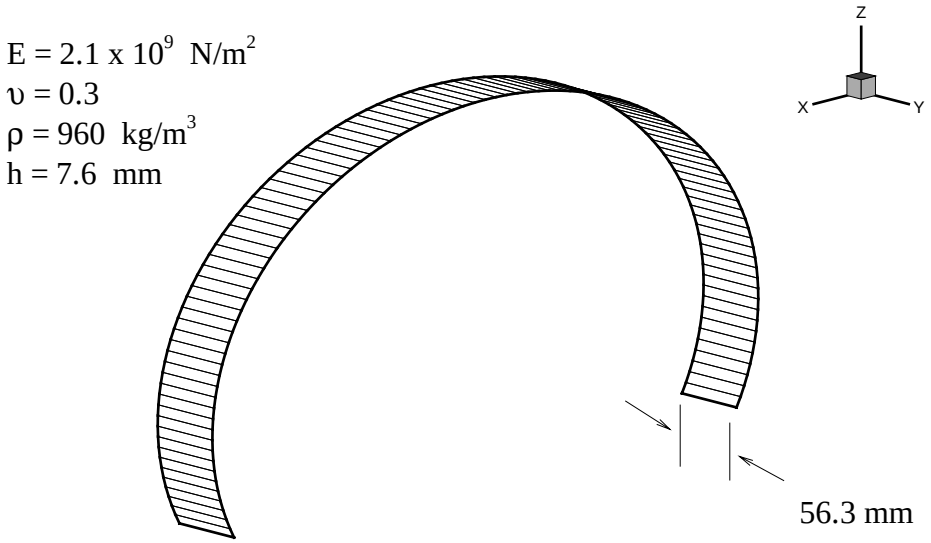

Figure 4.3 ABAQUS model of a 2-D dam structure.

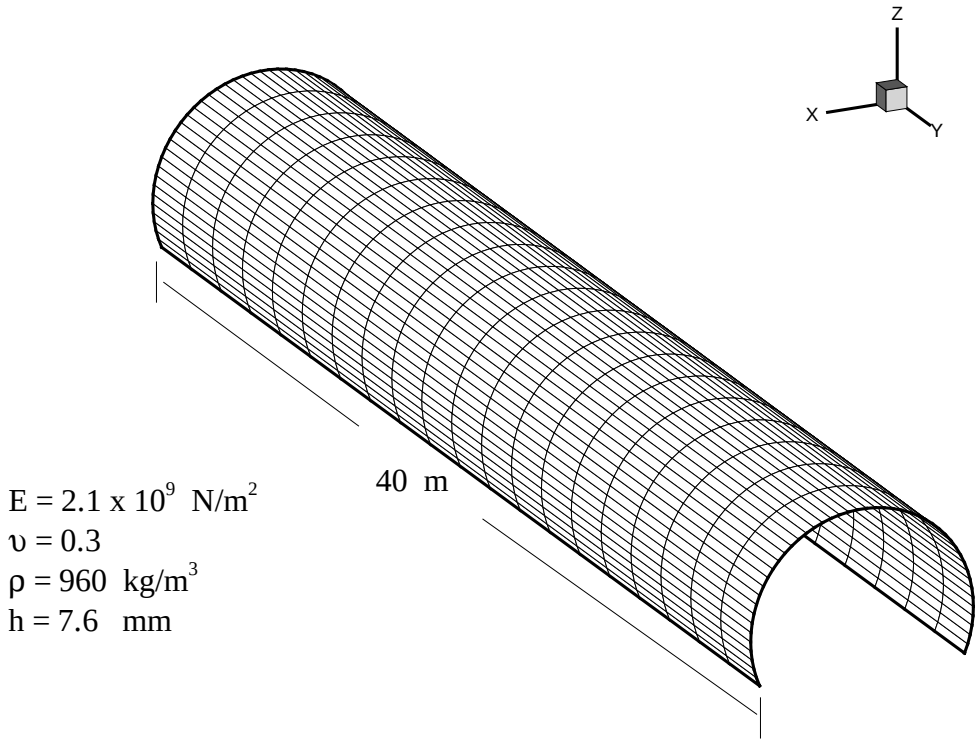

Figure 4.4 ABAQUS model of a 3-D dam structure (Moorthy et al., 1995).

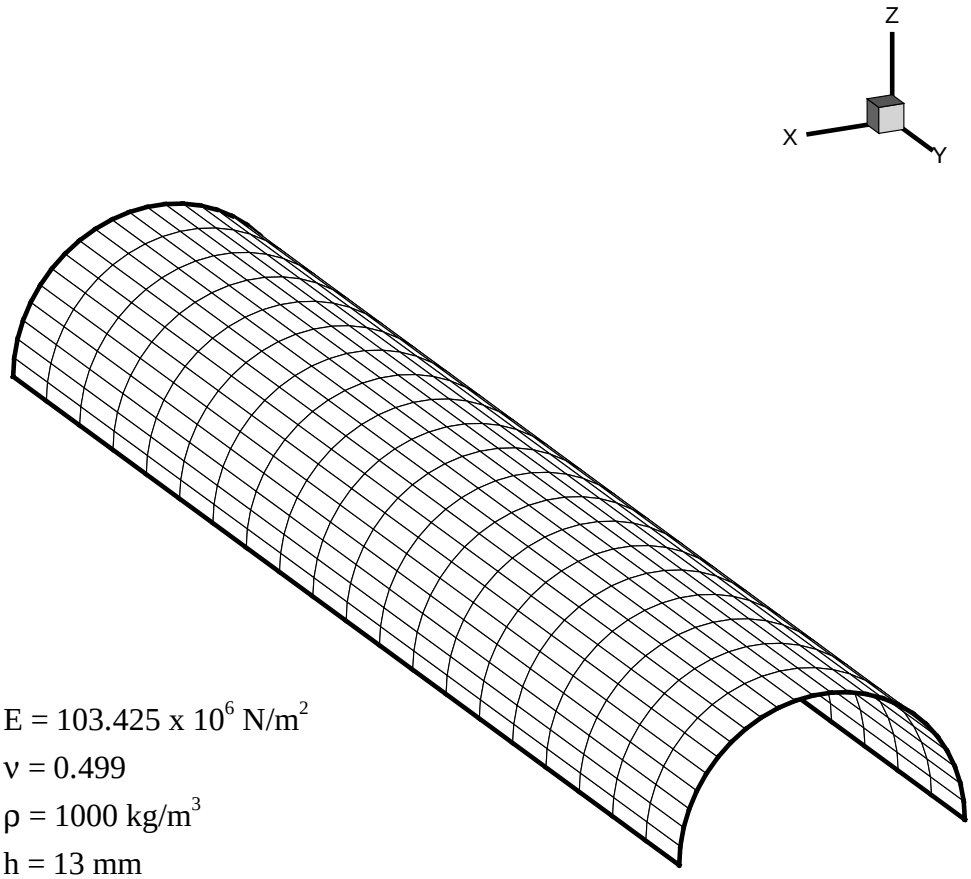

$E = 103.425 \times 10^6$ N/m^2

$\nu = 0.499$

$\rho = 1000$ kg/m^3

h = 13 mm

L = 40 m

$\alpha = 180^0$

a = 4 m

Figure 4.5 ABAQUS model of a 3-D open circular cylindrical shell.

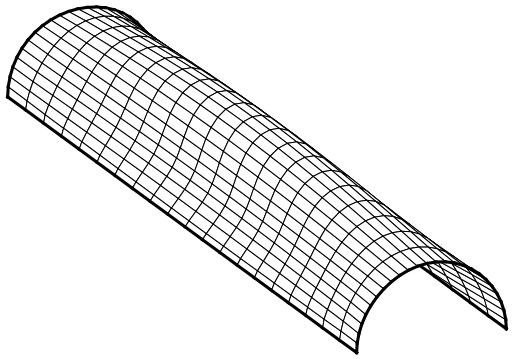

Mode 1
ω = 1.0743 rad/sec

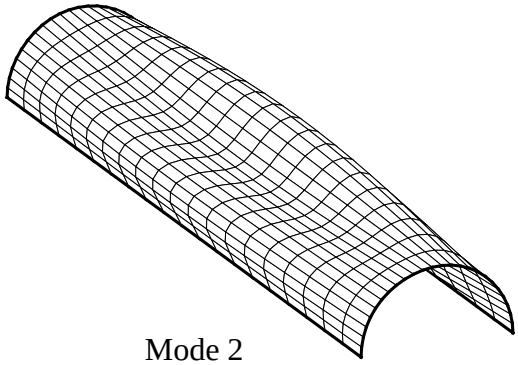

Mode 2
ω = 1.4016 rad/sec

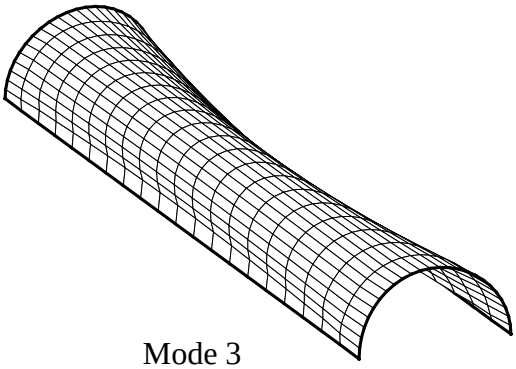

Mode 3
ω = 1.7402 rad/sec

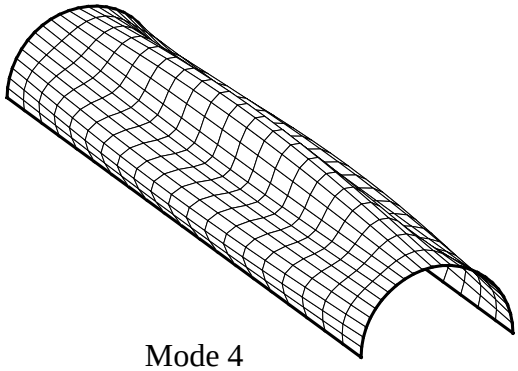

Mode 4
ω = 2.1843 rad/sec

Figure 4.6 Vibration mode shapes 1 - 4 of an open circular cylindrical shell.

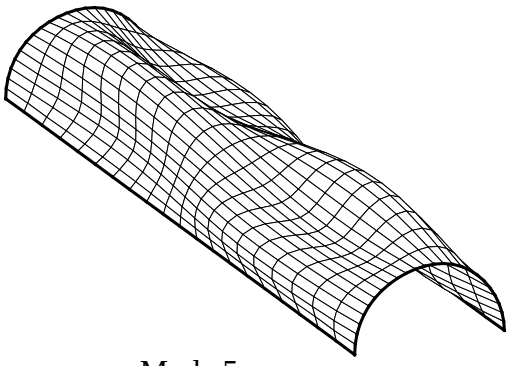

Mode 5
ω = 2.3281 rad/sec

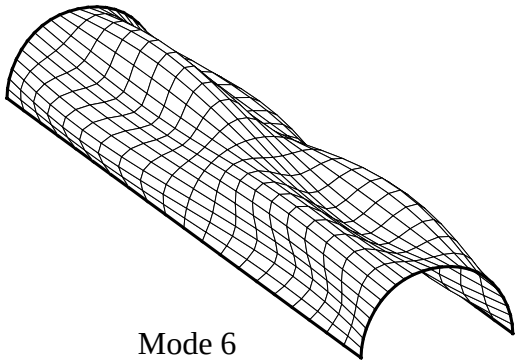

Mode 6
ω = 2.5144 rad/sec

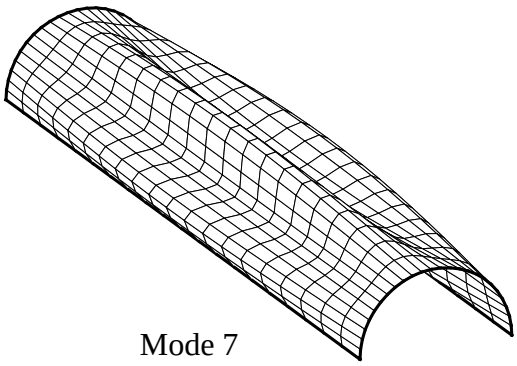

Mode 7
ω = 3.2463 rad/sec

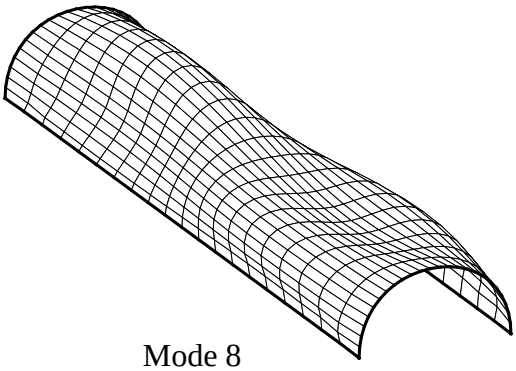

Mode 8
ω = 3.2937 rad/sec

Figure 4.7 Vibration mode shapes 5 - 8 of an open circular cylindrical shell.

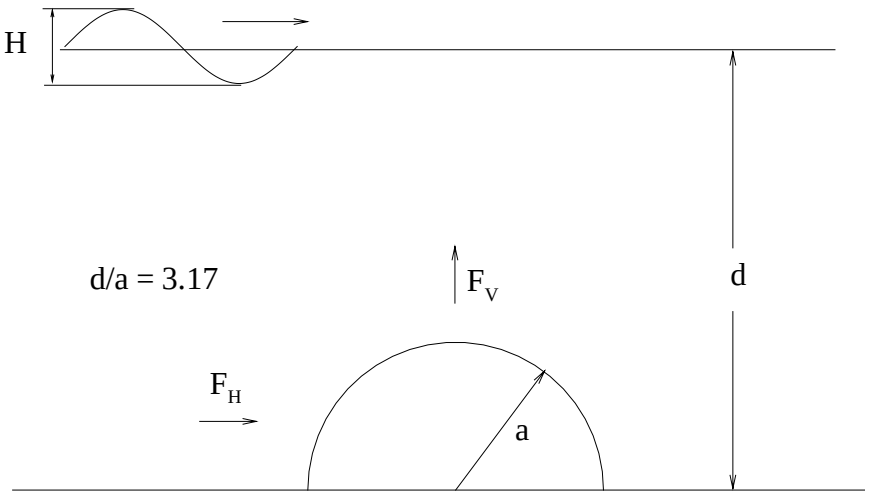

Figure 4.8 Hydrodynamic forces on a hemicylinder (Chakrabarti and Naftzger, 1989).

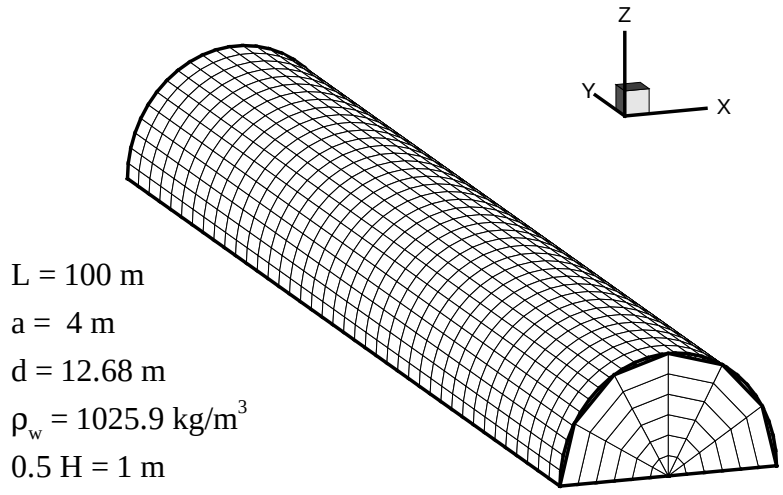

Figure 4.9 Discretized model of a hemicylinder (1072 quadrilateral panels).

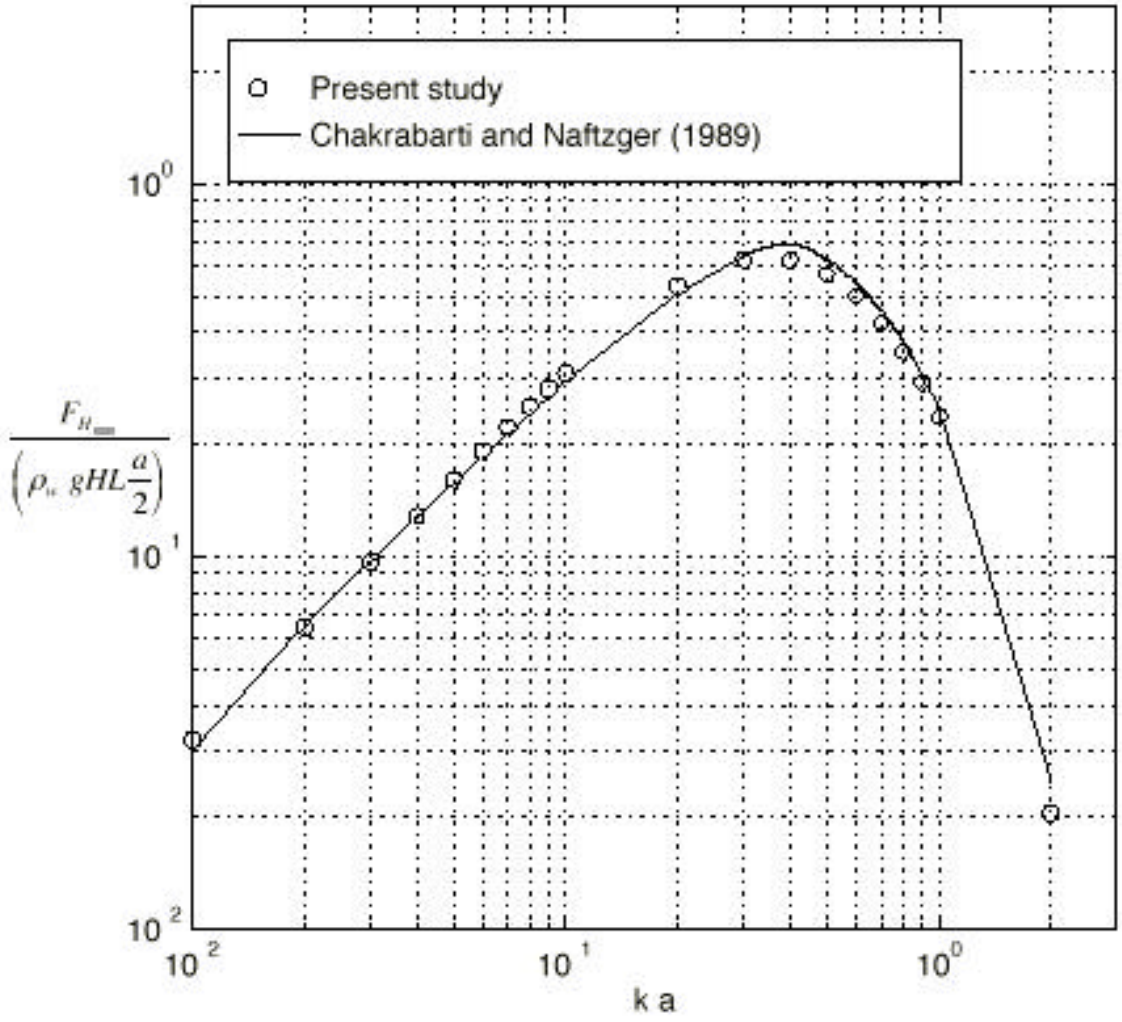

Figure 4.10 Nondimensional horizontal force on a hemicylinder.

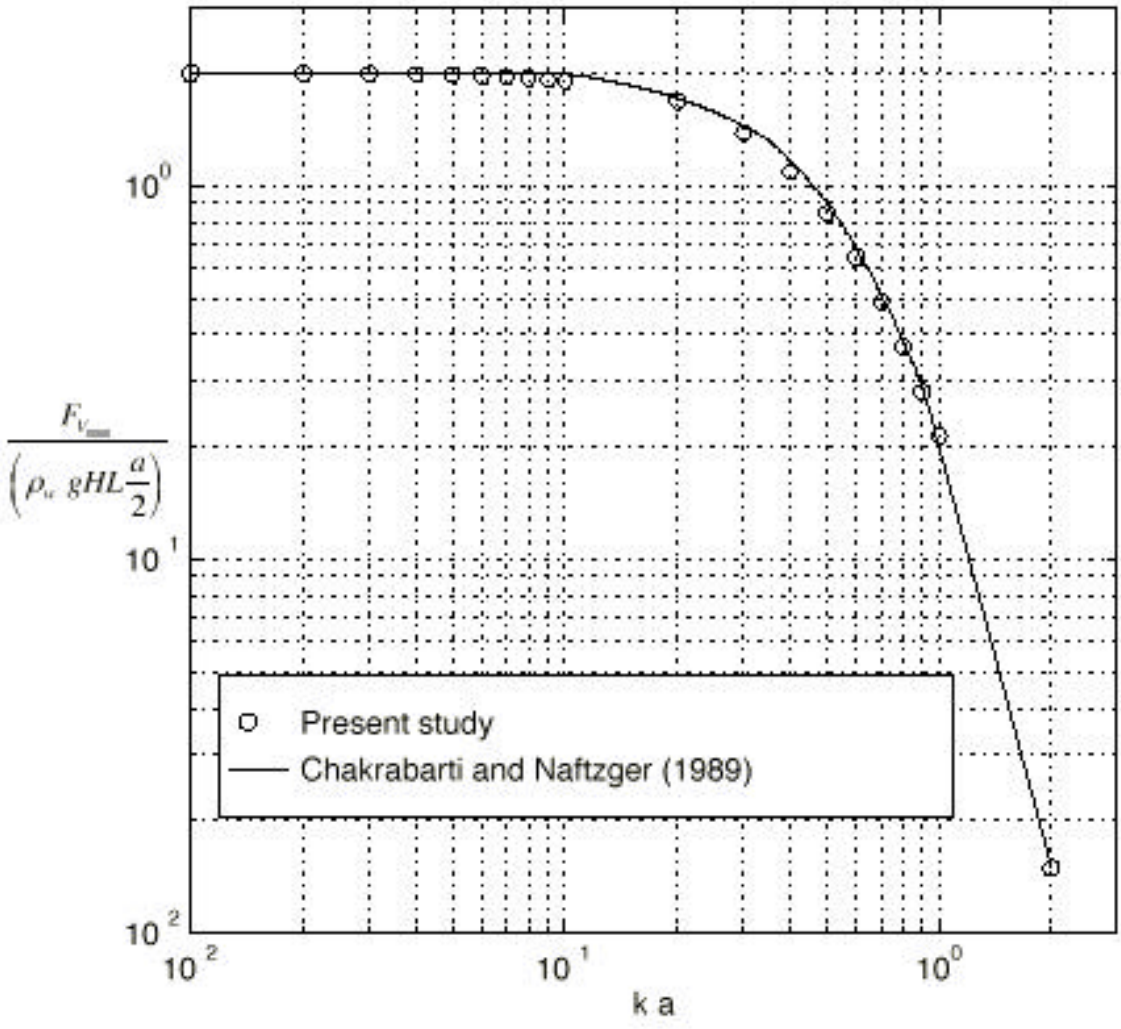

Figure 4.11 Nondimensional vertical force on a hemicylinder.

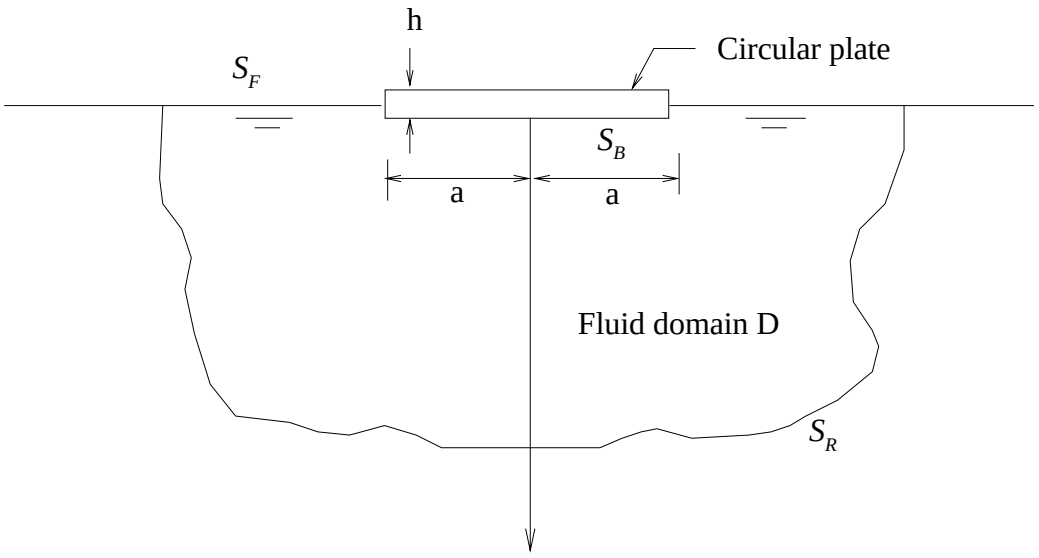

Figure 4.12 Axisymmetric vibration of circular plates (Kwak and Kim, 1991).

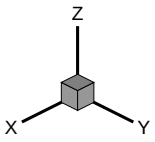

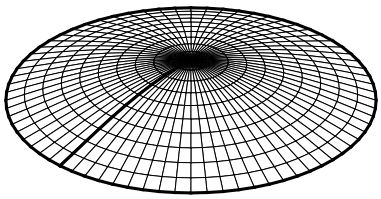

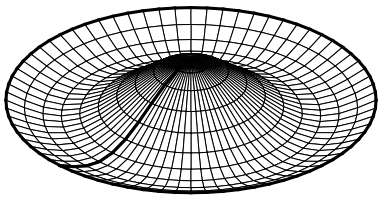

Mode 1
ω = 20.295 rad/sec

Mode 2
ω = 124.27 rad/sec

Figure 4.13 Vibration mode shapes 1-2 of a circular plate.

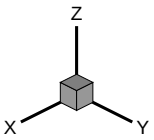

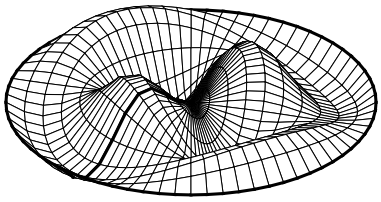

Mode 3
ω = 301.60 rad/sec

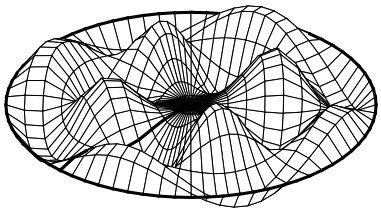

Mode 4
ω = 527.01 rad/sec

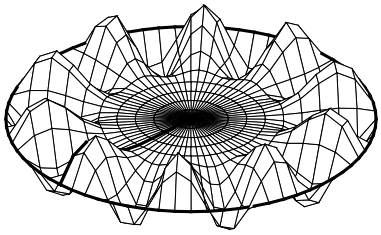

Mode 5
ω = 925.99 rad/sec

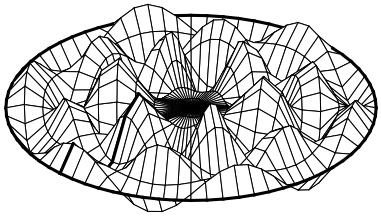

Mode 6
ω = 1336.0 rad/sec

Figure 4.14 Vibration mode shapes 4-6 of a circular plate.

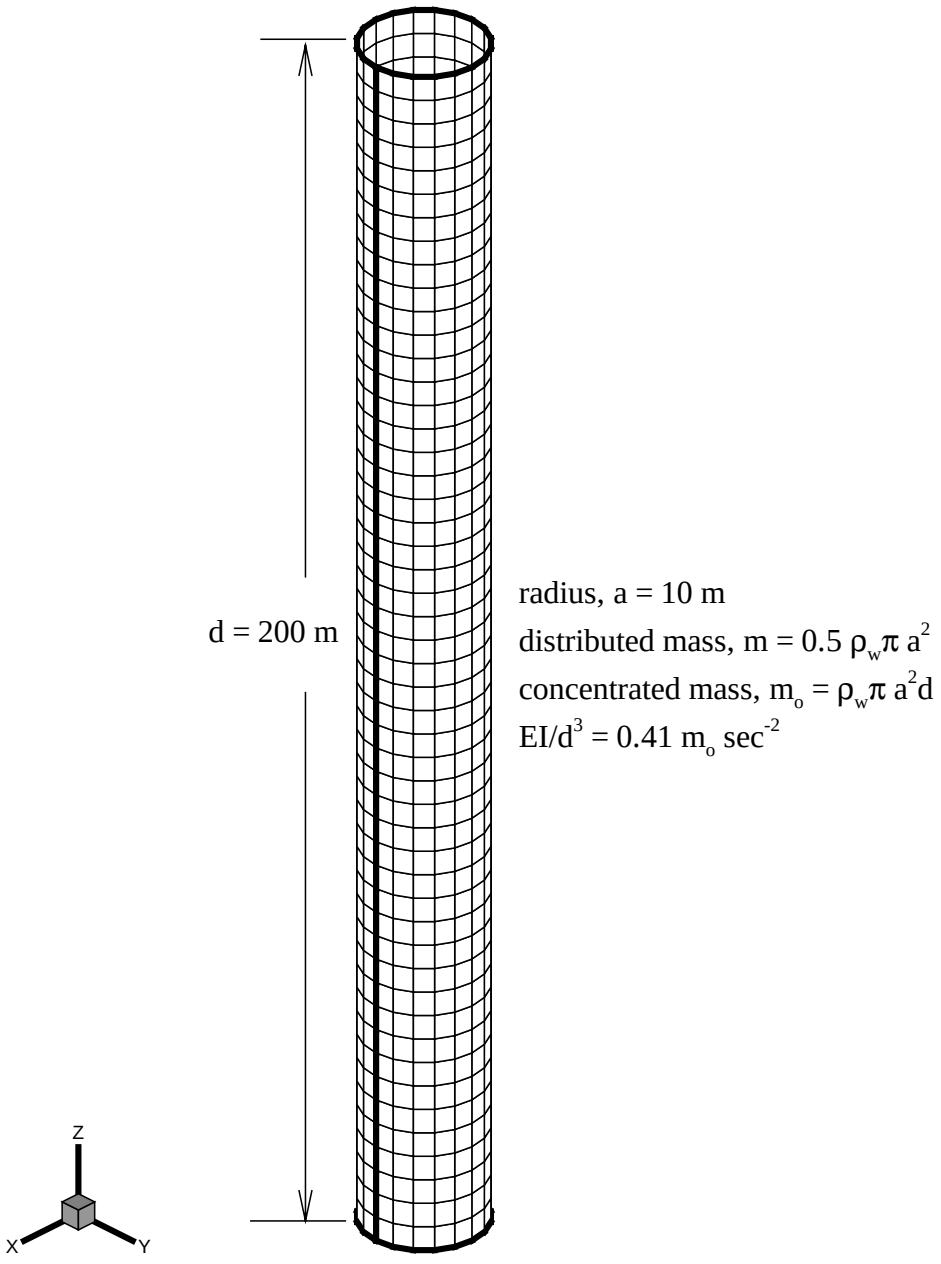

Figure 4.15 Discretized model of a vertical column (1000 quadrilateral panels).

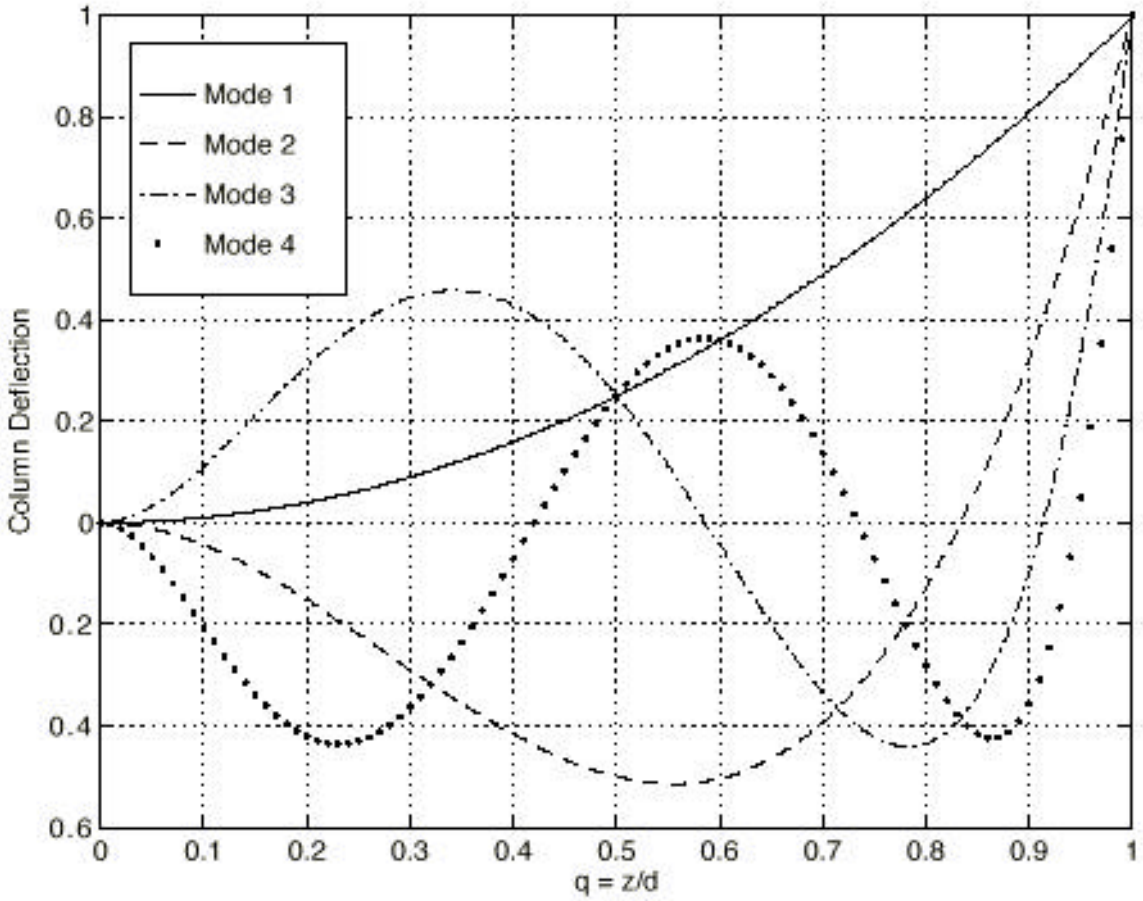

Figure 4.16 Vibration mode shapes 1-4 for a vertical column.

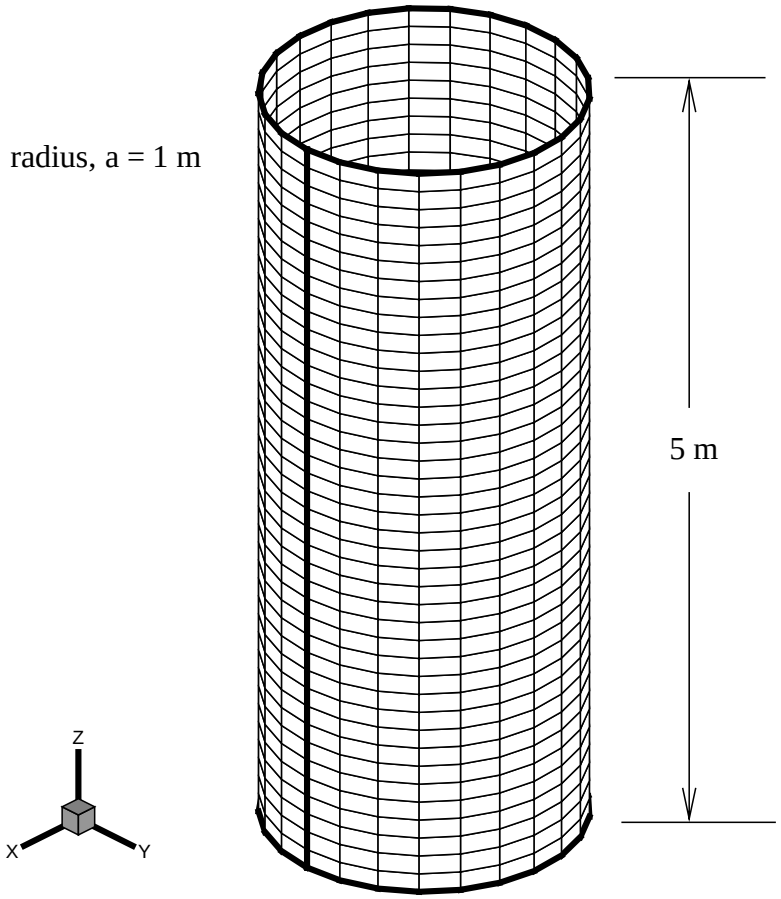

Figure 4.17 Discretized model of a vertical column (1000 quadrilateral panels).

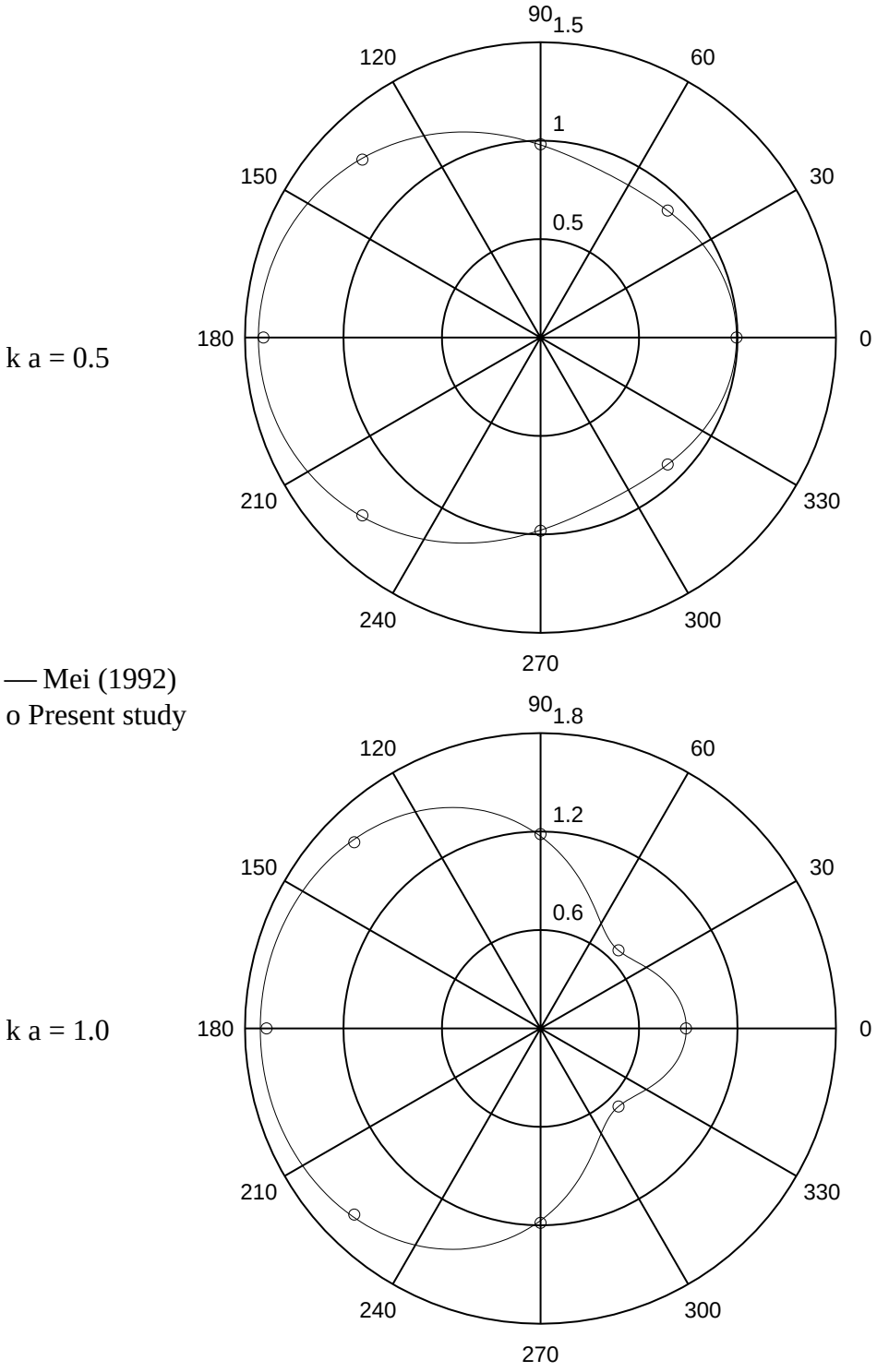

Figure 4.18 Polar distribution of free-surface amplitude.

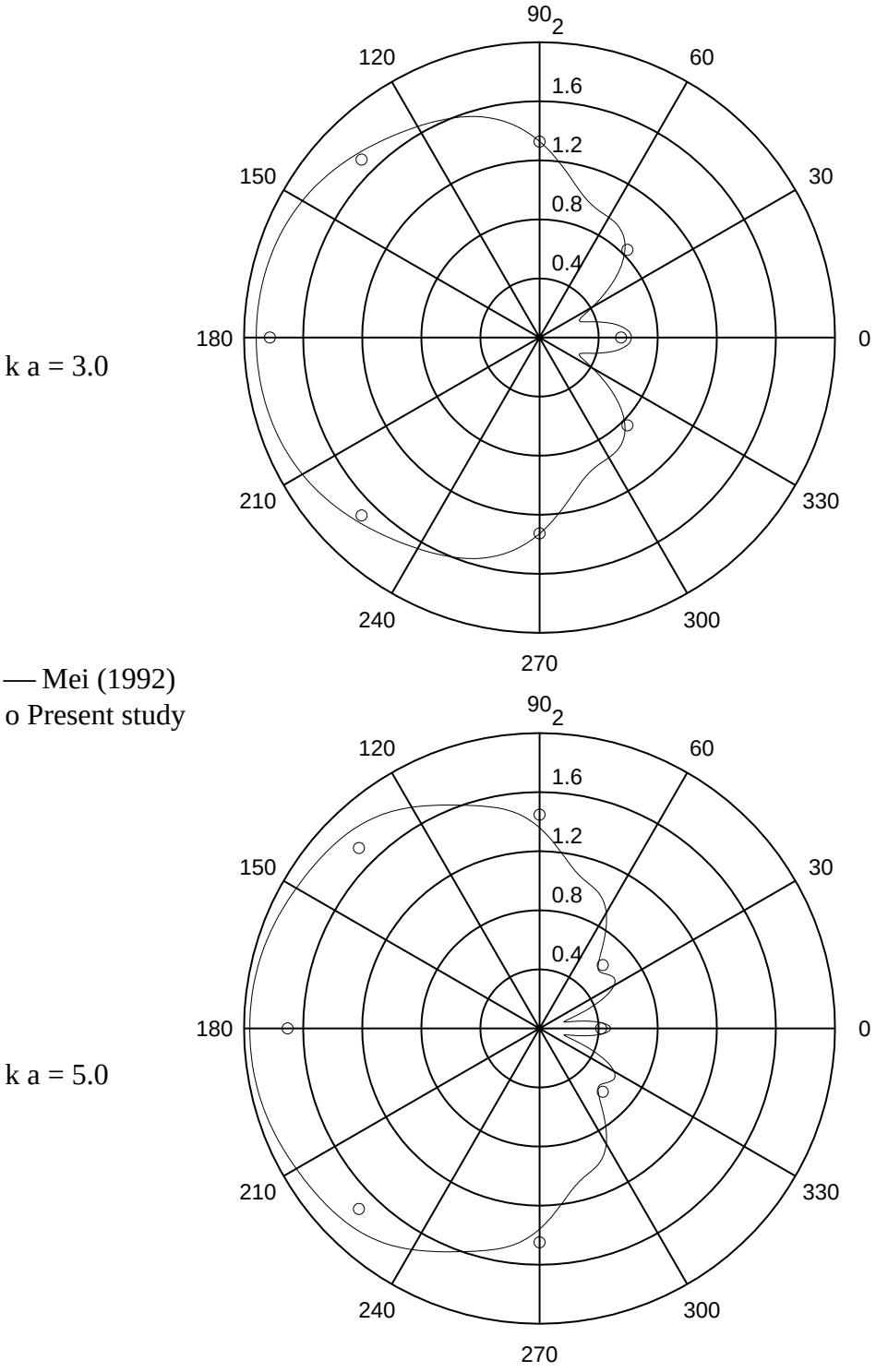

Figure 4.19 Polar distribution of free-surface amplitude.

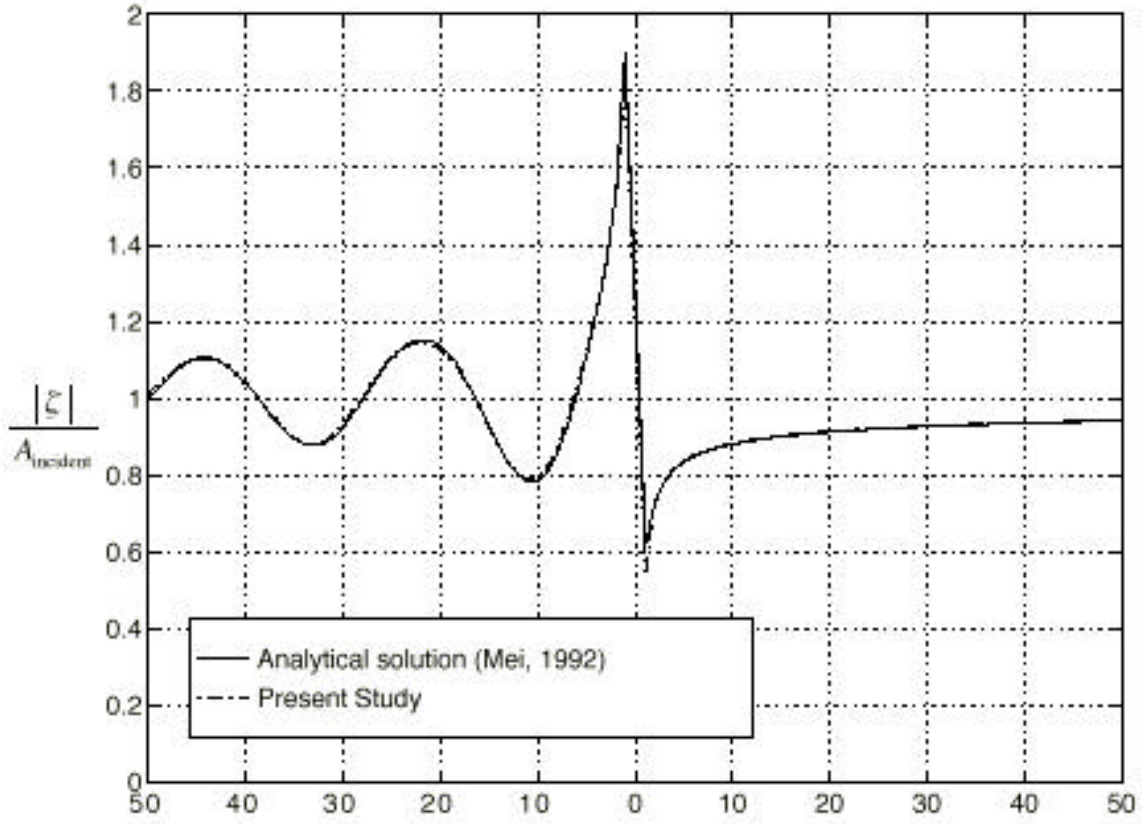

Figure 4.20 Free-surface amplitude away from the cylinder (k a = 3.0).

CHAPTER 5 NUMERICAL RESULTS

Numerical analysis of interaction of the structure with waves was performed at two cases of water depth, 6 m and 5 m. In each case, the analysis includes free vibration without water, free vibration with water and forced vibration. As discussed in Chapter 3, the breakwater is modeled as a thin, isotropic, elastic shell. Using 1500 quadrilateral panels of element S4R, a breakwater of 150 m length and 4 m radius is constructed as shown in Fig. 5.1. There are 20 panels along the circumference and 75 panels along the length.

The structure's boundary conditions are defined as follows:

- all nodes along the sides parallel to the y-axis are pinned,
- all nodes at the structure's ends (y = 0 and y = L) are clamped.

5.1 WATER DEPTH OF 6 m

5.1.1 FREE VIBRATION ANALYSIS WITHOUT WATER

For a water depth of 6 m, 5% of the maximum external hydrostatic pressure is determined to be 3000 N/m^2. Applying this pressure as a uniform internal pressure to the structure, small vibrations of the structure about the static equilibrium are analyzed using ABAQUS. The first fifteen "dry" mode shapes are shown in Fig. 5.2. Modes 1,2,5,7,8,11,13,14, and 15 are symmetric while modes 3,4,6,9,10, and 12 are antisymmetric. The natural frequencies of the structure are obtained from:

$$\left| -\omega^2 M_g + K_g \right| = 0 \tag{5.1}$$

As discussed previously in Chapter 3, these "dry" mode shapes are used as basis functions that describe the displacement of the body surface when external water is present.

A study was conducted to determine the changes in the natural frequencies if the structure is modeled as a membrane (e.g. no bending stiffness). Using the quadrilateral membrane element M3D4R in ABAQUS, the natural frequencies of the structure were found to be much smaller as shown in Table 5.1.

5.1.2 FREE VIBRATION ANALYSIS WITH WATER

In order to obtain the "wet" natural frequencies of the structure, the effect of external and internal water is included in the analysis. The "wet" vibration frequencies can be determined from:

$$\left| -\omega^2 \left(M_g + A + A_{\text{internal}} \right) + K_g \right| = 0 \tag{5.2}$$

where the generalized mass matrix, M_g, and the generalized stiffness matrix, K_g, are obtained from ABAQUS.

The external added mass matrix A is a function of wave frequency ω; therefore an iteration process is performed to get the natural vibration frequencies of the structure. For example, to obtain the first "wet" natural frequency, an external added mass matrix, A, is obtained at $\omega = 8.9639$ rad/sec (the first "dry" natural frequency). Solving equation (5.2) yields the new value $\omega = 1.378998$ rad/sec which is used to obtain a new external added mass matrix. The process is repeated until $\left| \dfrac{\omega_i - \omega_{i-1}}{\omega_i} \right|$ is less than or equal to 5%. Notice that only external added mass changes with frequency. The internal added mass, A_{internal}, is independent of wave frequency since the water is contained inside of the structure.

Figure 5.3.a and Fig. 5.3.b show the first four "dry" mode shapes and frequencies along with the corresponding cross-sectional profiles at mid-structure and at

one-quarter length from each end. Modes 1 and 2 are symmetric while modes 3 and 4 are antisymmetric.

Figure 5.4.a and Fig. 5.4.b show the first four "wet" mode shapes and frequencies. These figures show that the "wet" mode shapes do not change significantly as compared to the "dry" mode shapes. Symmetric mode shapes are observed in modes 1 and 2 while antisymmetric mode shapes are observed in modes 3 and 4.

Table 5.1 contains the values of the generalized mass of the structure, the diagonal elements of the external added mass matrix and the internal added mass matrix, and the "dry" and "wet" frequencies. As can be seen, the influence of the external and internal water is significant. The magnitudes of the external and internal added mass are much larger than the mass of the structure. As a result, there is an average reduction of 82.7% on the magnitude of the first four natural frequencies of the structure.

5.1.3 FORCED VIBRATION OF THE STRUCTURE IN WAVES

5.1.3.1 NORMAL INCIDENT WAVES ($\beta = 0$)

Hydrodynamic coefficients, forces, and response of the structure

We now consider the case of waves interacting with a flexible breakwater. As discussed in Chapter 3, the effect of the external water is represented by the added mass matrix, A, the damping matrix, B, and the hydrodynamic forces, $F_i^I + F_i^D$.

Figure 5.5 shows the non-dimensional added mass values for mode 1, A_{11}, and for mode 2, A_{22}, as a function of the non-dimensional term ka (k is the wave number and a is the radius of the structure). This plot indicates that the added mass coefficient for

mode 2 is much lower than that for mode 1. For mode 1, the added mass coefficient reaches its maximum value at a lower value of ka than for mode 2.

The values of the non-dimensional wave damping for mode 1, B_{11}, and for mode 2, B_{22}, are presented in Fig. 5.6. It can be observed that at low and high values of ka, the values of these wave damping coefficients are negligible. Similar to the added mass plot, the wave damping coefficient for mode 2 is much lower than that for mode 1.

Figure 5.7 shows the variation of the total nondimensional vertical and horizontal hydrodynamic forces on the structure. These forces are the maximum wave-induced forces as defined by Chakrabarti and Naftzger (1989) (see Fig. 4.8 and Section 4.2.1). The vertical force decreases as ka increases, while the horizontal force increases initially with ka but decreases after it reaches its maximum at $ka \approx 0.5$. Figure 5.8 shows that for the case of normal incident waves the hydrodynamic force for mode 1 is much higher than that for mode 2. For low and high values of ka, the magnitudes of the wave forces are small for both modes.

The Response Amplitude Operator $(RAO)_j$ values are obtained by solving for $\hat{\xi}_j$ using equation (3.4). Figure 5.9 presents the $(RAO)_1$ and $(RAO)_2$ as functions of ka for the case of normal incident waves. It can be seen that $(RAO)_1$ is maximum close to the first "wet" natural frequency $\omega_{n_1} = 1.46045$ rad/sec ($ka = 0.97$) and, likewise, $(RAO)_2$ is maximum close to the second "wet" natural frequency $\omega_{n_2} = 2.4650$ rad/sec ($ka = 2.48$).

Free surface elevation

The amplitude of the free surface elevation (ζ, see equation (3.17)) is obtained for several wave frequencies. The incident wave is taken to have a unit amplitude ($A_{\text{incident}} = 1$).

Figure 5.10 and Fig. 5.11 show the wave amplitudes at the middle and at the end of the structure for incident wave frequencies $\omega = \frac{\pi}{4}$ ($ka = 0.437$) and $\frac{\pi}{2}$ ($ka = 1.1$), respectively. From these figures, it can be seen that the flexible structure is much more effective as a breakwater than the fixed rigid structure in reducing the amplitude of the incident waves.

In Fig. 5.12 to Fig. 5.17, different colors are used to represent the different values of ζ at different points in the xy-plane. The colorbar shows the corresponding numerical value for each color. Notice that the color scale is different for each figure. The breakwater extends from y = 0 to y = 150 m and from x = -4 m to x = 4 m.

For an incident wave of frequency $\omega = \frac{\pi}{4}$ rad/sec, the non-dimensional amplitude of the free surface elevation are presented in Fig. 5.12. From the colorbar, it can be seen that the wave amplitude behind the structure is reduced to 0.5 which means the amplitude is reduced by 50%.

Figure 5.13 shows the wave amplitude of the free surface elevation for wave frequency $\omega = \frac{\pi}{6}$ rad/sec ($k\,a = 0.28$). For this frequency, the wave intensity behind the structure is reduced only by 20%. Figure 5.14 and Fig. 5.15 depict the wave amplitudes of the free surface elevation for wave frequencies $\omega = \omega_{n_1} = 1.46045$ rad/sec ($k\,a = 0.97$) and $\omega = \omega_{n_2} = 2.4650$ rad/sec ($k\,a = 2.48$), respectively. From the colorbar, it can be

seen that the wave amplitude behind the structure is reduced by as much as 80% for wave frequency $\omega = \omega_{n_1}$ and as much as 90% for wave frequency $\omega = \omega_{n_2}$. Figure 5.17 shows the wave amplitude of the free surface elevation for wave frequency $\omega = \pi$ rad/sec ($k\,a = 4.0$). For this wave frequency, it can be seen that the structure is no longer effective. It is also observed that diffraction of the wave energy around the ends of the structure has significant effect on the amplitude of the wave as depicted by the pattern behind and in front of the structure (see Fig. 5.17). Figure 5.13 to Fig. 5.17 show that the flexible breakwater is effective in reducing the maximum wave amplitude over a wide range of frequencies. We can also see that the wave field behind the structure is very three-dimensional. It is observed that the structure is effective close to the middle but not at the ends. This phenomenon can be explained as follows; the ends of the structure do not move much (recall the ends are clamped); therefore the waves generated by the structure to reduce the amplitude of the incoming waves are small. At low and high frequencies, the breakwater is not effective. As shown in Table 5.2, the RAO's for low or high frequency waves are small compared to those for other frequencies; therefore the structure does not move enough to generate waves that will cancel the incoming waves.

Figure 5.18 depicts the displacements of the structure over time for incident waves of frequency $\omega = \frac{\pi}{4}$ rad/sec. The corresponding mid-section displacements over time are presented in Fig. 5.19. As defined in equation (3.3), each "dry" mode shape has influence on the displacement of the structure. It is evident from Fig. 5.19 that mode shape 1 is dominant because $\hat{\xi}_1$ outweighs other $\hat{\xi}$'s (see Table 5.2). The structure moves mostly in mode 1 so that it generates waves that cancel the incident waves. Modes 3 and 4 are not excited because the disturbance is symmetric about the middle of the structure. The free surface elevations at different times are presented in Fig. 5.20.a to Fig. 5.20.d.

In a similar fashion, the displacements of the structure and the free surface elevations over time for the case of incident wave frequency $\omega = \omega_{n_2}$ rad/sec are presented in Fig. 5.21 to Fig. 5.23. Notice that the structure moves mostly in mode 2 since $\hat{\xi}_2$ is dominant over other $\hat{\xi}$'s.

5.1.3.2 OBLIQUE INCIDENT WAVES ($\beta = 15°, 30°$)

Hydrodynamic coefficients, forces, and response of the structure

For the case of oblique incident waves, the hydrodynamic coefficients are the same as those for the case of normal incident waves. The hydrodynamic forces, however, change significantly as can be seen in Fig. 5.24 and Fig. 5.25 for the case of incident waves at an angle of 15 degrees and in Fig. 5.27 and Fig. 5.28 for the case of incident waves at an angle of 30 degrees.

It can be observed that the frequency at the peak of the horizontal force as well as its maximum magnitude decreases as the incoming angle increases. The curve of the vertical force drops faster as the incoming angle increases, but its maximum magnitude stays the same (see Fig. 5.7, Fig. 5.24, and Fig. 5.27). Referring to Fig. 5.8, the hydrodynamic forces for modes 1 and 2 are reduced considerably as the incoming angle increases.

Oblique incident waves excite the antisymmetric modes such as modes 3 and 4. This is evident as shown in Fig. 5.26 and Fig. 5.29. However, the RAO's reduce as the incoming angle increases, which means the structure is not as effective as in the case of normal incident waves. The frequencies at the peak of the RAO's reduce as the incoming angle increases.

Free surface elevation

The wave amplitudes are obtained for several wave frequencies. Figure 5.30 to Fig. 5.35 present the color image of the wave amplitudes. It is evident from these figures that the breakwater becomes less effective as the incoming angle increases.

Figure 5.36 presents the structure's displacements over time for an incident wave at $\beta = 15°$ for wave frequency $\omega = \frac{\pi}{4}$ rad/sec. The corresponding free surface elevations are presented in Fig. 5.37.a to Fig. 5.37.d. Similarly, Fig. 5.38 to Fig. 5.39 present results for an incident wave at $\beta = 30°$ for wave frequency $\omega = \frac{\pi}{4}$ rad/sec.

5.1.4 TRANSMISSION COEFFICIENT

In this analysis, the transmission coefficient is defined to be the mean value of the wave amplitudes behind the middle of the structure at distances from the end of the structure (x = 4 m) to 50 m from the center of the structure. Figure 5.40 shows the variation of wave transmission coefficient as a function of $k\,a$ for three different incident wave angles. As shown in Fig. 5.40, the breakwater is effective over a wide range of frequencies for the case of normal incident waves. For $\beta = 15°$, the structure is effective only for a small frequency bandwidth. As the angle of the incident wave increases to 30 degrees, the breakwater becomes ineffective.

5.2 WATER DEPTH OF 5 m

5.2.1 FREE VIBRATION ANALYSIS WITHOUT WATER

The same procedure used for the case of water depth 6 m is followed to obtain the natural "dry" frequencies of the structure. Since the water depth is 5 m, 5% of the maximum external hydrostatic pressure is determined to be 2500 N/m^2. As shown in Fig. 5.41, the first fifteen "dry" mode shapes are essentially the same as those for the case of water depth 6 m. The frequencies, however, are slightly lower because the internal pressure is slightly lower.

5.2.2 FREE VIBRATION ANALYSIS WITH WATER

For the case of water depth 5 m, the values of the external and internal added mass are calculated to find the "wet" natural frequencies of the structure. The iteration process is also used. Figure 5.42 and Fig. 5.43 show, respectively, the first four "dry" and "wet" mode shapes.

Compared to the case of water depth 6 m, the "wet" frequencies are slightly higher. At a water depth of 5 m, the structure moves a smaller amount of external water than if it were submerged in water of 6 m depth. As a result, the "wet" natural frequencies of the structure are slightly higher, as observed. Notice that the "wet" mode shapes for modes 3 and 4 are similar to each other.

5.2.3 FORCED VIBRATION OF THE STRUCTURE IN WAVES

5.2.3.1 NORMAL INCIDENT WAVES ($\beta = 0$)

Hydrodynamic coefficients, forces, and response of the structure

For the case of normal incident waves, the hydrodynamic coefficients are plotted as functions of $k\,a$ in Fig. 5.44 and Fig. 5.45.

As shown in Fig. 5.44, for low and high values of $k\,a$, the non-dimensional added mass coefficient for mode 1 is greater than that for mode 2. For $k\,a = 0.75$ to $k\,a = 2.25$, the added mass coefficient for mode 1 is lower than that for mode 2. Referring to Fig. 5.5, it can be seen that for a water depth of 5 m, the maximum values of the added mass coefficients for modes 1 and 2 are greater than those for a water depth of 6 m. Notice that the vertical scales in Fig. 5.5 and Fig. 5.44 are different.

Figure 5.45 shows that the non-dimensional damping coefficient for mode 1 is greater than that for mode 2 if $k\,a < 2.3$. For low and high values of $k\,a$, the damping coefficients are negligible for both modes. Compared to the case of a water depth of 6 m (see Fig. 5.6), the damping coefficients for the case of a water depth of 5 m are much larger. Notice that the vertical scales in Fig. 5.6 and Fig. 5.45 are also different.

Figure 5.46 indicates that the hydrodynamic forces do not change significantly as the water depth changes. Referring to Fig. 5.7, it can be seen that the curve of the vertical force drops more slowly for the case of water depth 5 m while the maximum of the horizontal force increases slightly as the water depth decreases.

Figure 5.48 presents the values of $(\mathrm{RAO})_1$ and $(\mathrm{RAO})_2$ as functions of $k\,a$. It can be seen that the curve of $(\mathrm{RAO})_2$ has two peaks. This can be explained as follows: The added mass, damping and hydrodynamic coefficients are strongly dependent on the frequency of the wave (see Fig. 5.44, Fig. 5.45 and Fig. 5.47). The first peak of $(\mathrm{RAO})_2$ corresponds to the maximum hydrodynamic force for mode 2 as shown in Fig. 5.47 and the second peak of $(\mathrm{RAO})_2$ corresponds to the second "wet" natural frequency $\omega_{n_2} = 2.7753$ rad/sec ($ka = 3.14$). The same explanation applies for the curve of $(\mathrm{RAO})_1$.

It can be seen that the maximum of $(RAO)_1$ is not close to the first "wet" natural frequency $\omega_{n_1} = 1.5936$ rad/sec ($ka = 1.16$). As shown in Fig. 5.47, the maximum force for mode 1 occurs at $k\,a = 0.5$ and the peak of $(RAO)_1$ also occurs at this wave number.

Free surface elevation

Figure 5.49 and Fig. 5.50 show the wave amplitudes at the middle and at the ends of the structure for wave frequencies $\omega = \frac{\pi}{4}$ rad/sec ($k\,a = 0.47$) and $\omega_{n_2} = 2.7753$ rad/sec ($k\,a = 3.14$), respectively. It can be seen that the structure reduces the wave intensity efficiently and that the flexible structure is more effective than the rigid one.

The wave amplitudes at different frequencies are presented in Fig. 5.51 to Fig. 5.56. It is observed that for wave frequencies $\omega = \frac{\pi}{2}$ rad/sec ($k\,a = 1.13$) and $\omega_{n_1} = 1.5936$ rad/sec ($k\,a = 1.16$), the wave amplitudes behind the structure are not reduced much. As shown in Fig. 5.57, it is apparent that for wave frequency $\omega = \omega_{n_1}$, the structure does not move and therefore does not generate waves that cancel the incoming waves.

Figure 5.58 depicts the displacements of the structure over time for incident waves of frequency $\omega = \frac{\pi}{4}$ rad/sec. It is evident that, for this wave frequency, the structure moves mostly in mode 1 and generates waves that cancel the incident waves. Modes 3 and 4 are not excited because the disturbance is symmetric about the middle of the structure. The free surface elevations at different times are presented in Fig. 5.59.a to Fig. 5.59.d.

5.2.3.2 OBLIQUE INCIDENT WAVES ($\beta = 15°$)

Hydrodynamic coefficients, forces, and response of the structure

For the case of oblique incoming waves, the hydrodynamic forces show the same changes observed in the case of water depth 6 m. As shown in Fig. 5.60, the curve of the vertical force drops faster for the incoming angle of 15 degrees. The magnitude of the horizontal force is lower for the incoming angle of 15 degrees than that for the normal incident waves. The forces for modes 1 and 2 are reduced considerably (see Fig. 5.61 and Fig. 5.47) when the depth changes from 6 m to 5 m.

As shown in Fig. 5.62, oblique incident waves excite the antisymmetric modes such as modes 3 and 4. However, the RAO's reduce as compared to the case of normal incoming waves (see Fig. 5.48), which means the structure is not as effective. The frequencies at the peak of the RAO's reduce as the incoming angle increases. This is also observed for the case of a water depth 6 m.

Free surface elevation

Figure 5.63 and Fig. 5.64 present the color image of the wave amplitudes at wave frequencies $\omega = \frac{\pi}{2}$ and $\frac{\pi}{6}$, respectively. It is evident that the structure is less effective for the oblique incoming waves.

Figure 5.65 shows the displacements of the structure over time and Fig. 5.66 depicts the surface elevation at different times.

5.2.4 TRANSMISSION COEFFICIENT

Figure 5.67 shows the transmission coefficients (defined previously in Section 5.1.4) as a function of $k\,a$. For the case of normal incident waves in a water depth of 5 m, the structure is effective for $0.25 < k\,a < 1.0$ and $1.75 < k\,a < 3.4$. For the case of oblique incident waves, the structure is effective only for a small frequency bandwidth.

Table 5.1 Natural frequencies for shell and membrane structure.

Mode #	ω (rad/sec)		Difference %
	Shell	Membrane	
1	8.9639	7.8598	12.3
2	13.892	7.8853	43.2
3	14.227	8.4177	40.8
4	14.769	9.7190	34.2
5	15.126	10.327	31.7
6	16.776	10.870	35.2
7	19.170	11.366	40.7
8	19.876	11.366	42.8
9	22.164	11.374	48.7
10	22.805	11.378	50.1
11	24.326	11.413	53.1
12	25.540	11.451	55.2
13	25.549	11.490	55.0
14	26.394	11.571	56.2
15	26.846	11.629	56.7

Table 5.2 External and internal added mass.

Mode #	Generalized mass (kg)	External added mass (A_{jj}) (kg)	Internal added mass (kg)		Dry ω_n (rad/sec)	Wet ω_n (rad/sec)
			A_{jj}	$\frac{A_{jj}}{0.5\rho_w \pi a^2 L}$		
1	49,004.0	610,584.0	1,172,604.0	0.303	8.9639	1.4605
2	20,721.0	238,176.0	398,916.59	0.103	13.892	2.4650
3	23,034.0	265,334.0	434,454.41	0.112	14.227	2.5400
4	46,610.0	471,392.0	1,048,136.0	0.271	14.769	2.5508

Table 5.3 RAO for $\omega = \frac{\pi}{6}, \frac{\pi}{4}, \omega_{n_1}, \omega_{n_2}, \frac{\pi}{2}$, and π rad/sec ($\beta = 0$).

$\omega = \frac{\pi}{6}$	$\omega = \frac{\pi}{4}$	$\omega = \omega_{n_1}$	$\omega = \omega_{n_2}$	$\omega = \frac{\pi}{2}$	$\omega = \pi$
0.9882	1.567	1.906	0.169	1.677	0.014
0.0760	0.185	0.807	1.6649	0.903	0.118
1.542×10^{-6}	9.415×10^{-6}	2.248×10^{-3}	4.494×10^{-3}	3.144×10^{-4}	4.011×10^{-4}
0.0014	5.357×10^{-3}	0.028	0.036	0.030	1.292×10^{-3}
0.0268	0.064	0.258	0.449	0.287	0.066
2.323×10^{-5}	1.351×10^{-4}	2.697×10^{-3}	0.030	3.666×10^{-3}	8.643×10^{-3}
0.0104	0.024	0.080	0.076	0.086	0.102
0.0505	0.061	0.069	0.052	0.070	0.056
2.844×10^{-5}	1.612×10^{-4}	2.777×10^{-3}	0.020	3.685×10^{-3}	4.278×10^{-3}
1.089×10^{-4}	3.953×10^{-4}	1.698×10^{-3}	3.270×10^{-4}	1.731×10^{-3}	5.396×10^{-4}
0.0115	0.017	0.019	0.017	0.020	9.879×10^{-3}
2.242×10^{-5}	8.339×10^{-5}	4.048×10^{-4}	6.875×10^{-5}	4.255×10^{-4}	9.907×10^{-5}
0.0041	9.389×10^{-3}	0.028	0.023	0.029	0.013
0.0365	0.039	0.014	0.069	0.013	0.046
0.0031	5.473×10^{-3}	0.011	0.017	0.012	0.010

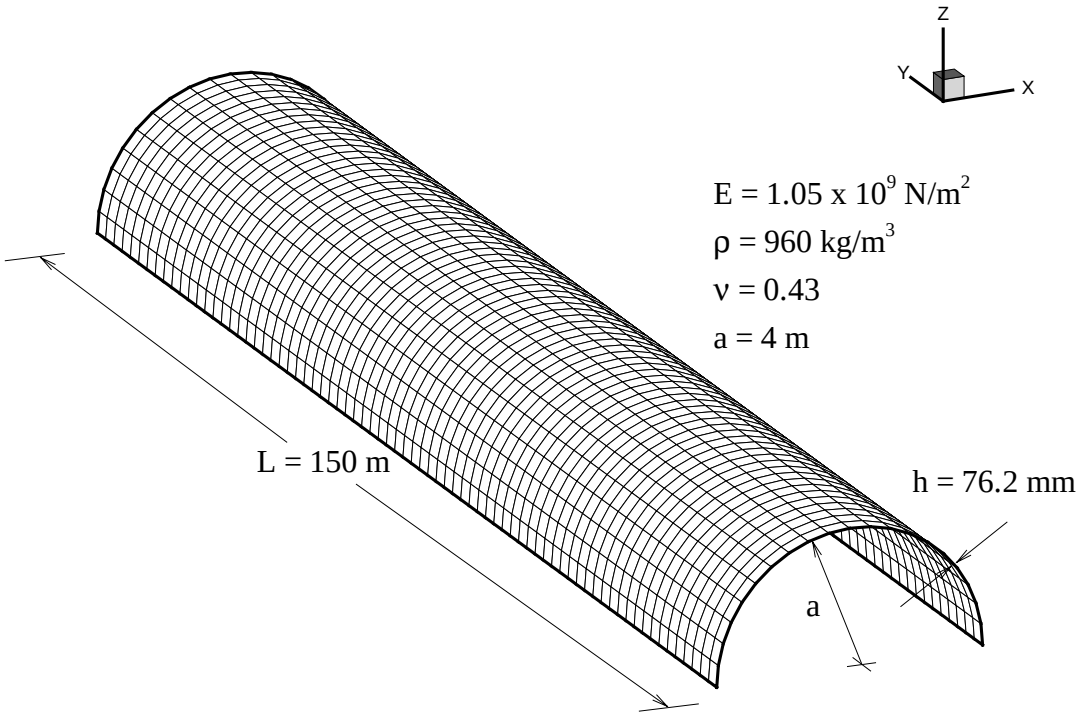

Figure 5.1 The structure of the breakwater.

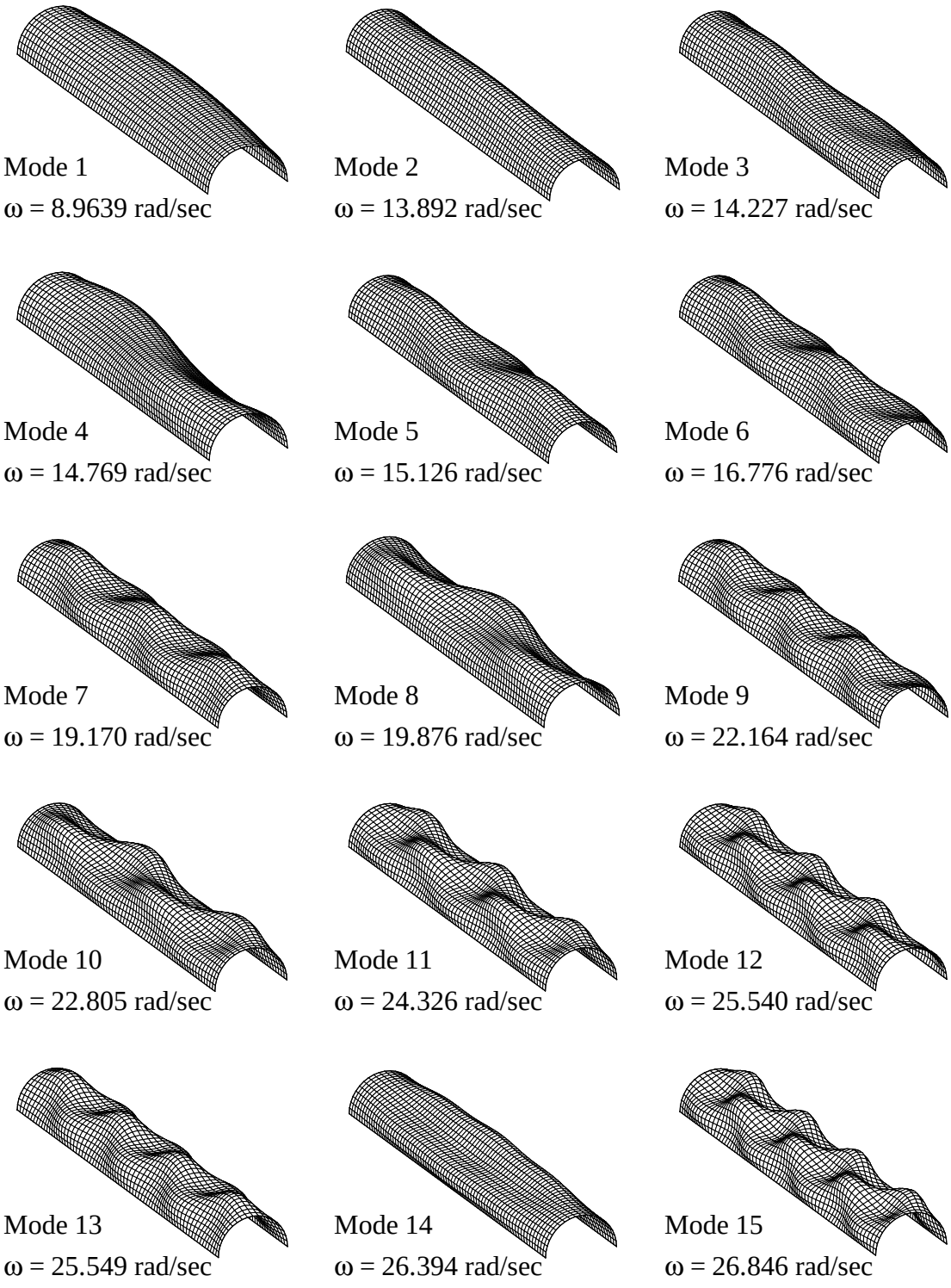

Figure 5.2 Natural “dry” mode shapes and frequencies.

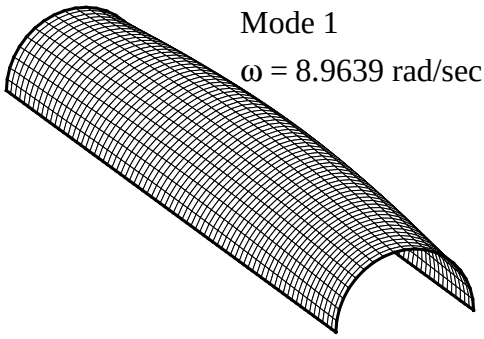

Mode 1
ω = 8.9639 rad/sec

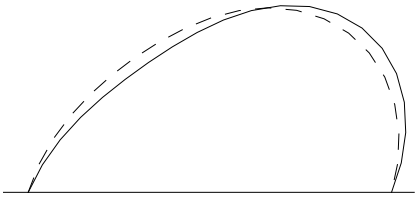

Cross sections at:
L/2 —
L/4 – –

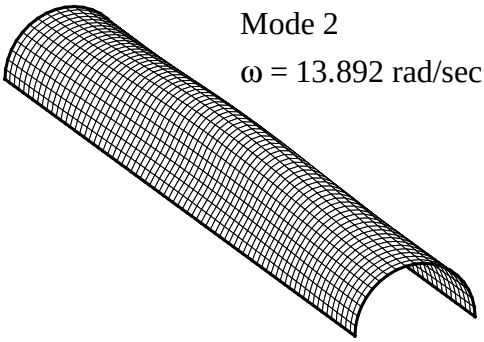

Mode 2
ω = 13.892 rad/sec

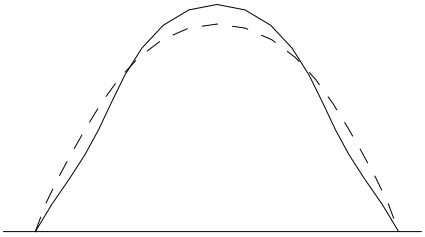

Cross sections at:
L/2 —
L/4 – –

Figure 5.3.a Natural “dry” mode shapes 1-2.

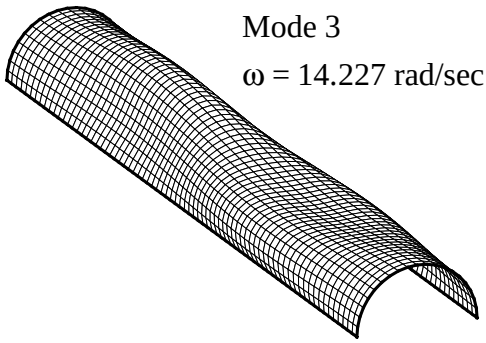

Mode 3
ω = 14.227 rad/sec

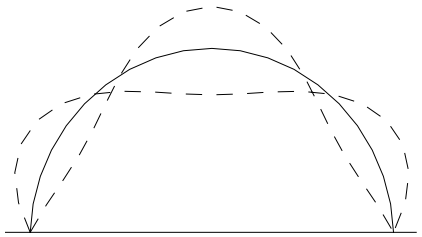

Cross sections at:
L/2 —
L/4 – –

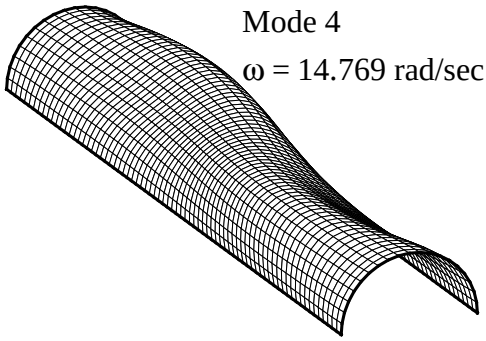

Mode 4
ω = 14.769 rad/sec

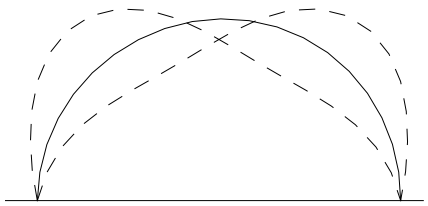

Cross sections at:
L/2 —
L/4 – –

Figure 5.3.b Natural “dry” mode shapes 3-4.

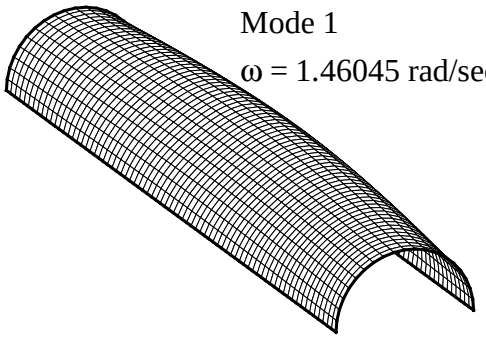

Mode 1
ω = 1.46045 rad/sec

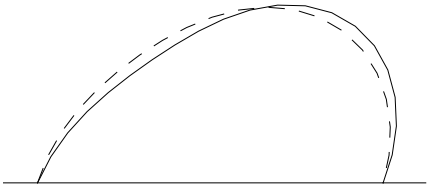

Cross sections at:
L/2 —
L/4 – –

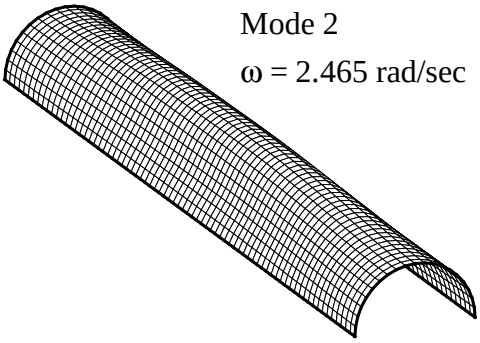

Mode 2
ω = 2.465 rad/sec

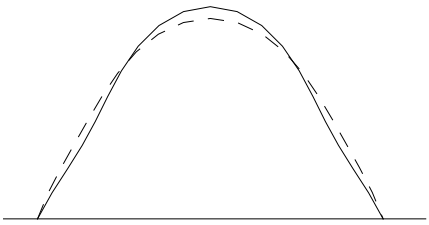

Cross sections at:
L/2 —
L/4 – –

Figure 5.4.a Natural “wet” mode shapes 1-2.

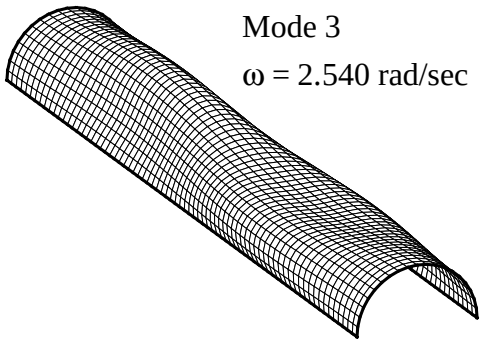

Mode 3
ω = 2.540 rad/sec

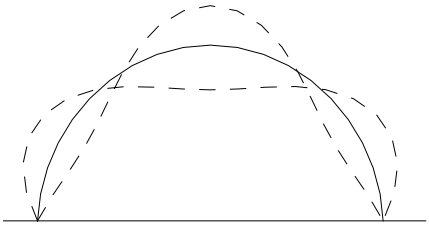

Cross sections at:
L/2 —
L/4 – –

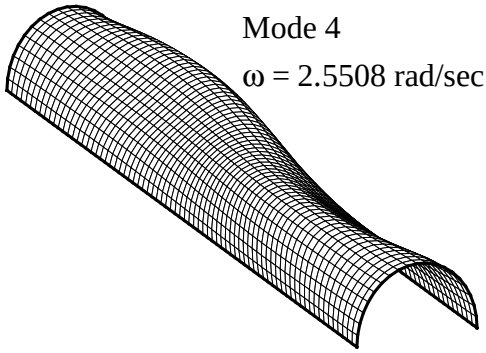

Mode 4
ω = 2.5508 rad/sec

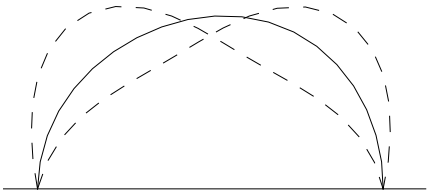

Cross sections at:
L/2 —
L/4 – –

Figure 5.4.b Natural “wet” mode shapes 3-4.

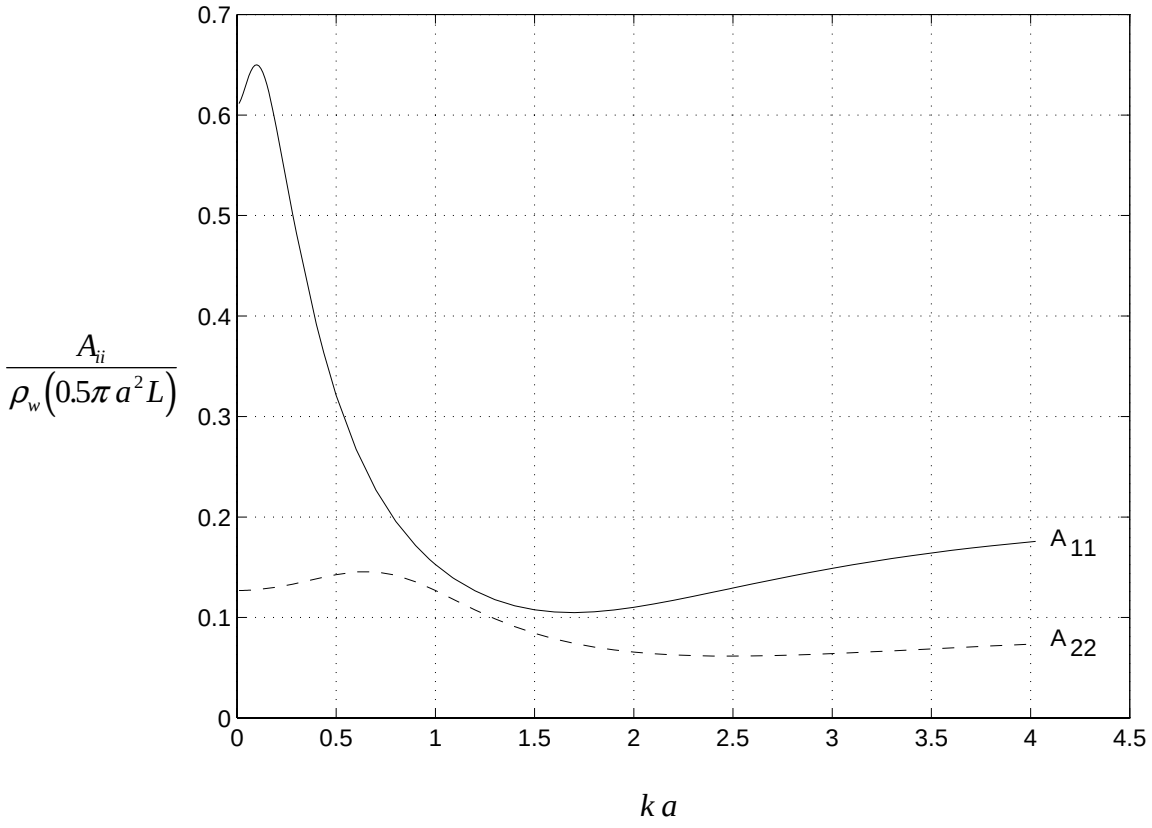

Figure 5.5 Non-dimensional added mass coefficients.

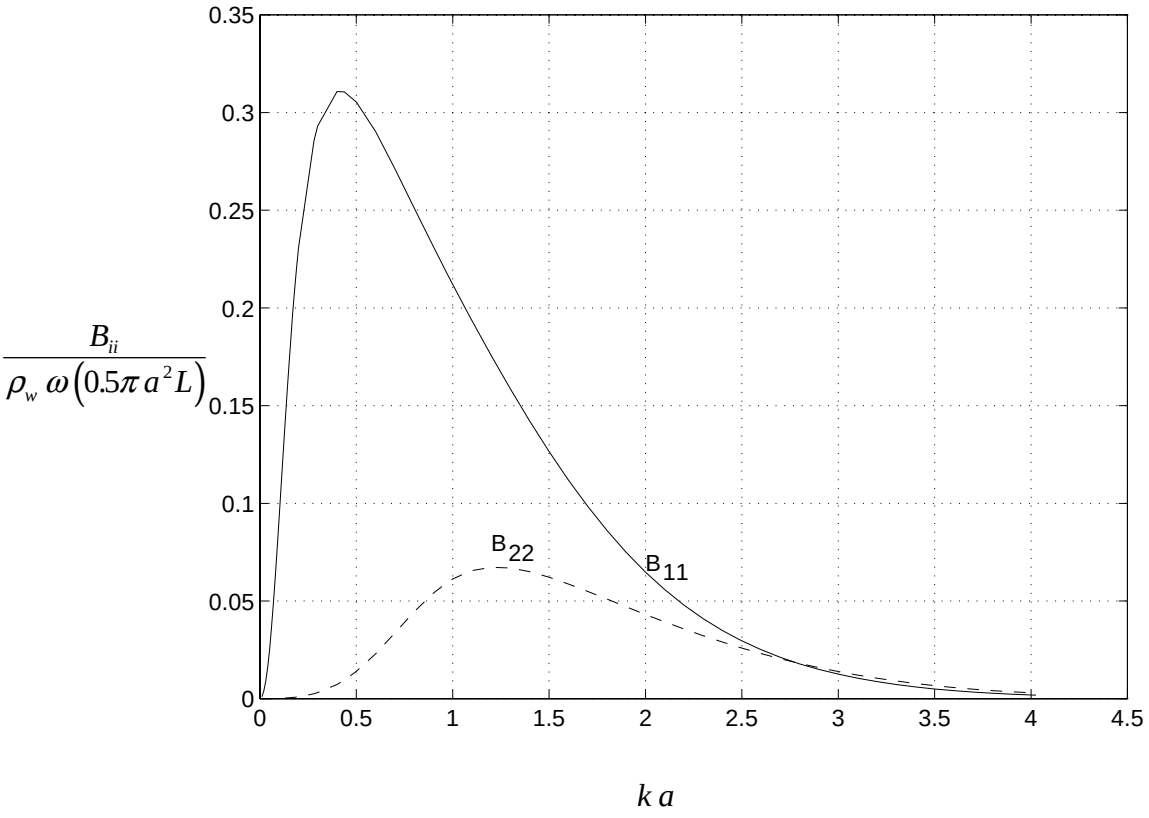

Figure 5.6 Non-dimensional damping coefficients.

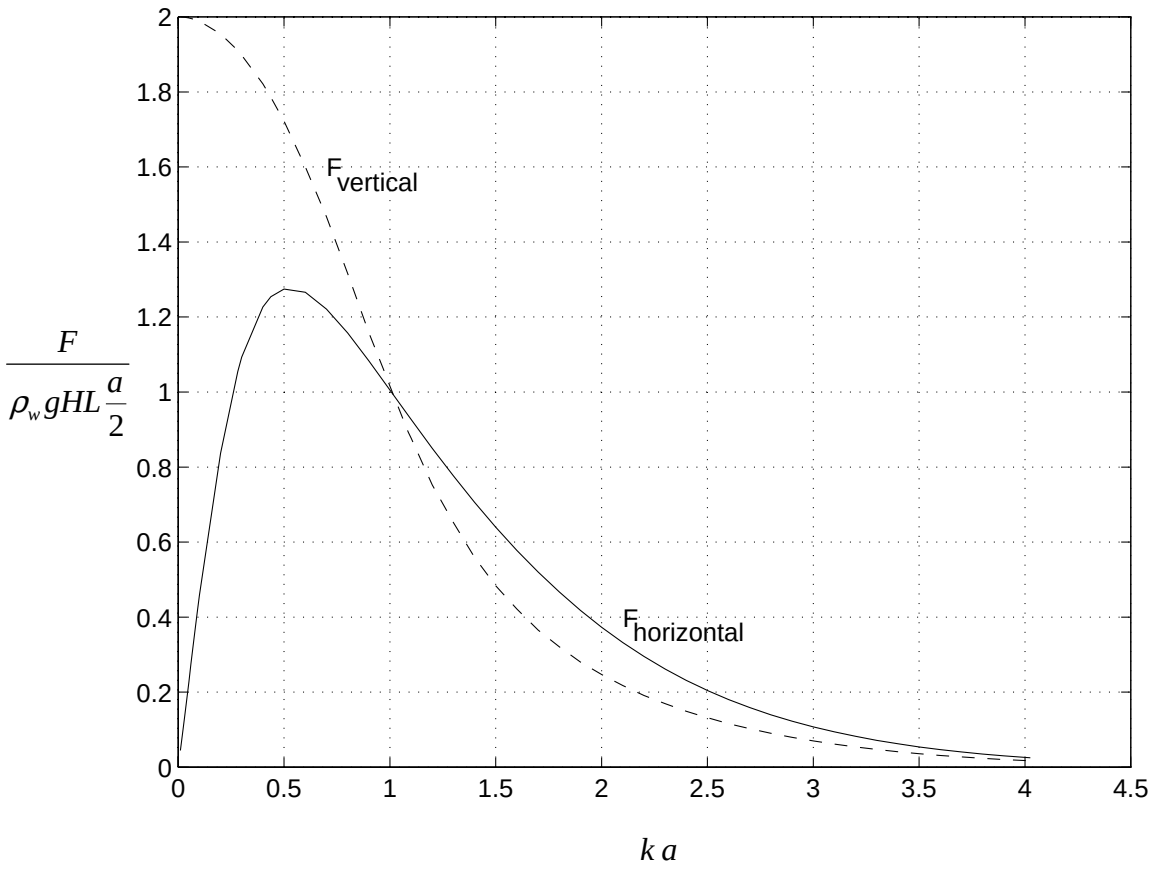

Figure 5.7 Vertical and horizontal forces for the case of normal incident waves ($\beta = 0$).

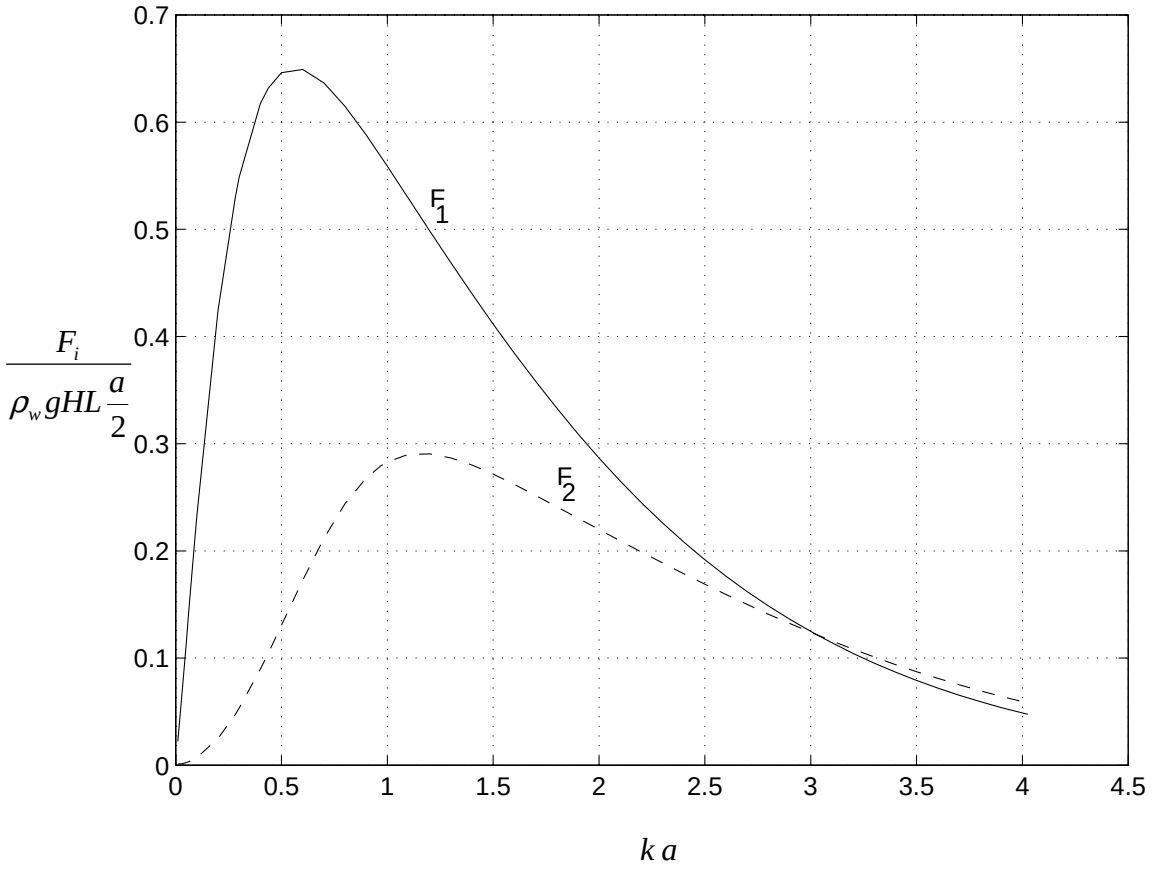

Figure 5.8 Hydrodynamic forces for modes 1 and 2 ($\beta = 0$).

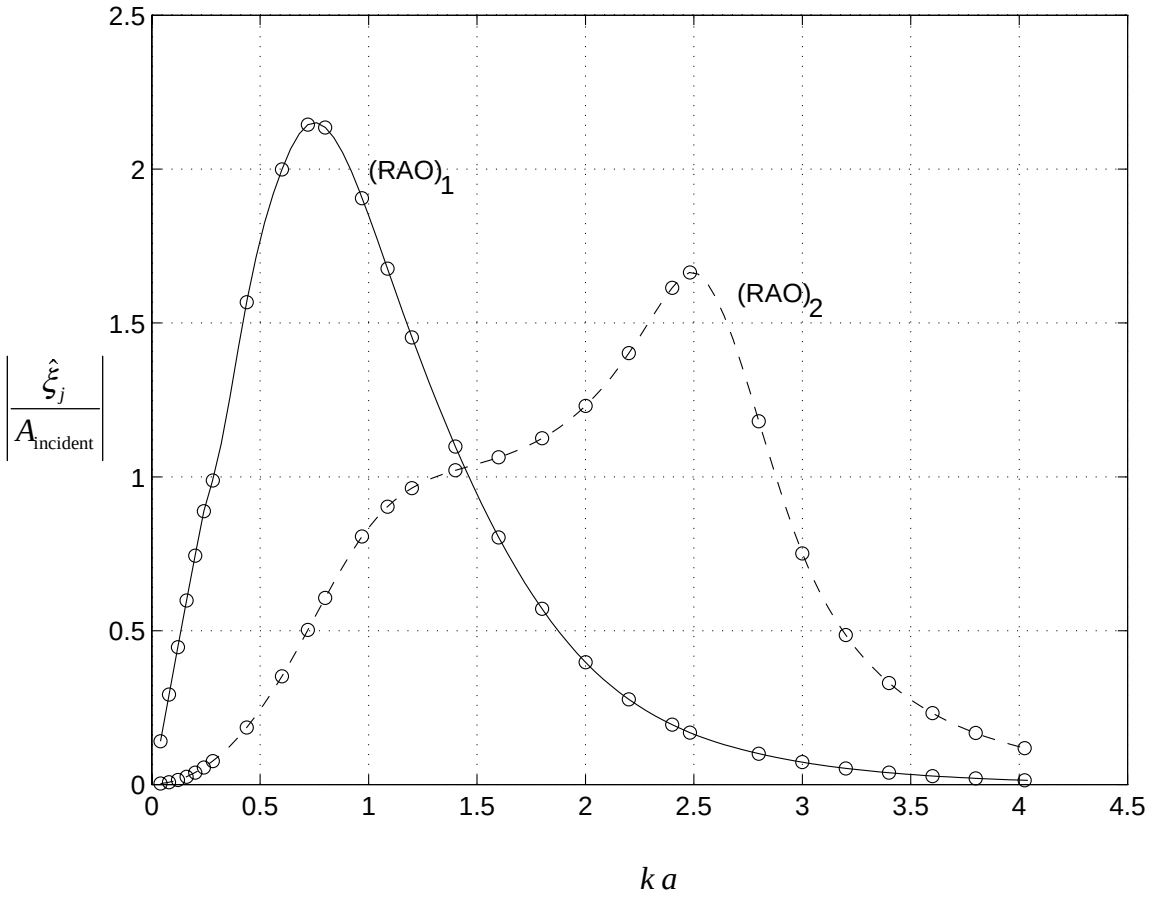

Figure 5.9 RAO for the case of normal incident waves ($\beta = 0$).

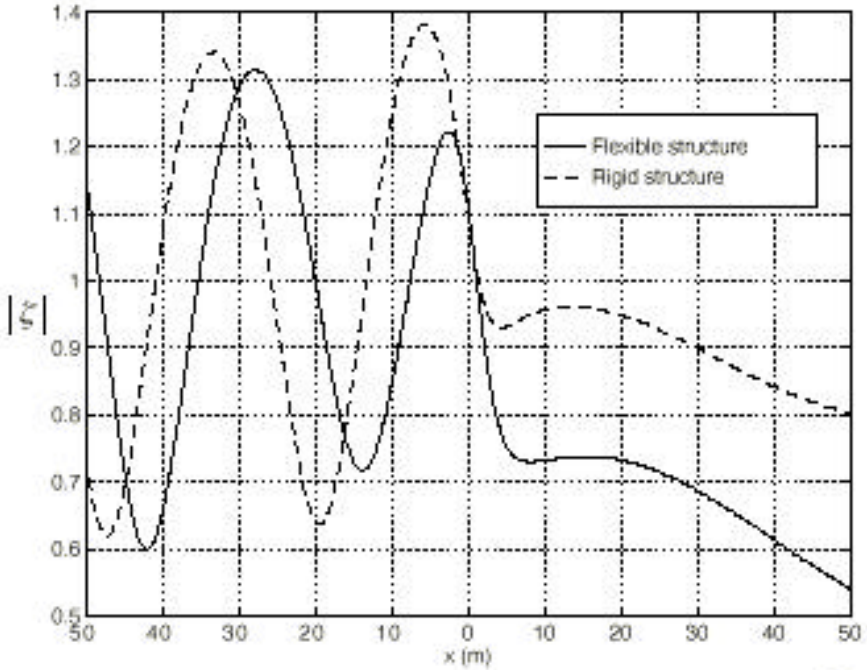

Figure 5.10.a Wave amplitude at the middle of the structure; $\omega = \frac{\pi}{4}$ rad/sec.

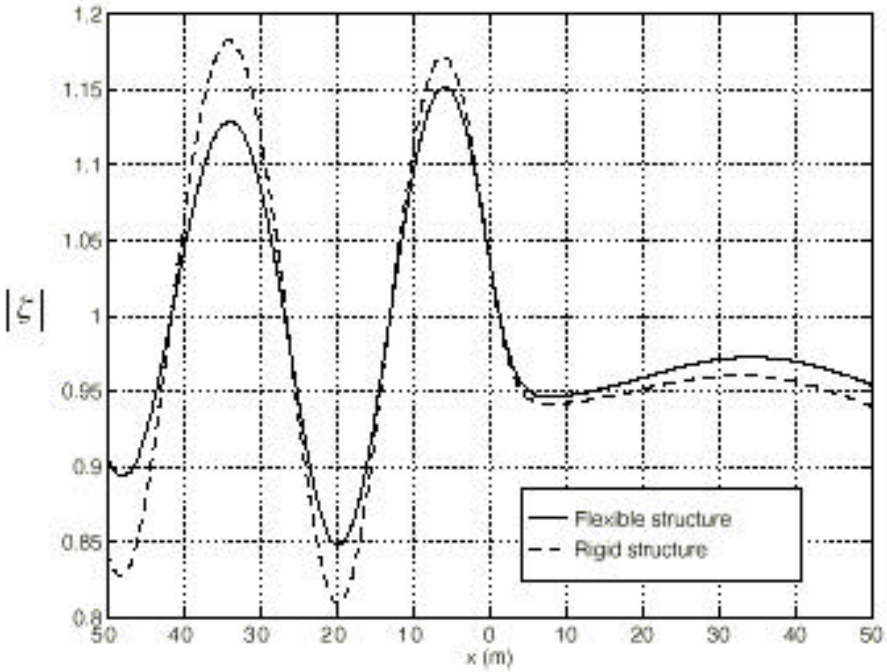

Figure 5.10.b Wave amplitude at the ends of the structure; $\omega = \frac{\pi}{4}$ rad/sec.

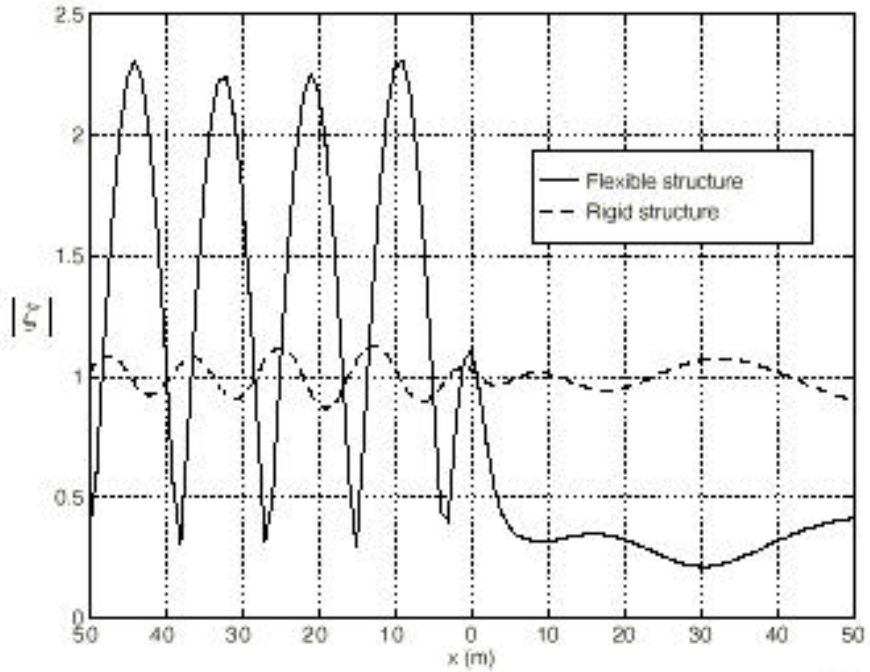

Figure 5.11.a Wave amplitude at the middle of the structure; $\omega = \frac{\pi}{2}$ rad/sec.

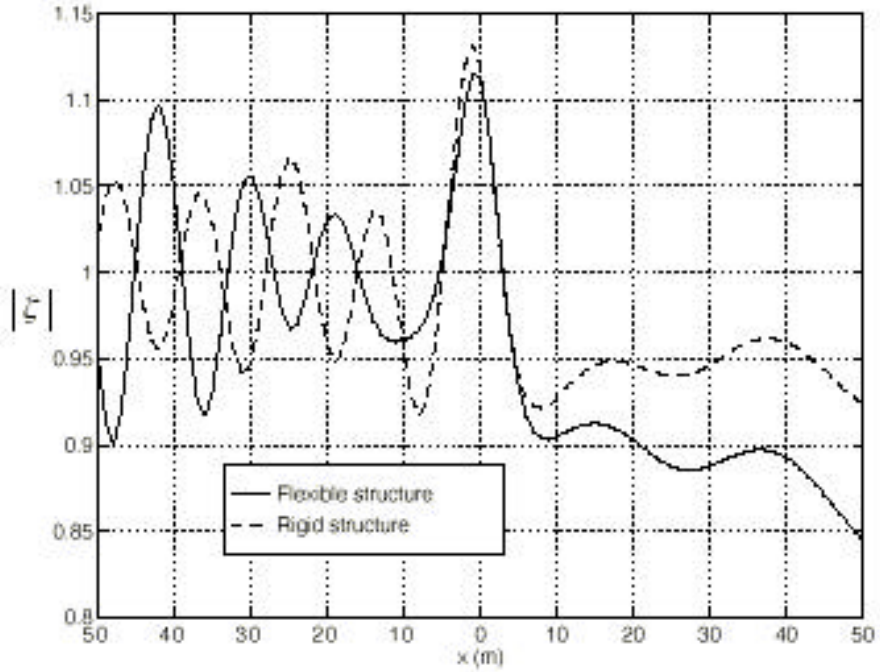

Figure 5.11.b Wave amplitude at the ends of the structure; $\omega = \frac{\pi}{2}$ rad/sec.

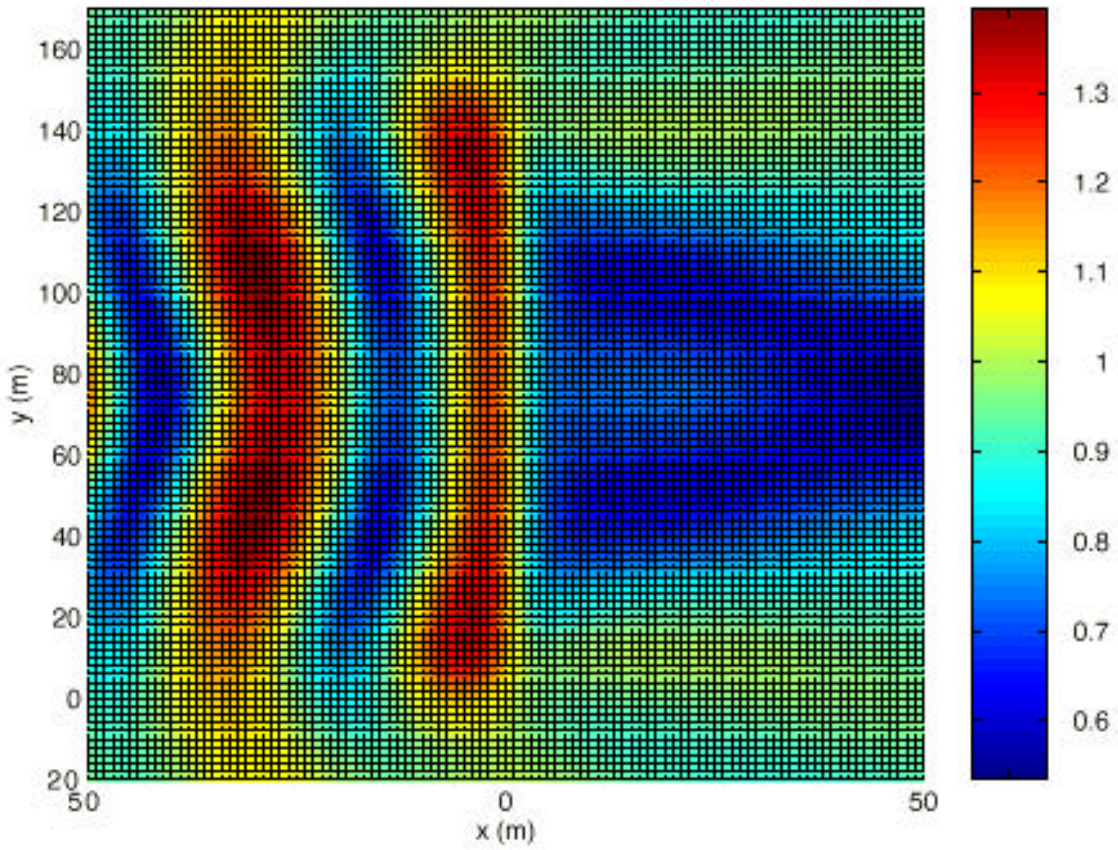

Figure 5.12 The amplitude of the free surface elevation for $\omega = \frac{\pi}{4}$ $(\beta = 0)$.

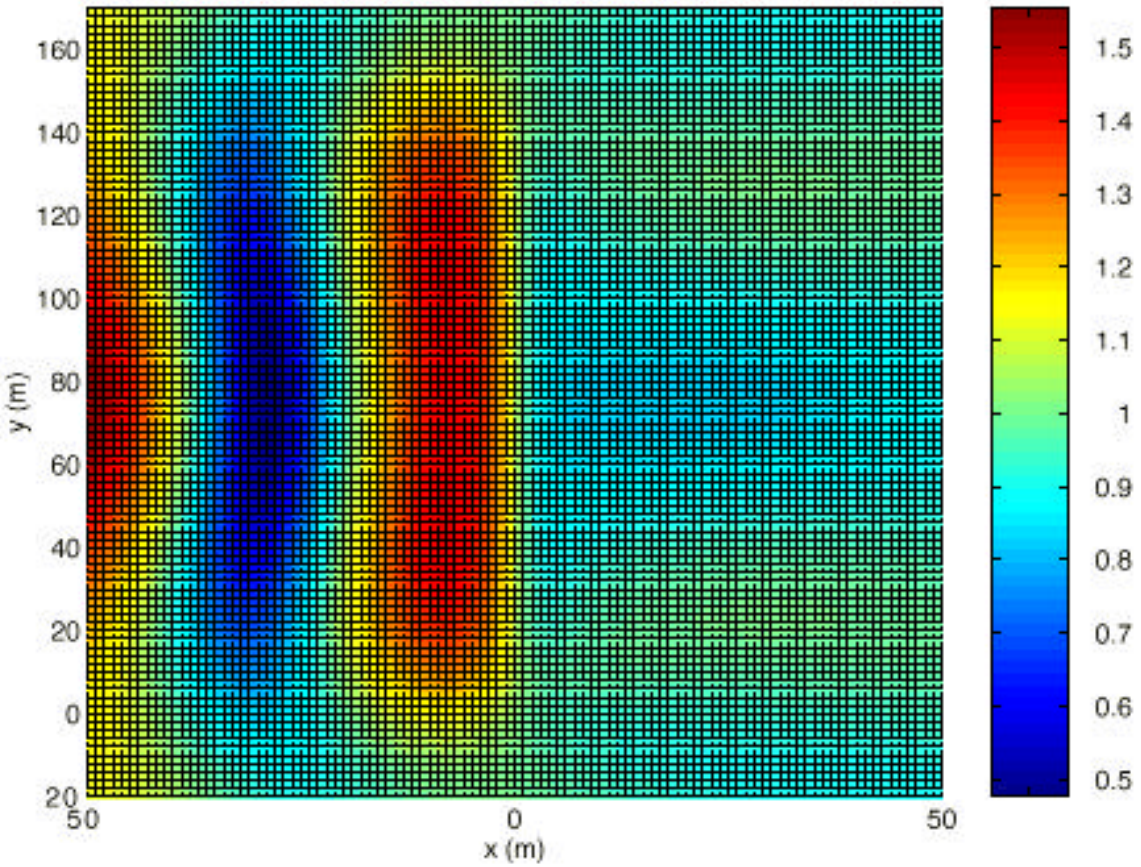

Figure 5.13 The amplitude of the free surface elevation for $\omega = \frac{\pi}{6}$ $(\beta = 0)$.

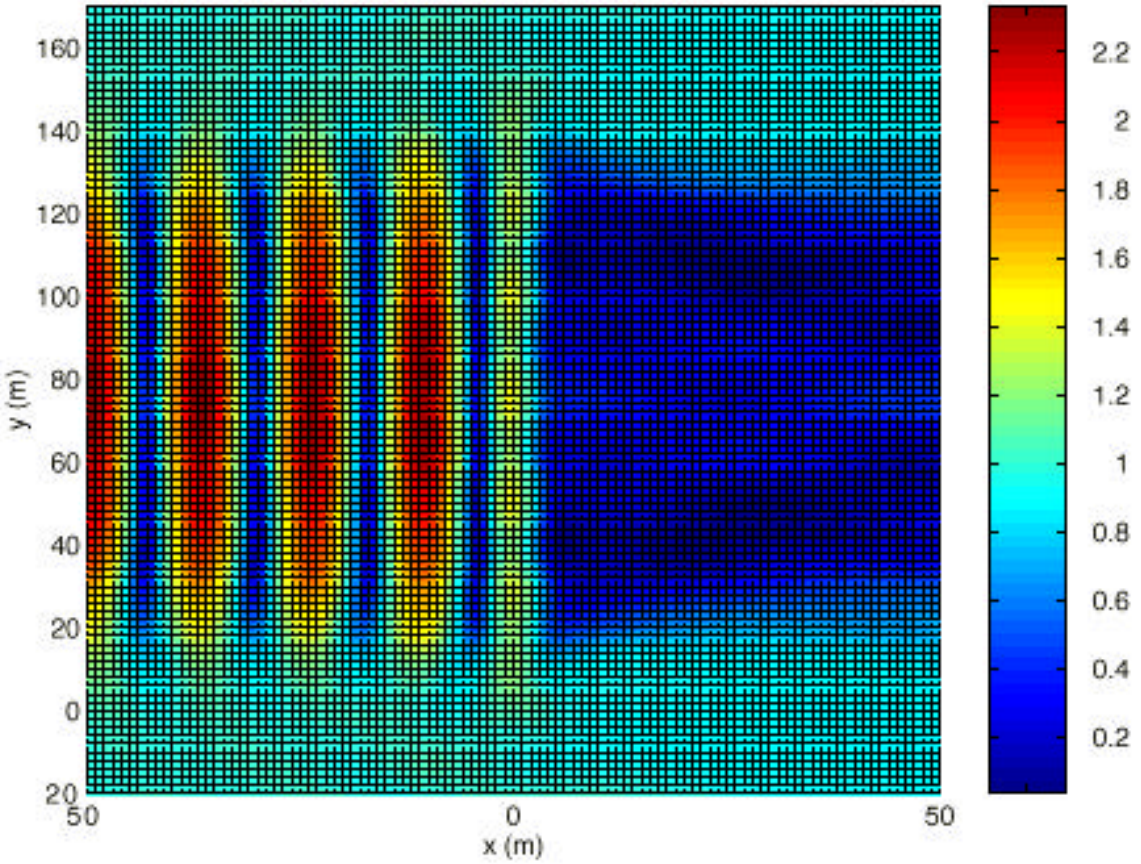

Figure 5.14 The amplitude of the free surface elevation for $\omega = \omega_{n_{max}} (\beta = 0)$.

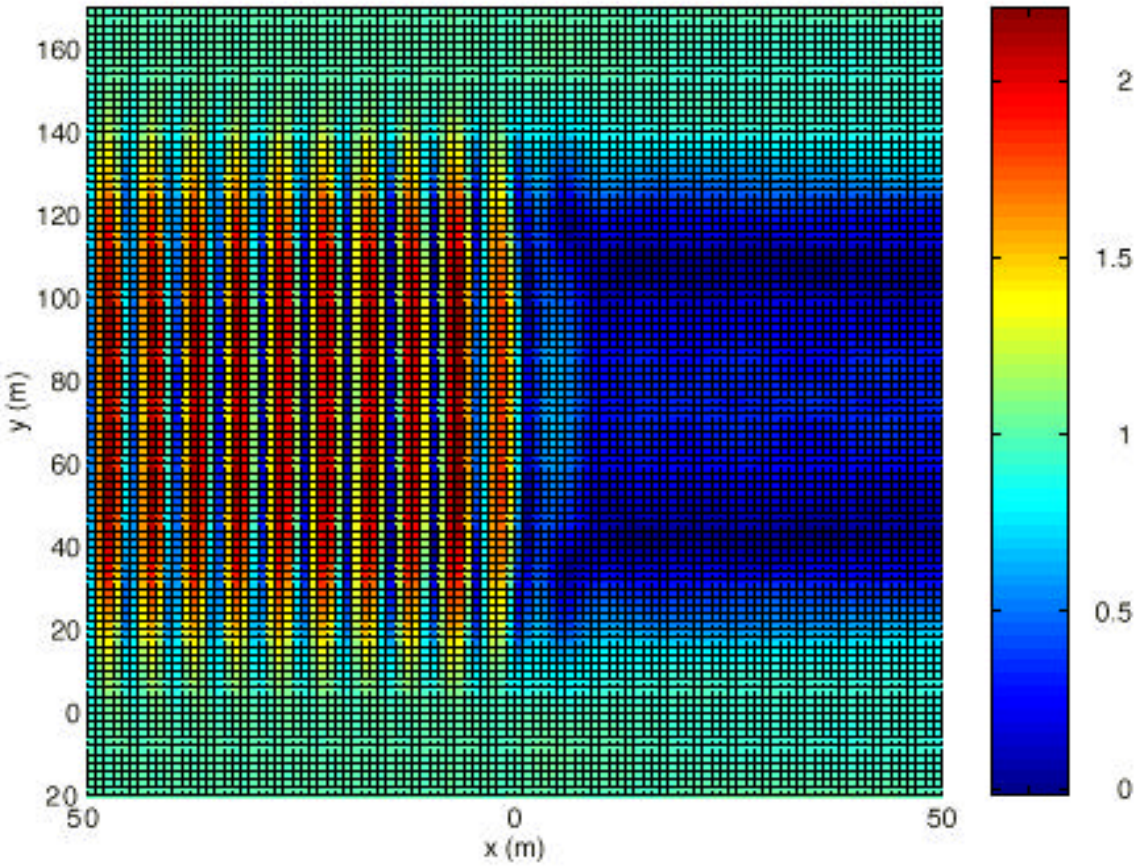

Figure 5.15 The amplitude of the free surface elevation for $\omega = \omega_{n_{max}} (\beta = 0)$.

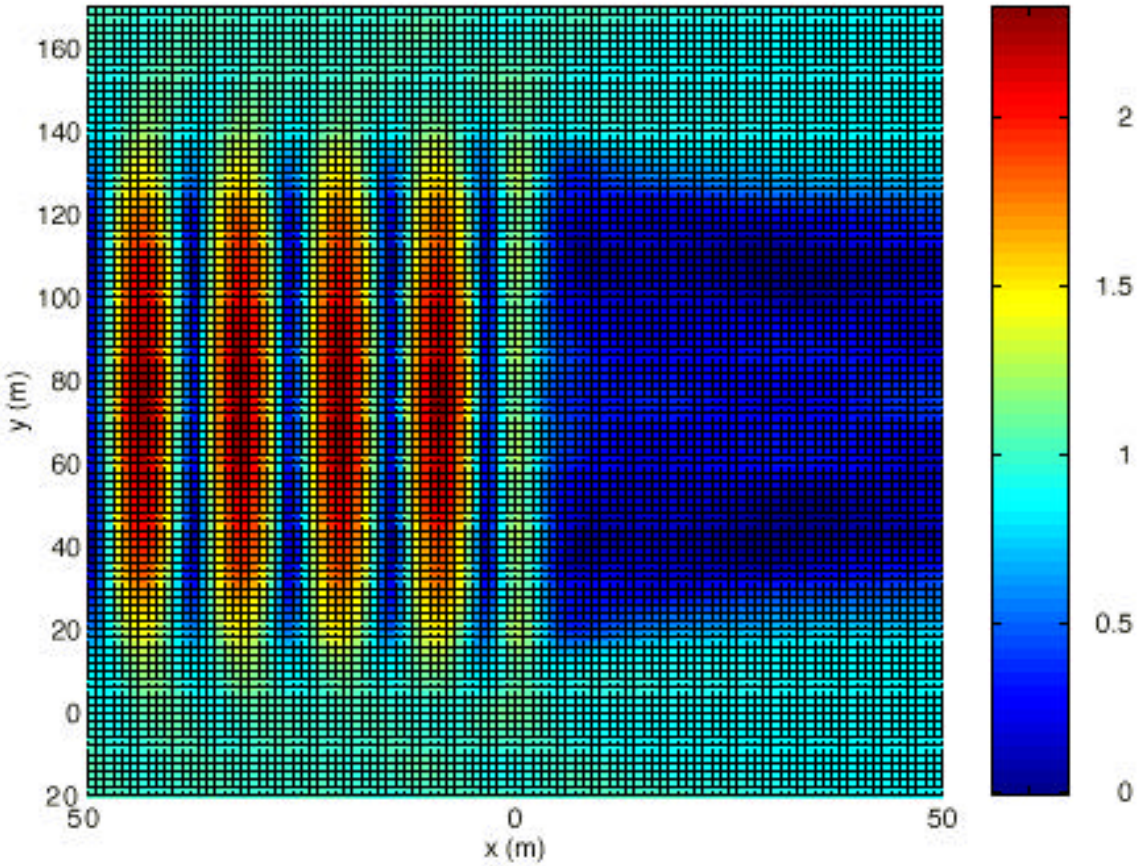

Figure 5.16 The amplitude of the free surface elevation for $\omega = \frac{\pi}{2}$ $(\beta = 0)$.

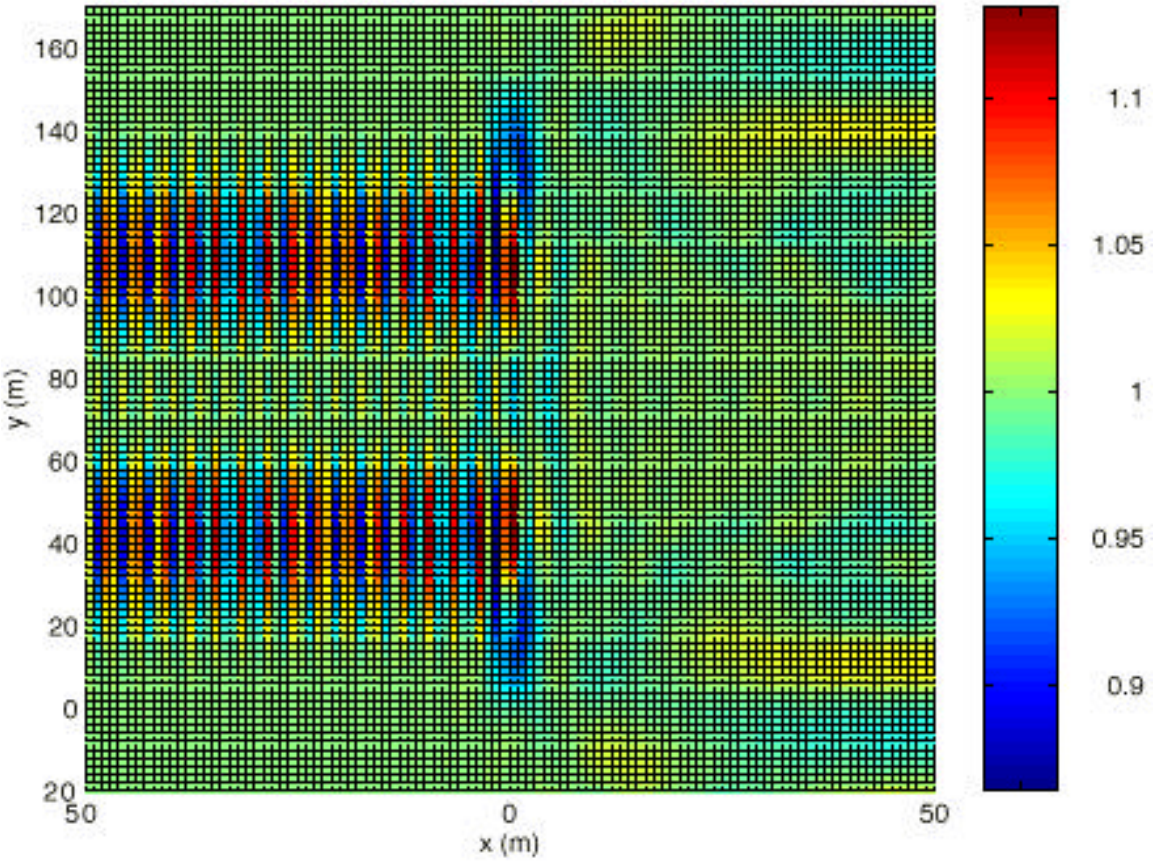

Figure 5.17 The amplitude of the free surface elevation for $\omega = \pi$ $(\beta = 0)$.

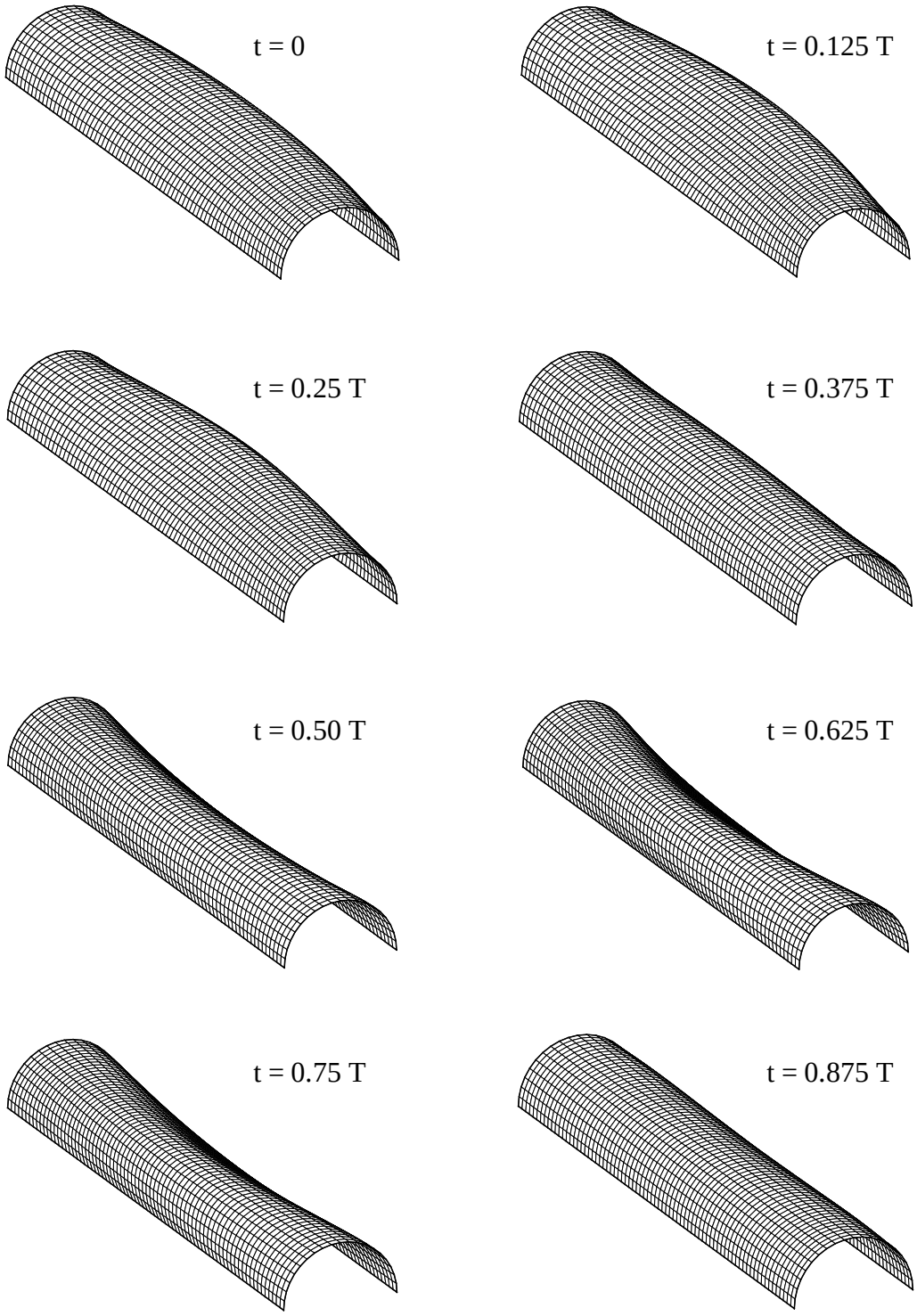

Figure 5.18 Displacements of structure over time for $A_{\text{incident}} = 1$ ($\omega = \frac{\pi}{4}$, $\beta = 0$).

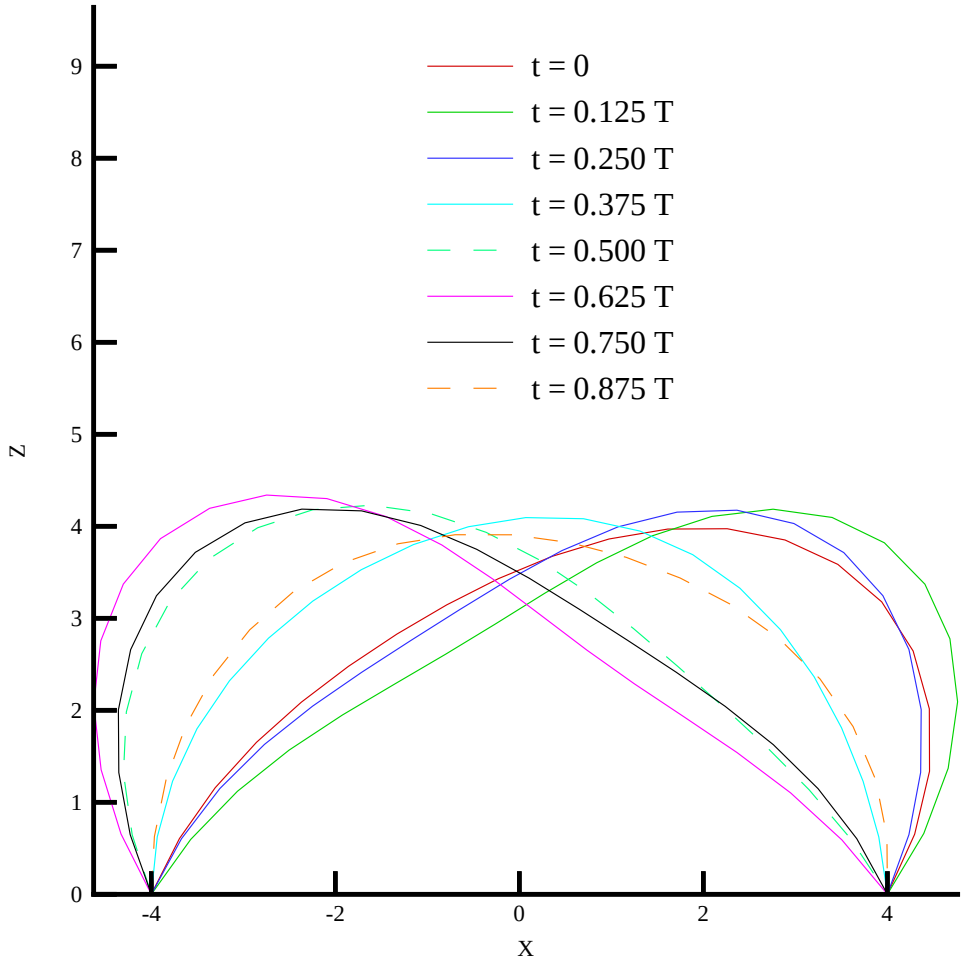

Figure 5.19 Mid-section displacements over time for $A_{\text{incident}} = 1$ ($\omega = \frac{\pi}{4}$, $\beta = 0$).

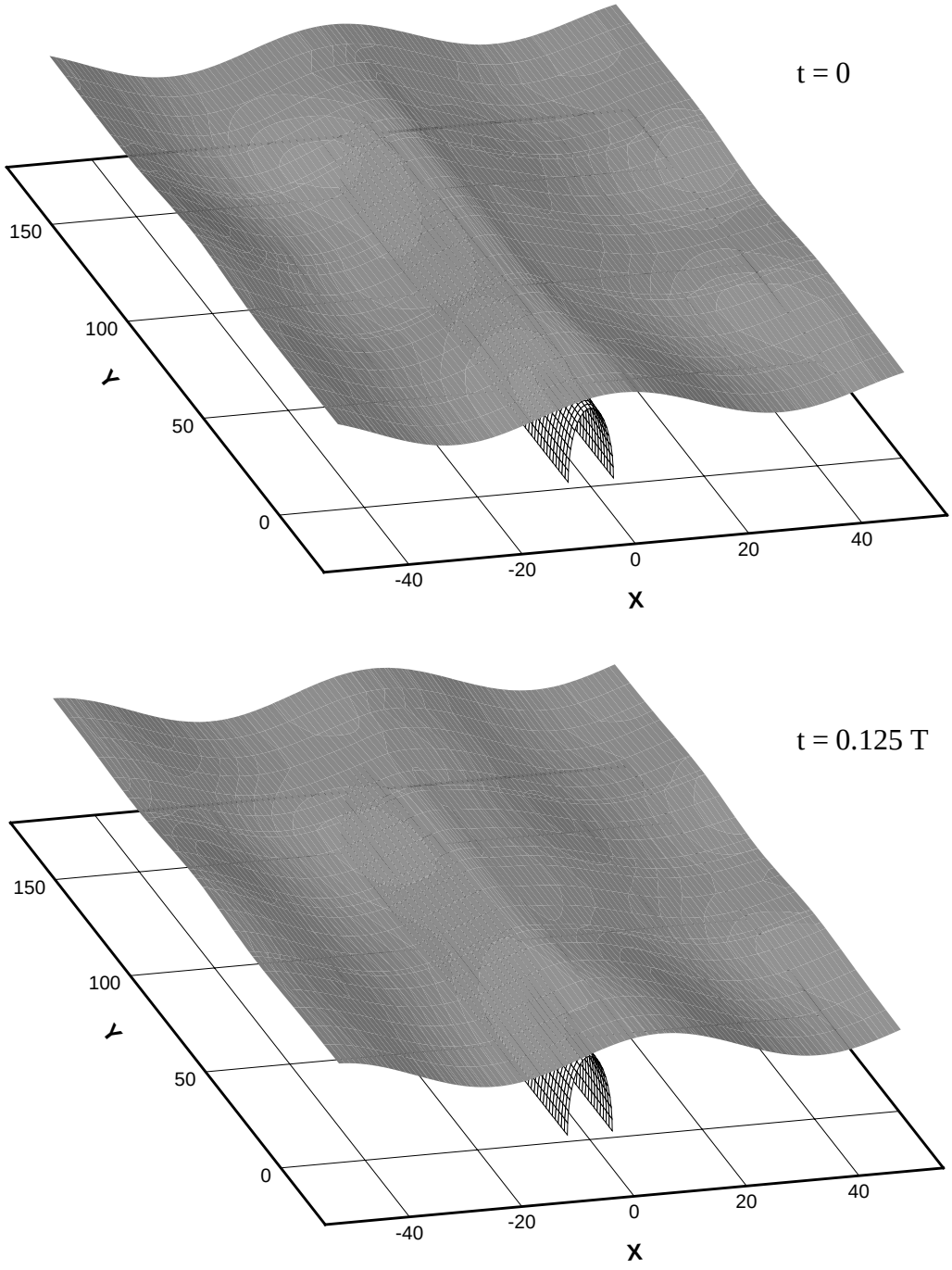

Figure 5.20.a Free surface elevation ($\omega = \frac{\pi}{4}$, $\beta = 0$).

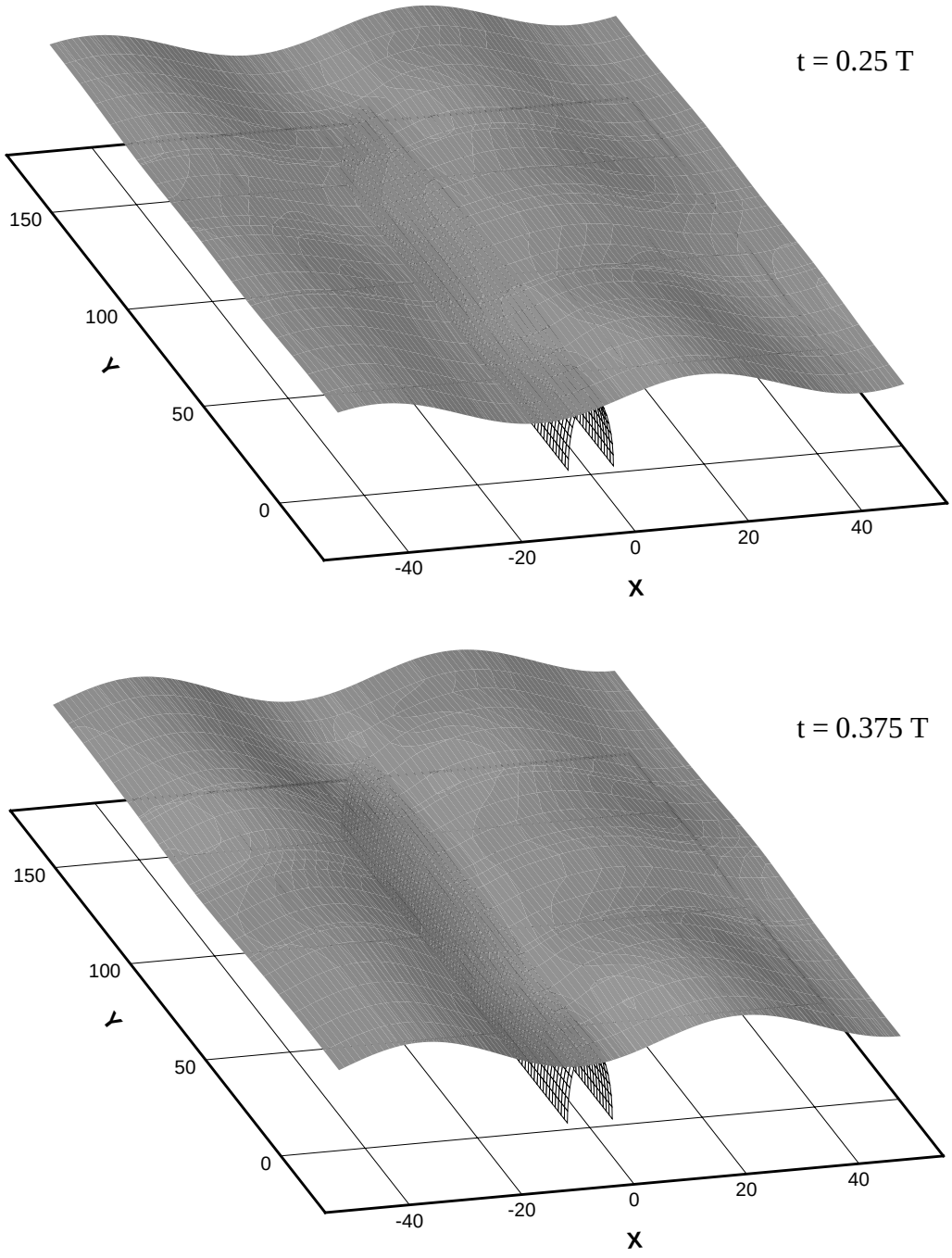

Figure 5.20.b Free surface elevation ($\omega = \frac{\pi}{4}$, $\beta = 0$).

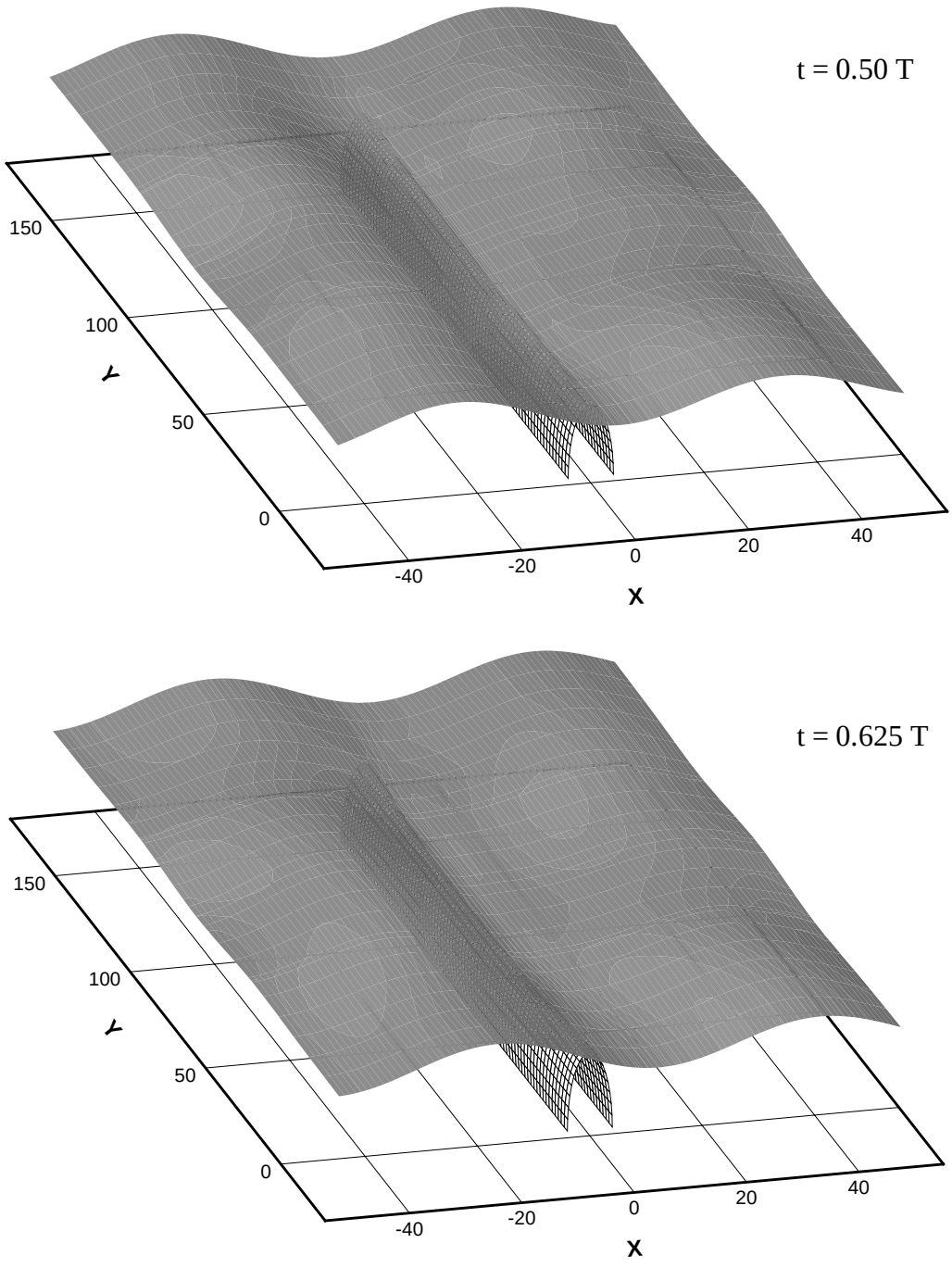

Figure 5.20.c Free surface elevation ($\omega = \frac{\pi}{4}$, $\beta = 0$).

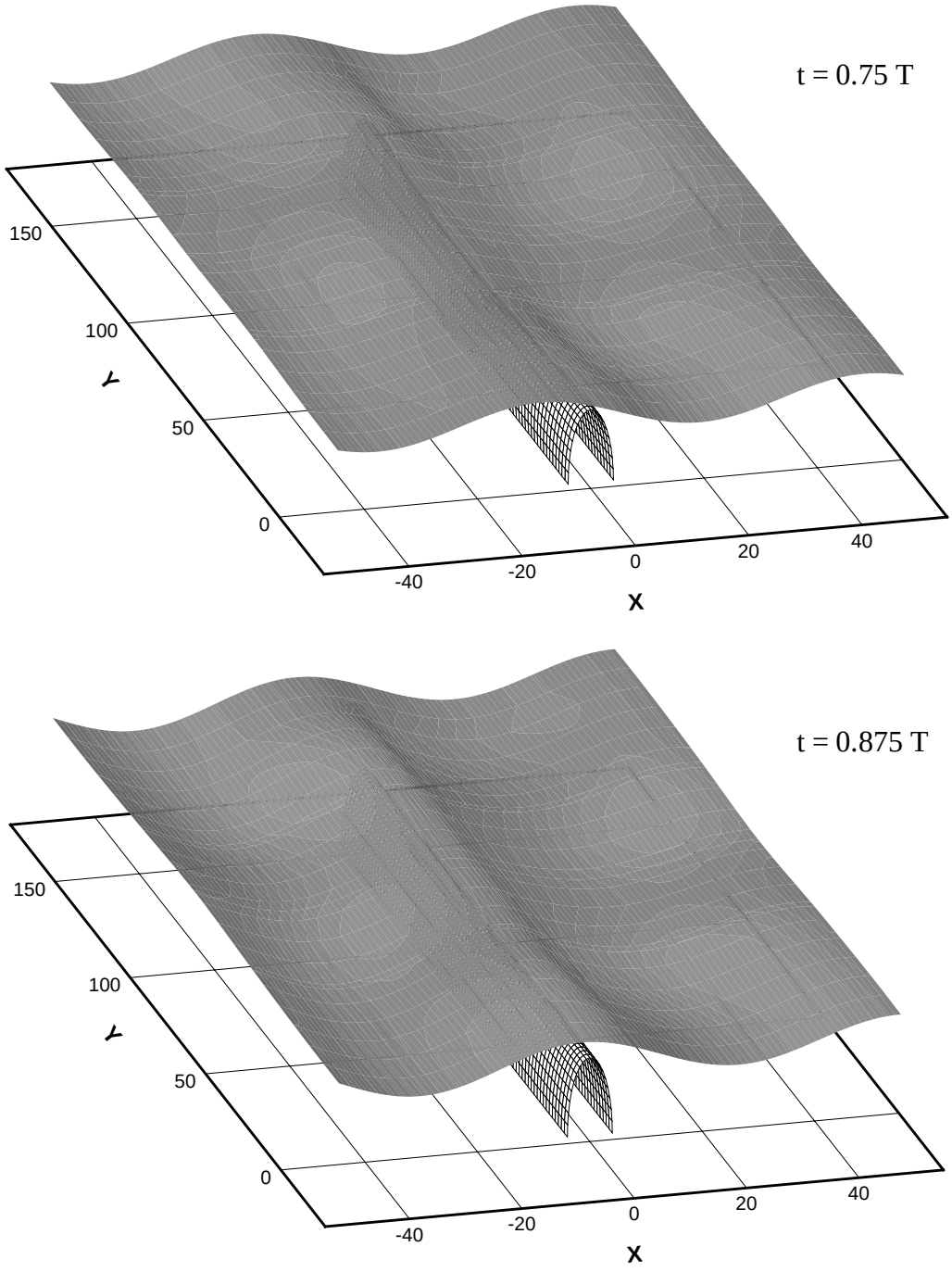

Figure 5.20.d Free surface elevation ($\omega = \frac{\pi}{4}$, $\beta = 0$).

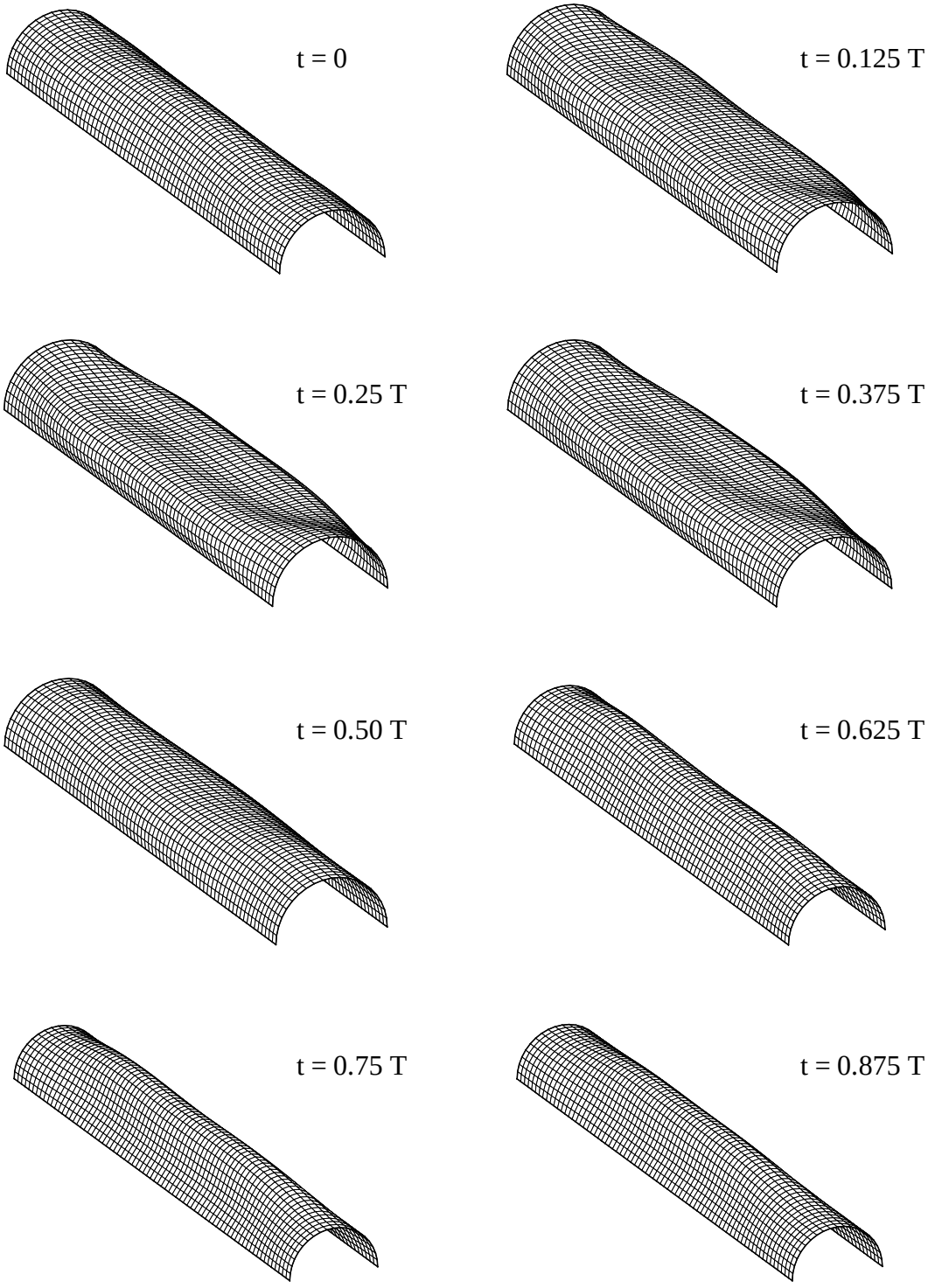

Figure 5.21 Displacements of structure over time for $A_{\text{incident}} = 1$ ($\omega = \omega_{n_2}$, $\beta = 0$).

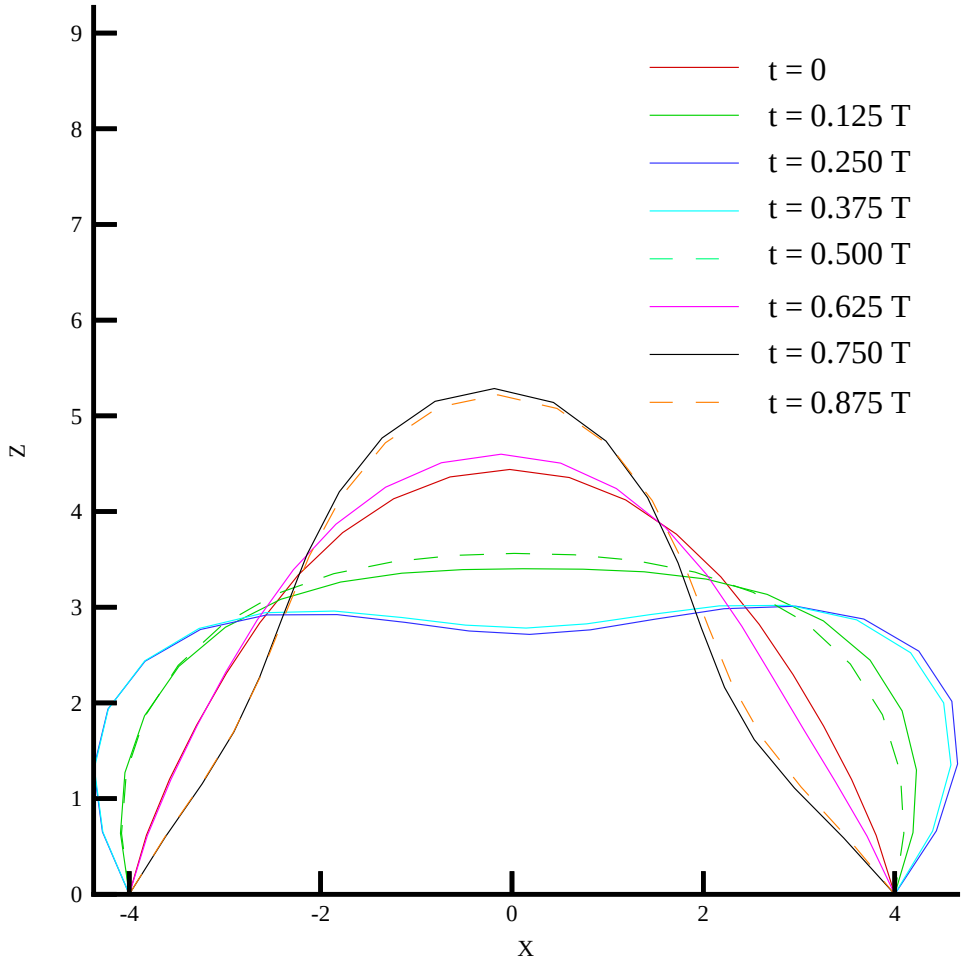

Figure 5.22 Mid-section displacements over time for $A_{\text{incident}} = 1$ ($\omega = \omega_{n_2}$, $\beta = 0$).

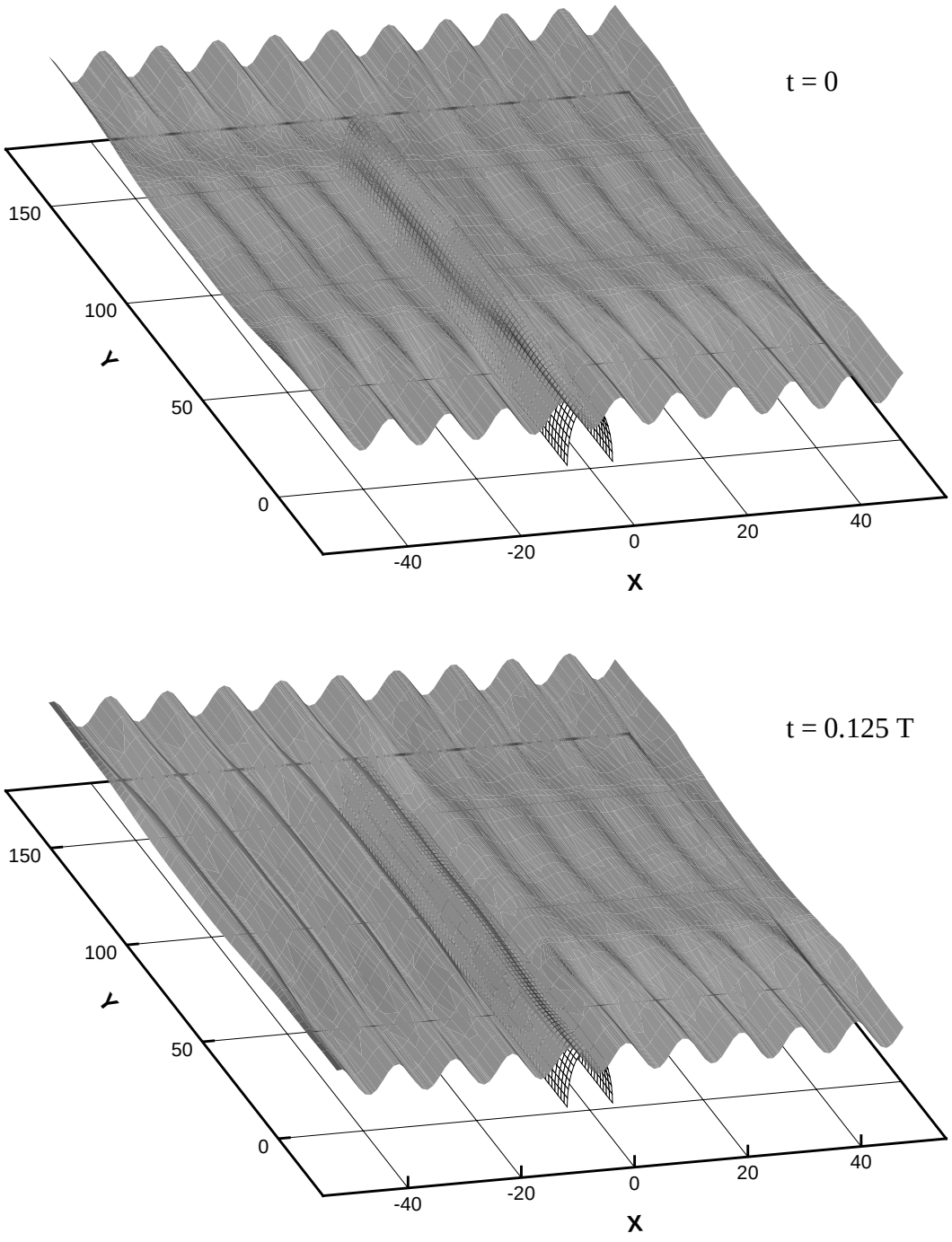

Figure 5.23.a Free surface elevation ($\omega = \omega_{n_2}$, $\beta = 0$).

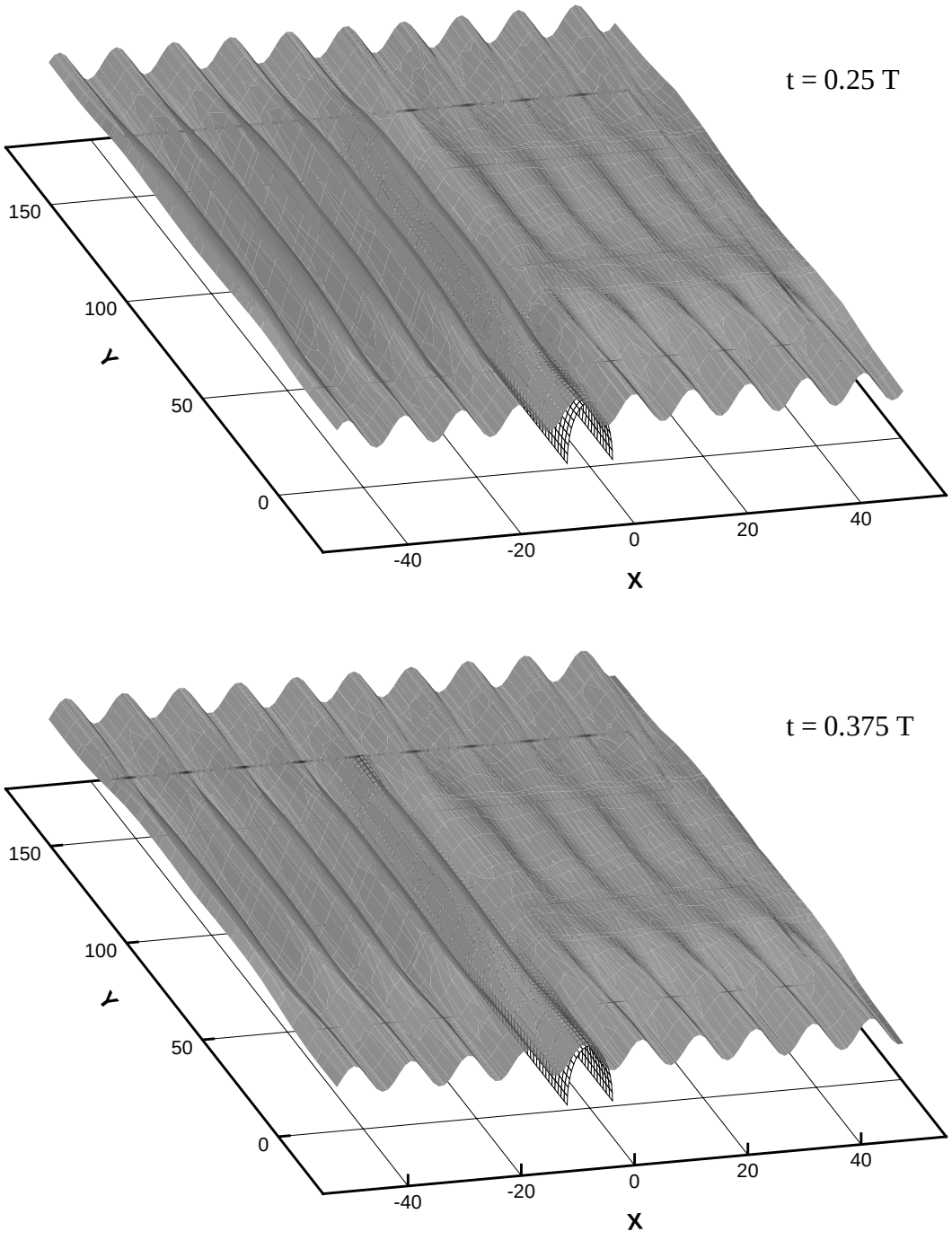

Figure 5.23.b Free surface elevation ($\omega = \omega_{n_2}$, $\beta = 0$).

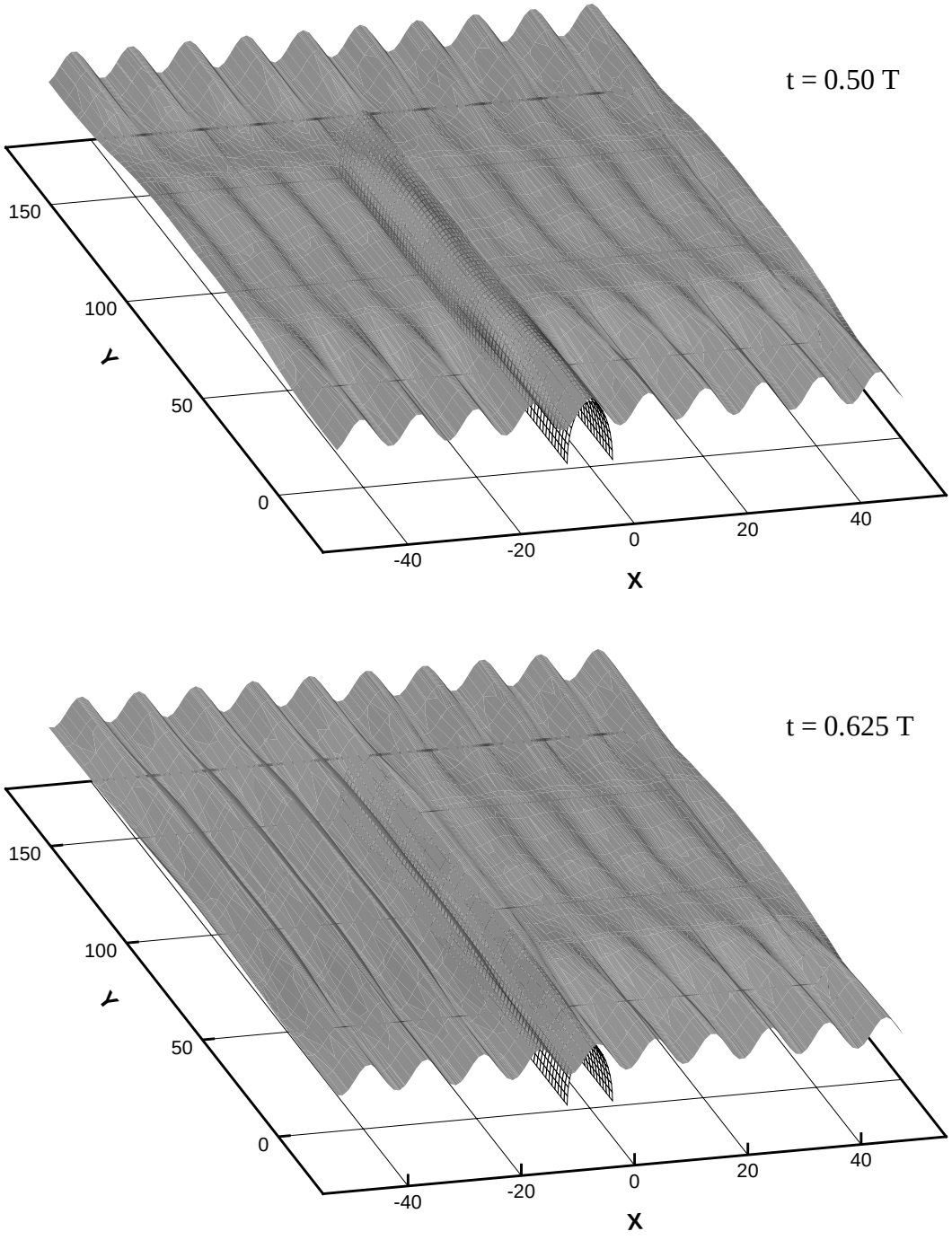

Figure 5.23.c Free surface elevation ($\omega = \omega_{n_2}$, $\beta = 0$).

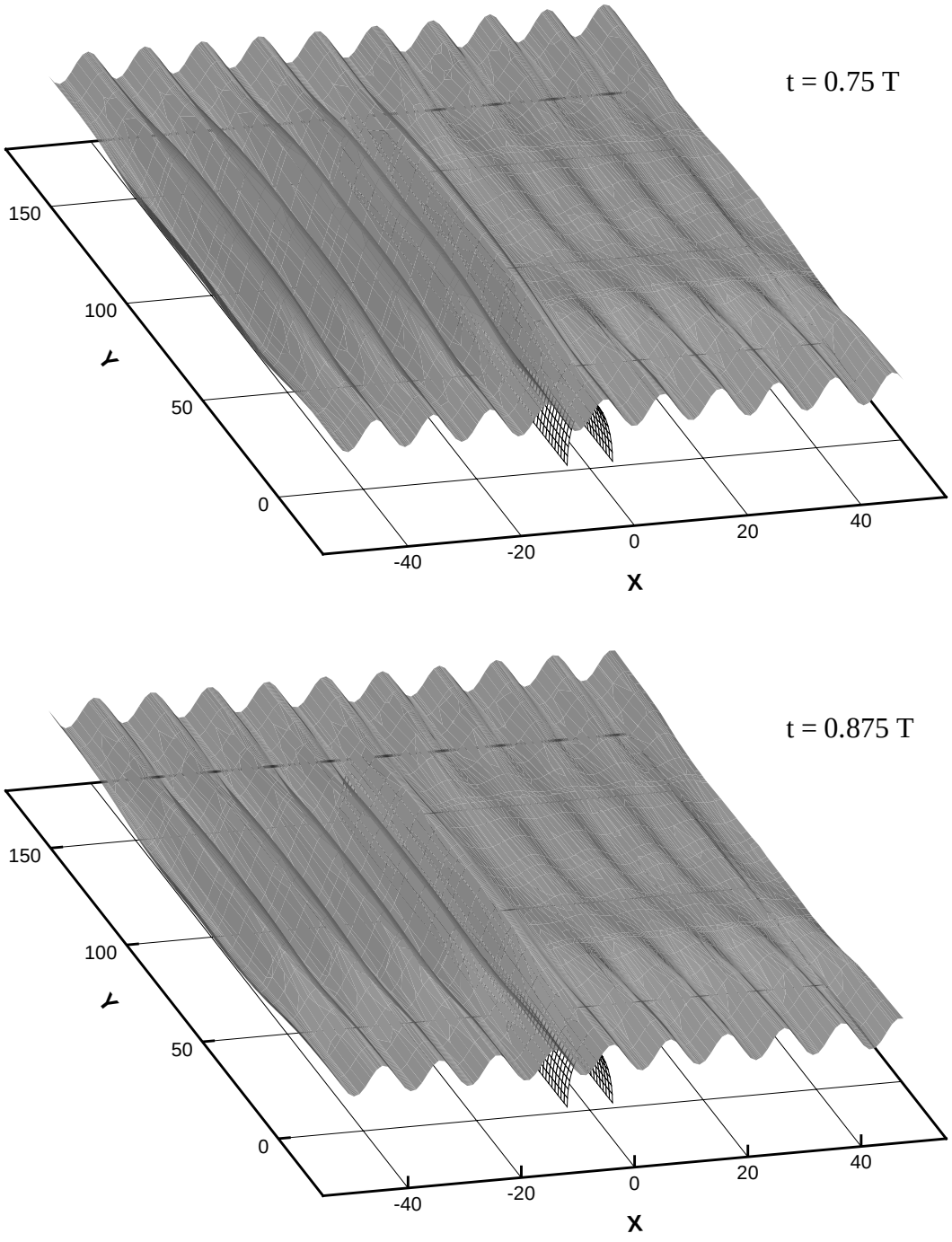

Figure 5.23.d Free surface elevation ($\omega = \omega_{n_2}$, $\beta = 0$).

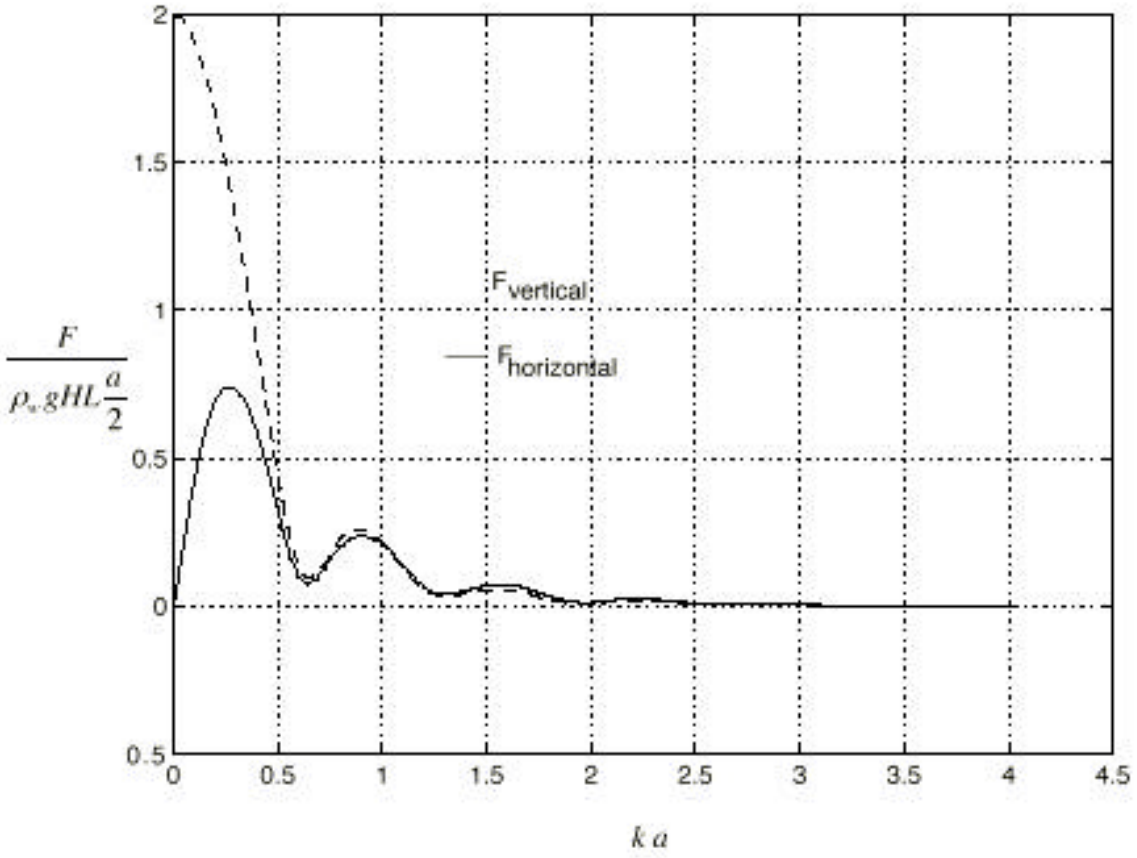

Figure 5.24 Vertical and horizontal forces for the case of oblique incident waves ($\beta = 15^{\circ}$).

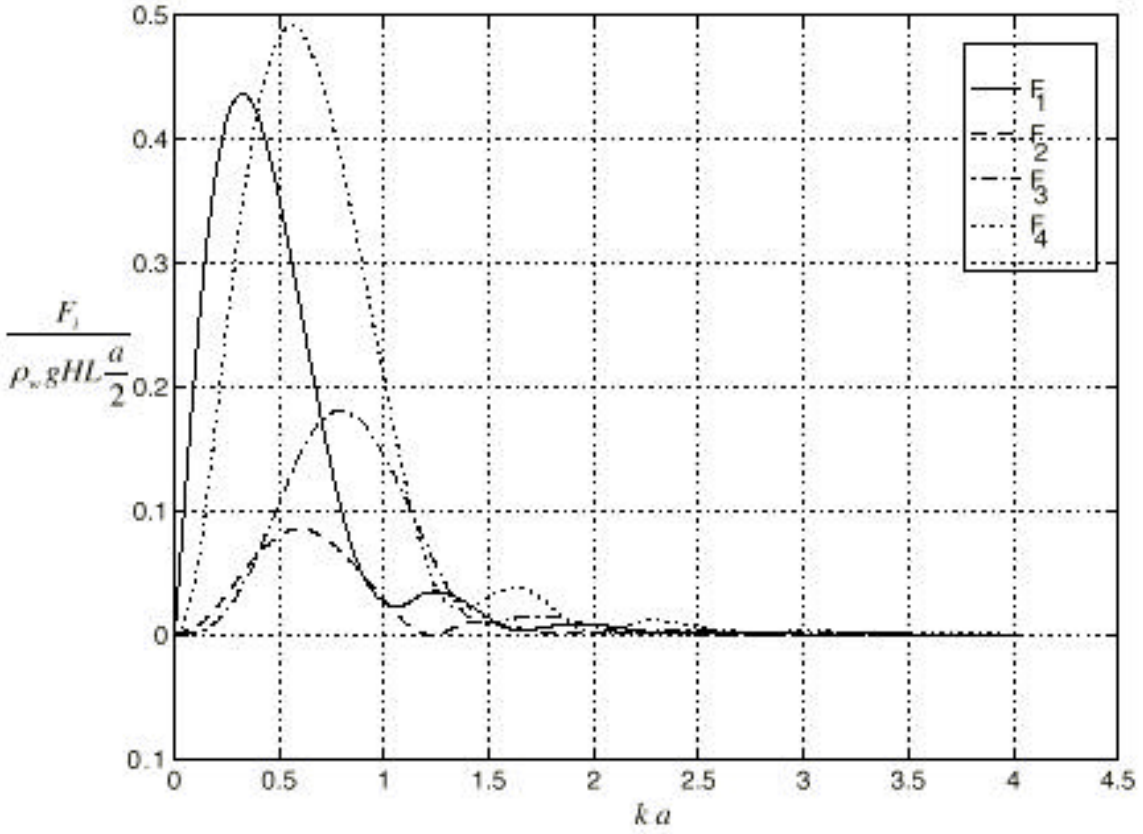

Figure 5.25 Hydrodynamic forces for modes 1, 2, 3 and 4 ($\beta = 15°$).

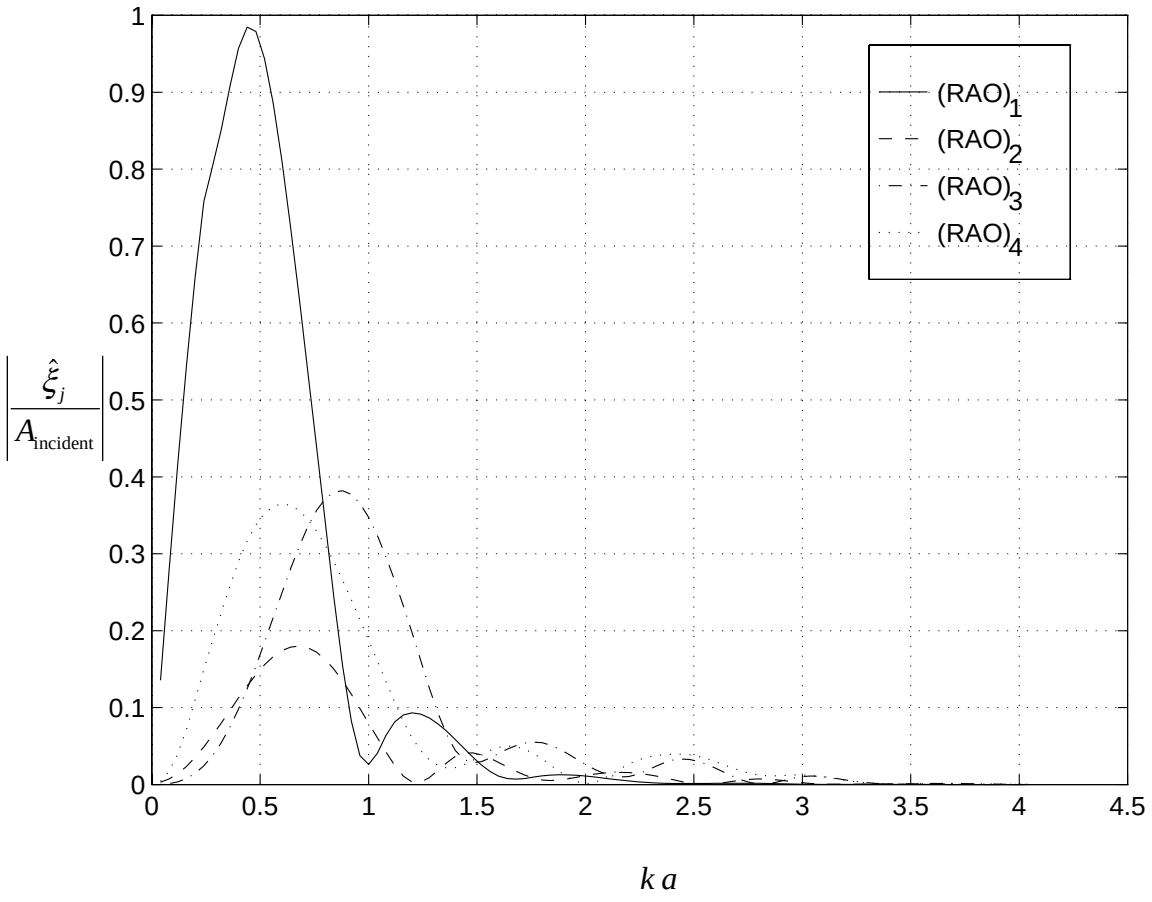

Figure 5.26 RAO for the case of oblique incident waves ($\beta = 15°$).

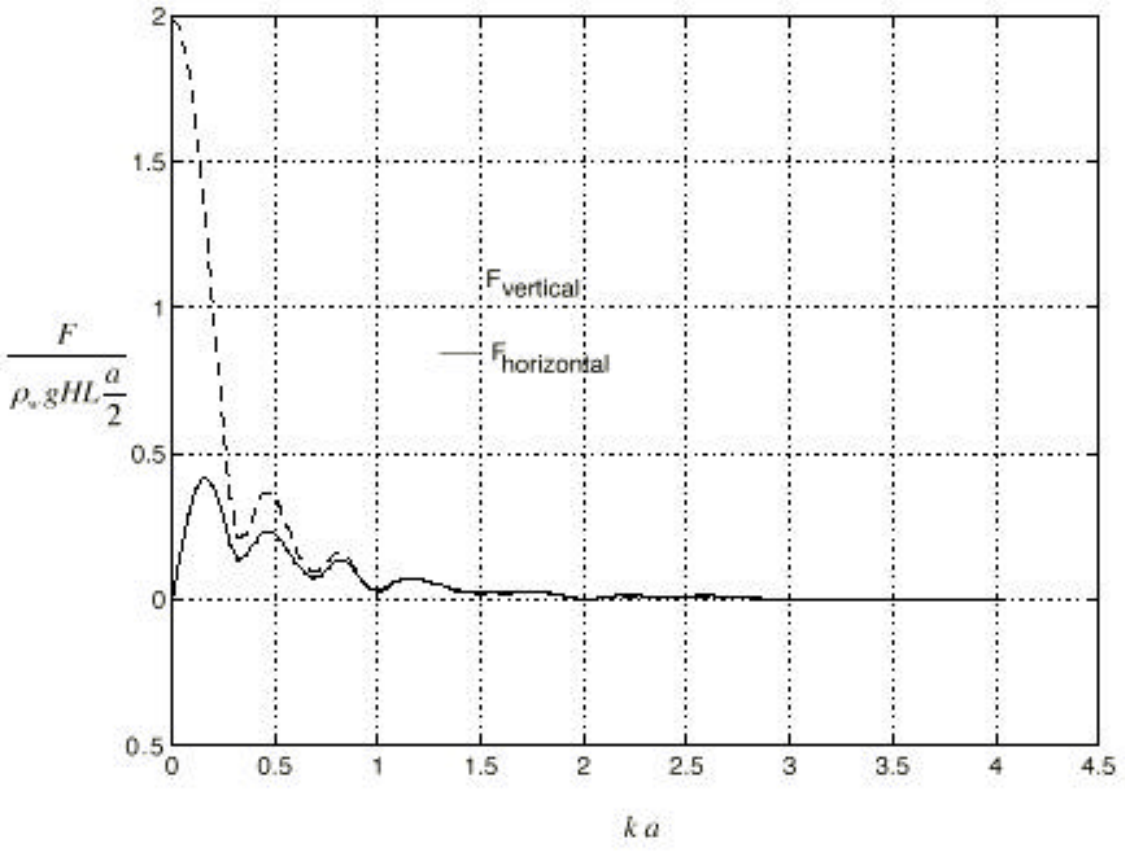

Figure 5.27 Vertical and horizontal forces for the case of oblique incident waves ($\beta = 30°$).

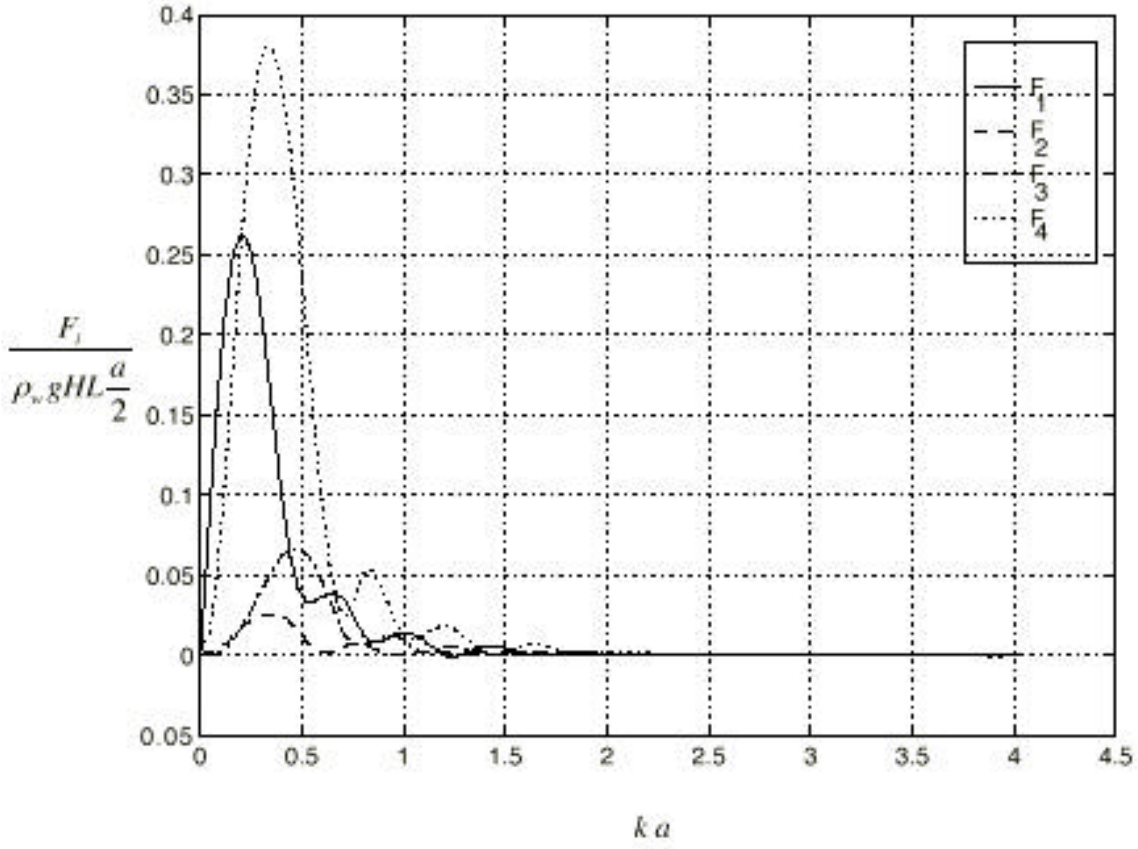

Figure 5.28 Hydrodynamic forces for modes 1, 2, 3 and 4 ($\beta = 30°$).

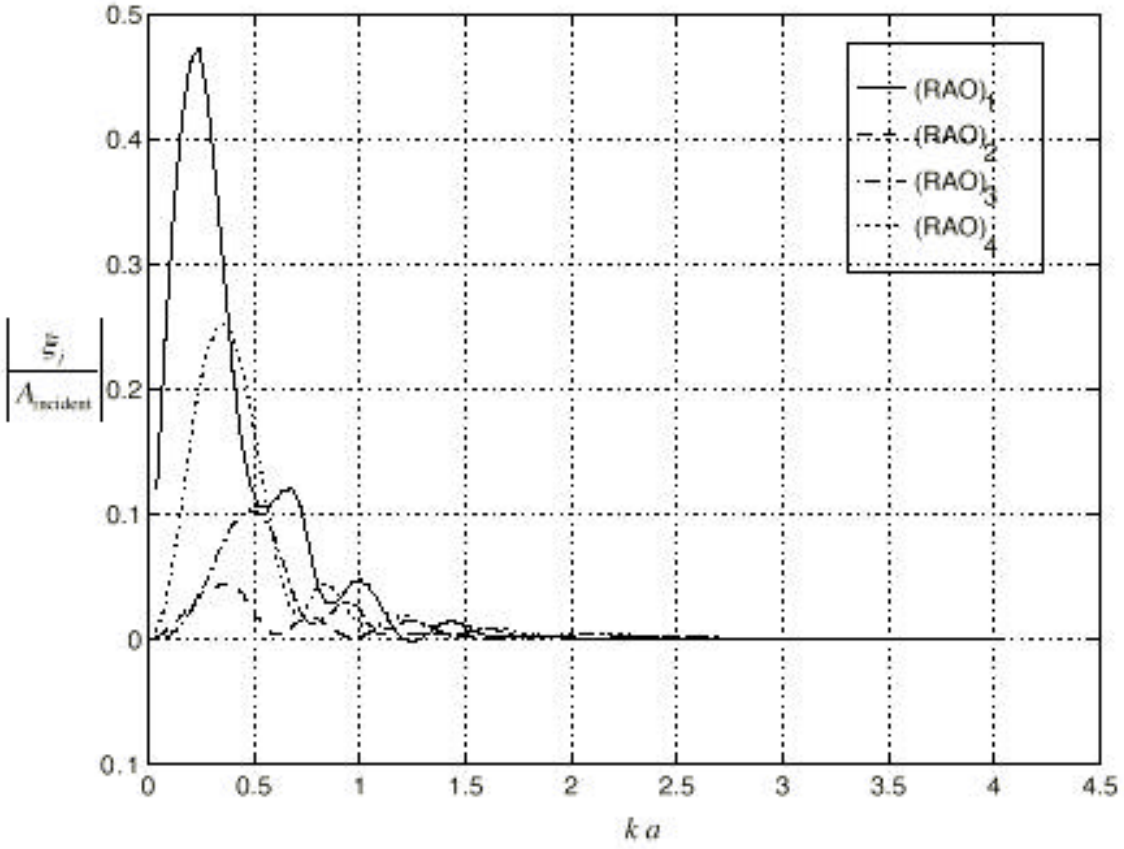

Figure 5.29 RAO for the case of oblique incident waves ($\beta = 30°$).

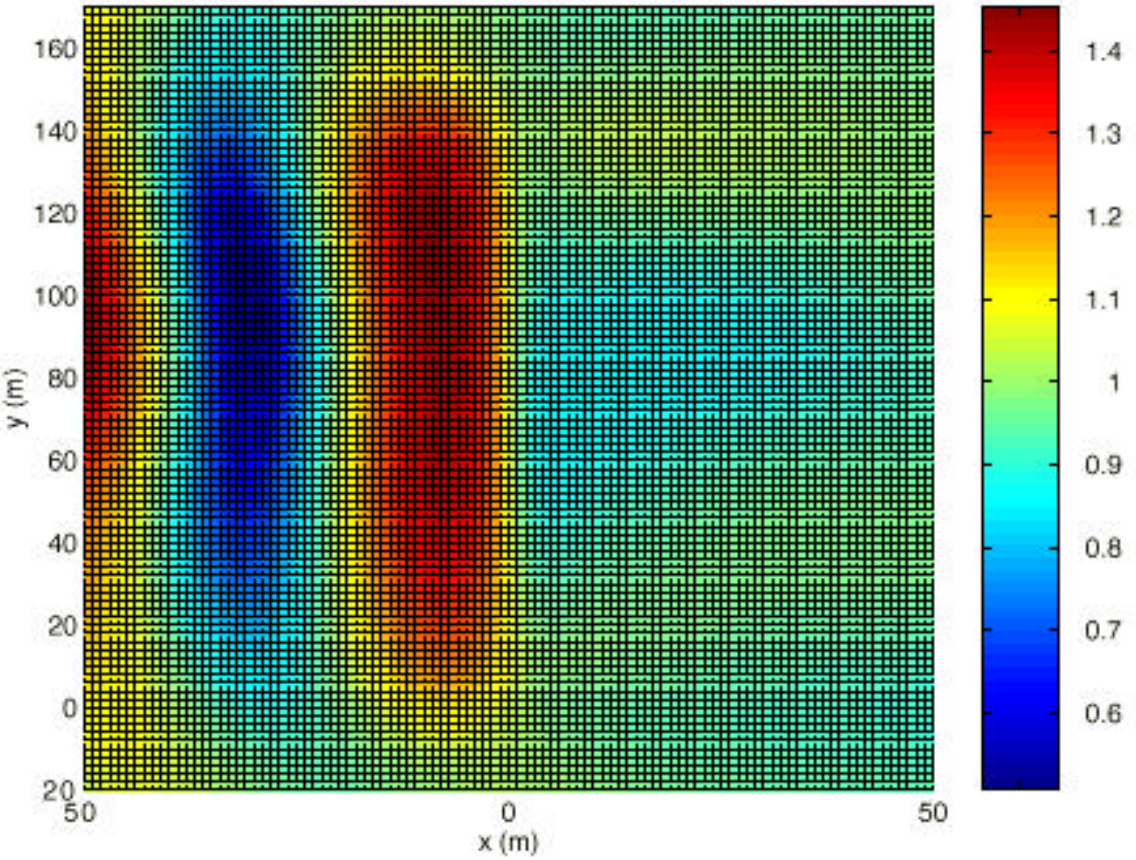

Figure 5.30 The amplitude of the free surface elevation for $\omega = \frac{\pi}{6}$ $\left(\beta = 15^{\circ}\right)$.

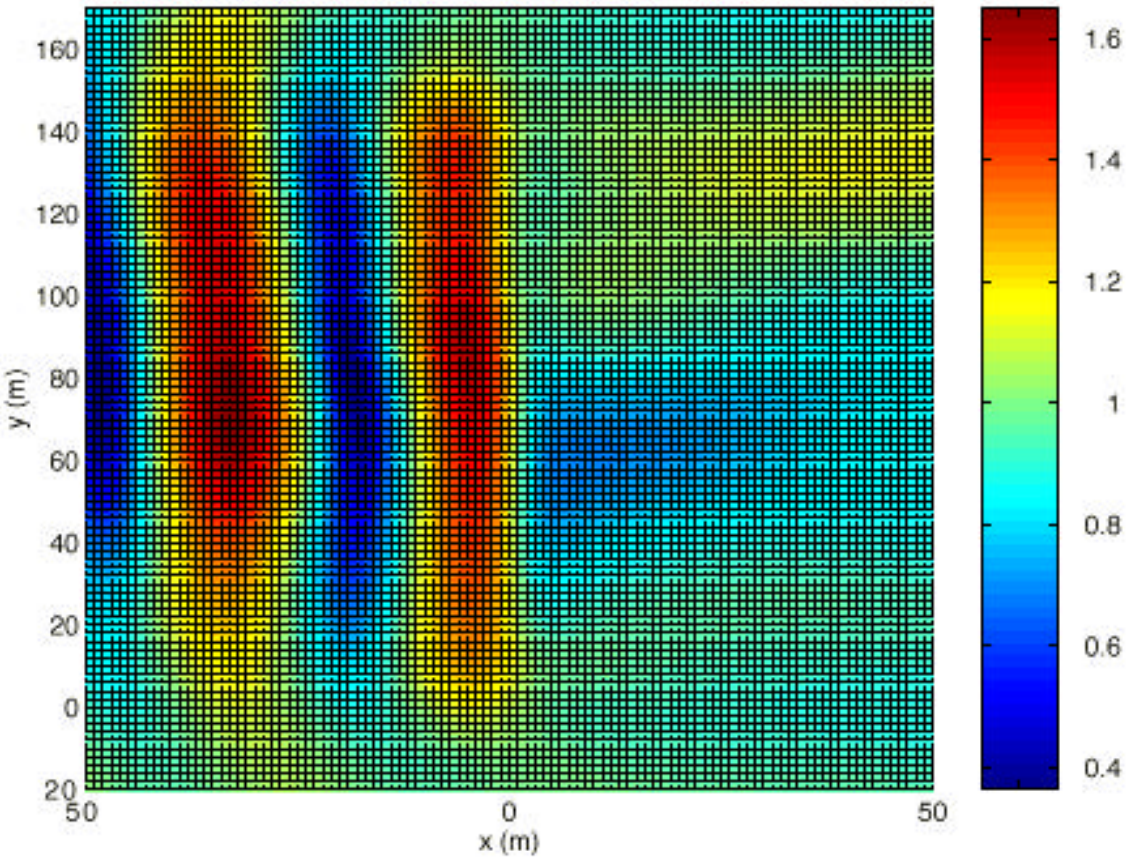

Figure 5.31 The amplitude of the free surface elevation for $\omega = \frac{\pi}{4}$ $(\beta = 15^{\circ})$.

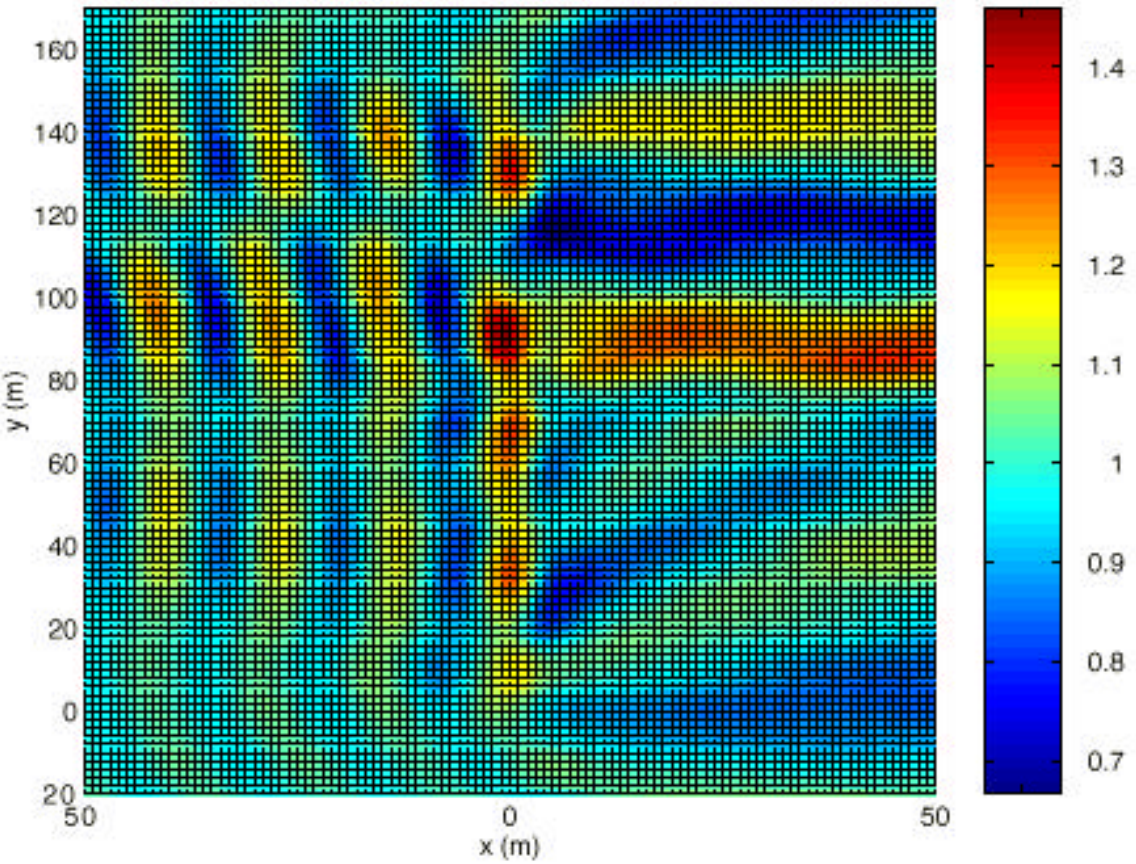

Figure 5.32 The amplitude of the free surface elevation for $\omega = \omega_{\kappa_{max}} \left(\beta = 15^{\circ} \right)$.

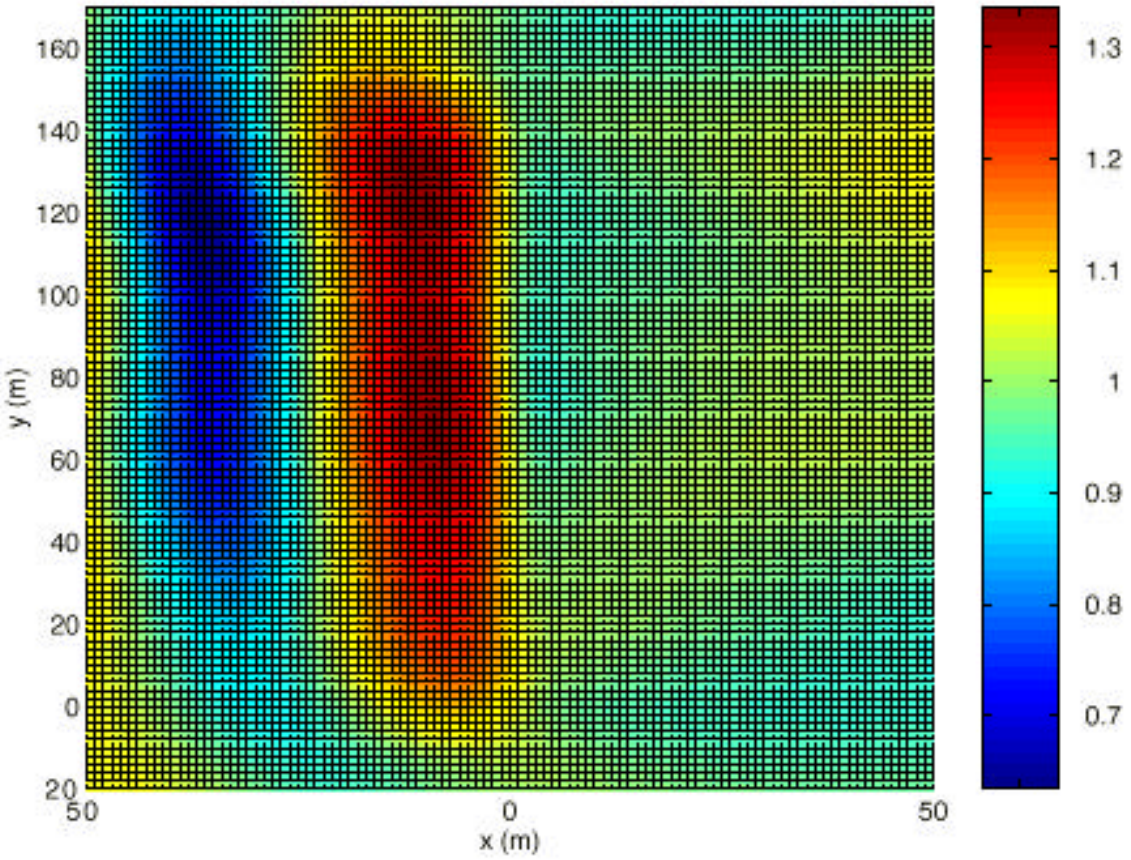

Figure 5.33 The amplitude of the free surface elevation for $\omega = \frac{\pi}{6}$ $(\beta = 30^{\circ})$.

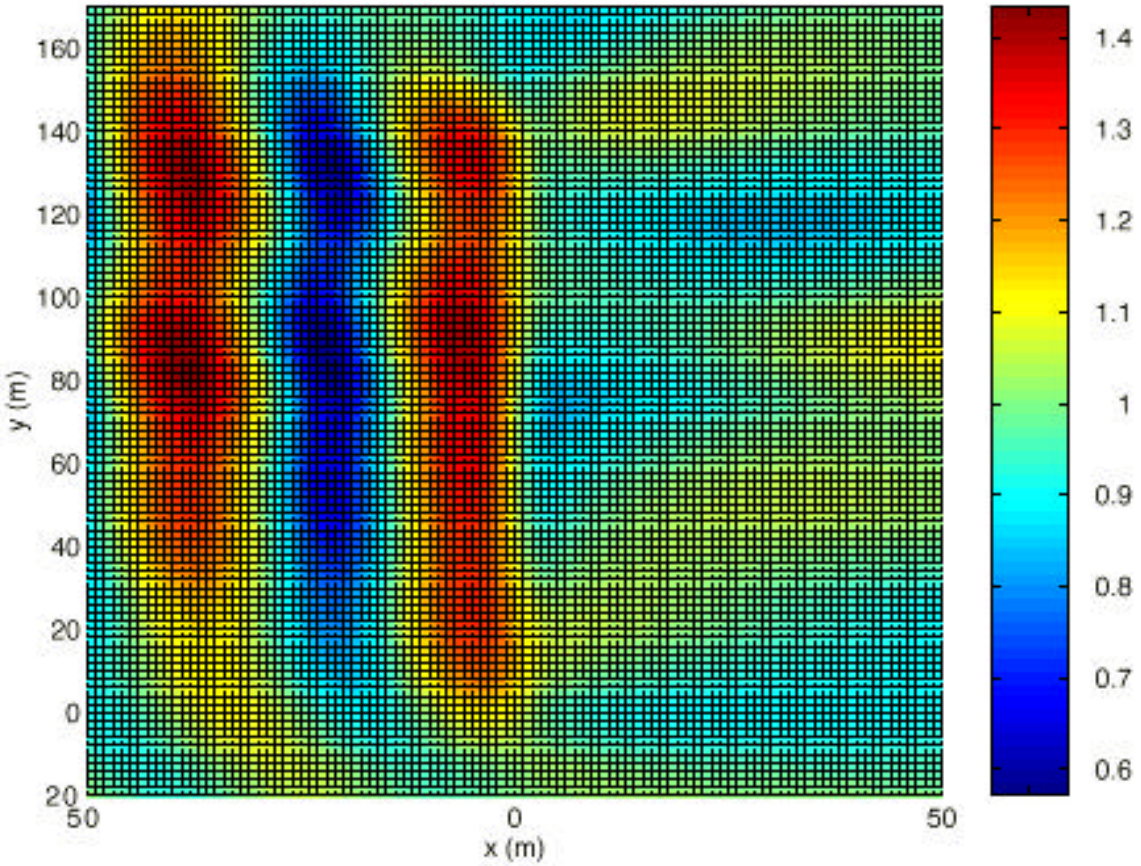

Figure 5.34 The amplitude of the free surface elevation for $\omega = \frac{\pi}{4}$ $(\beta = 30^{\circ})$.

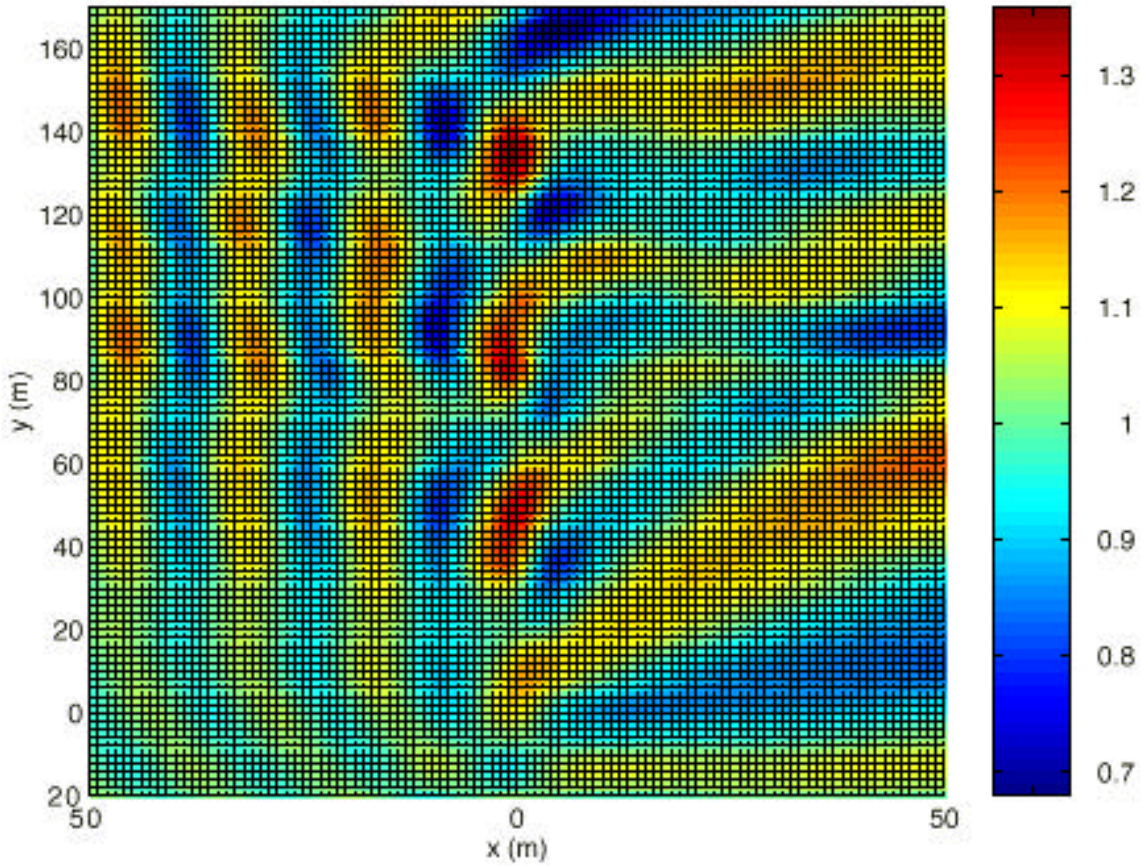

Figure 5.35 The amplitude of the free surface elevation for $\omega = \omega_{n\_}\left(\beta = 30^{\circ}\right)$.

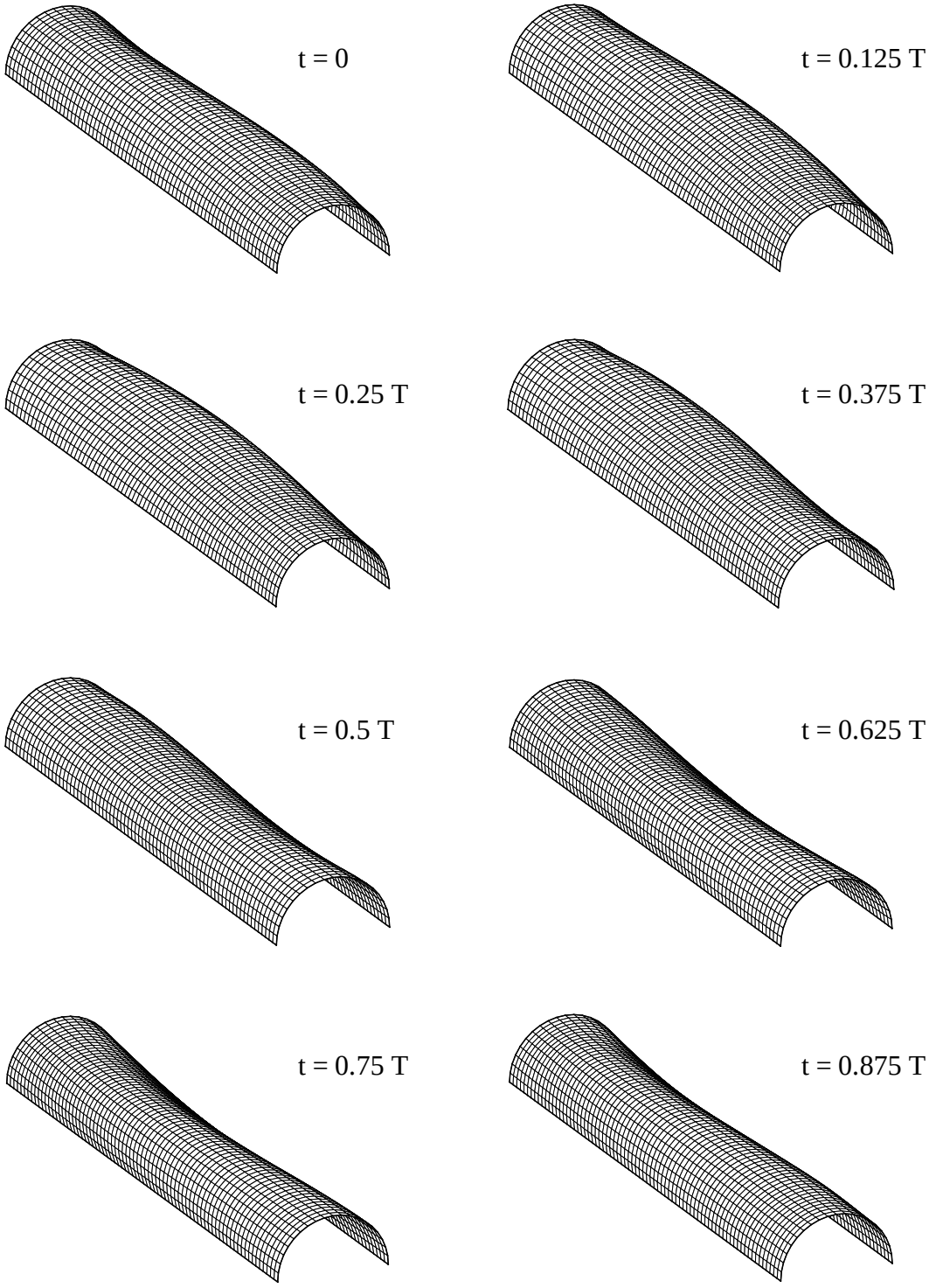

Figure 5.36 Displacements of structure over time for $A_{\text{incident}} = 1$ ($\omega = \frac{\pi}{4}$, $\beta = 15°$).

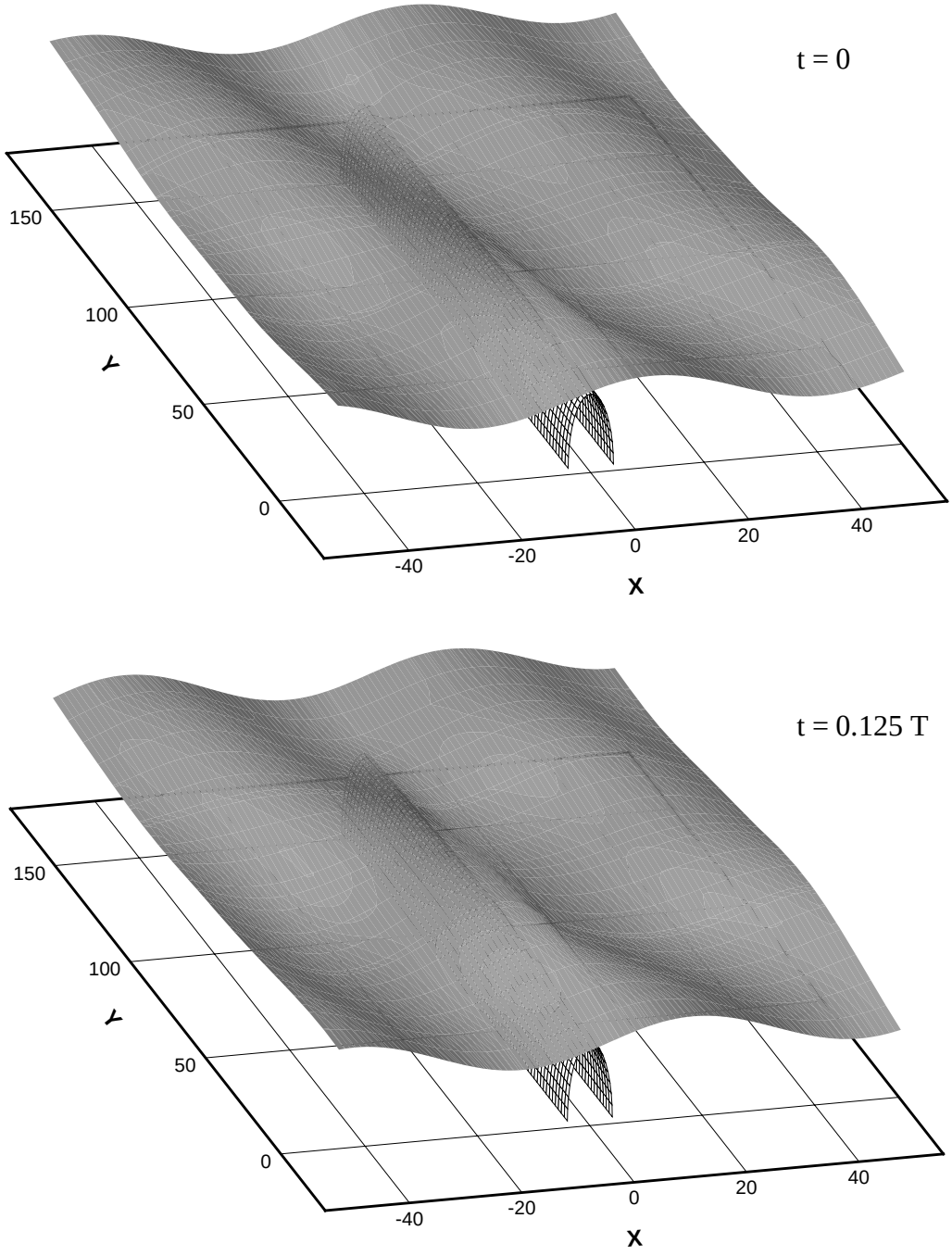

Figure 5.37.a Free surface elevation ($\omega = \frac{\pi}{4}$, $\beta = 15°$).

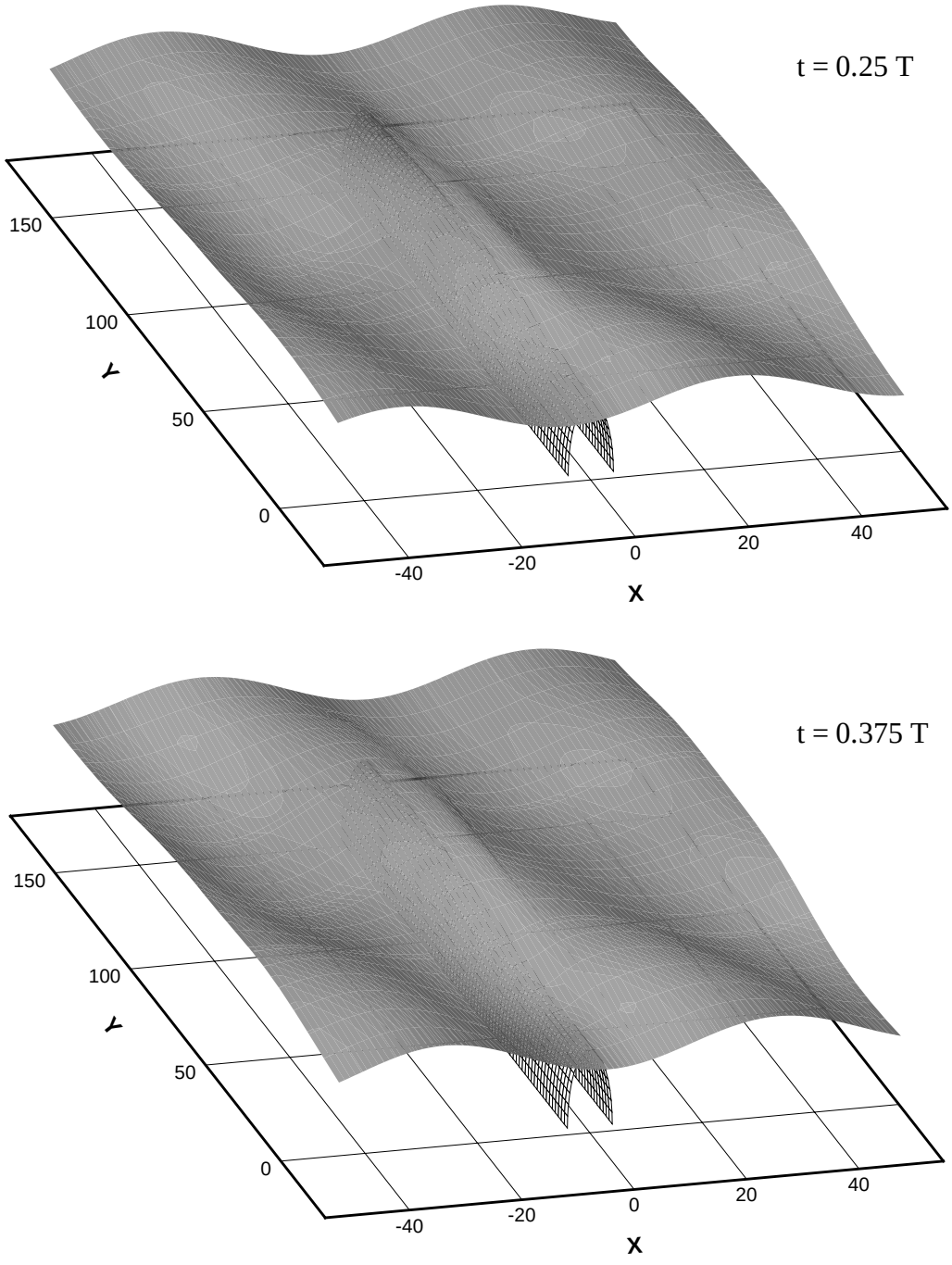

Figure 5.37.b Free surface elevation ($\omega = \frac{\pi}{4}$, $\beta = 15°$).

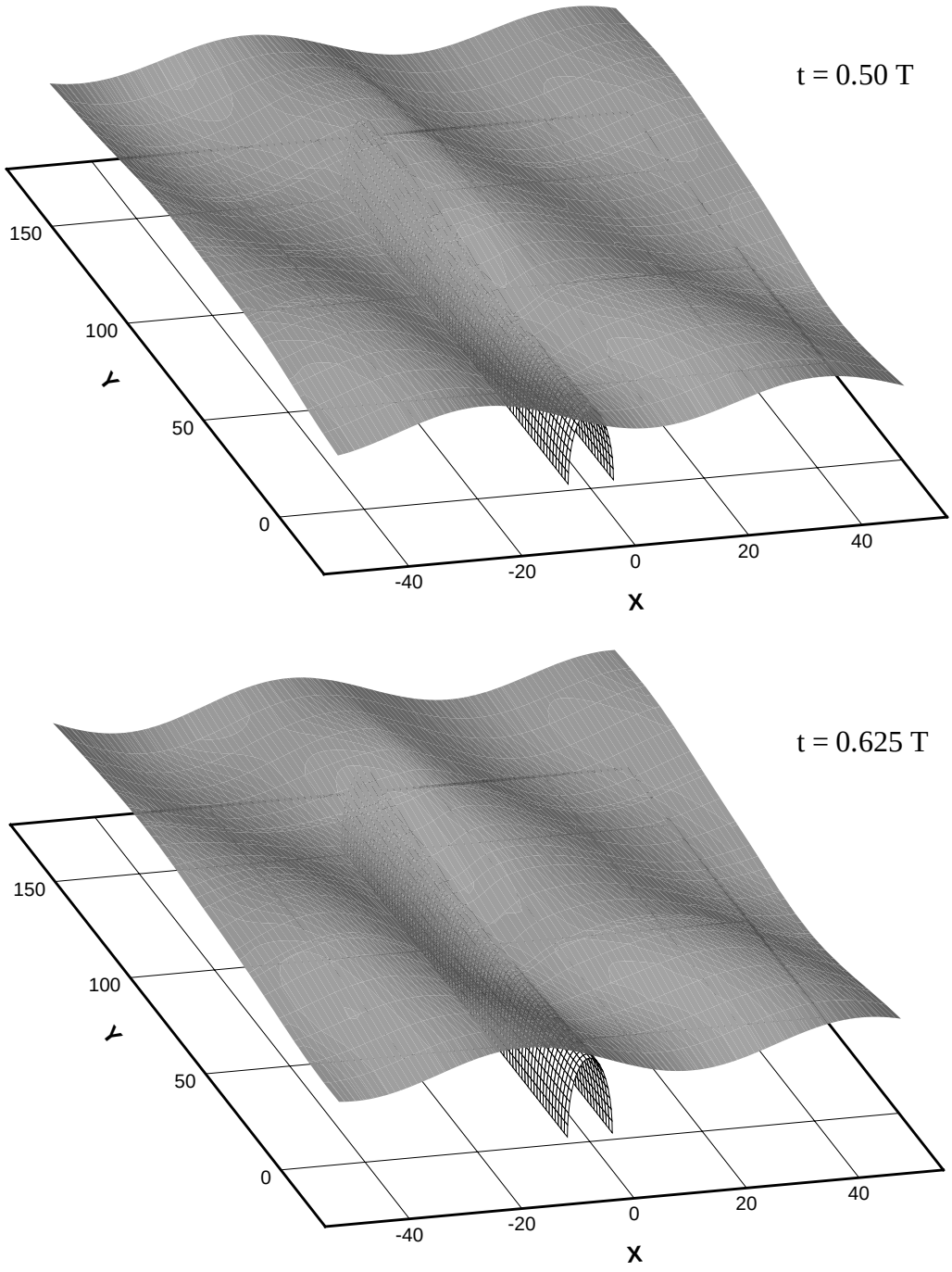

Figure 5.37.c Free surface elevation ($\omega = \frac{\pi}{4}$, $\beta = 15°$).

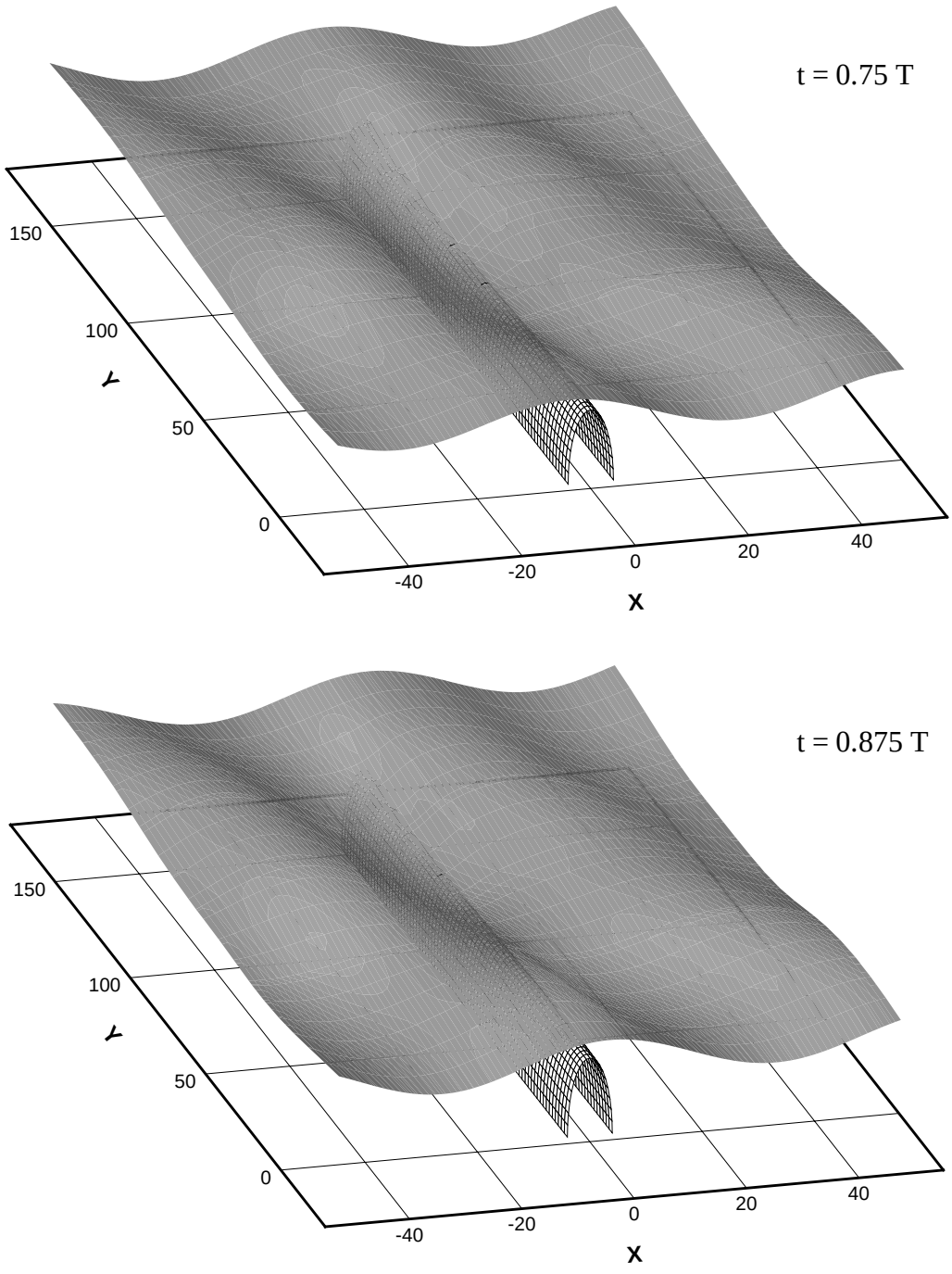

Figure 5.37.d Free surface elevation ($\omega = \frac{\pi}{4}$, $\beta = 15°$).

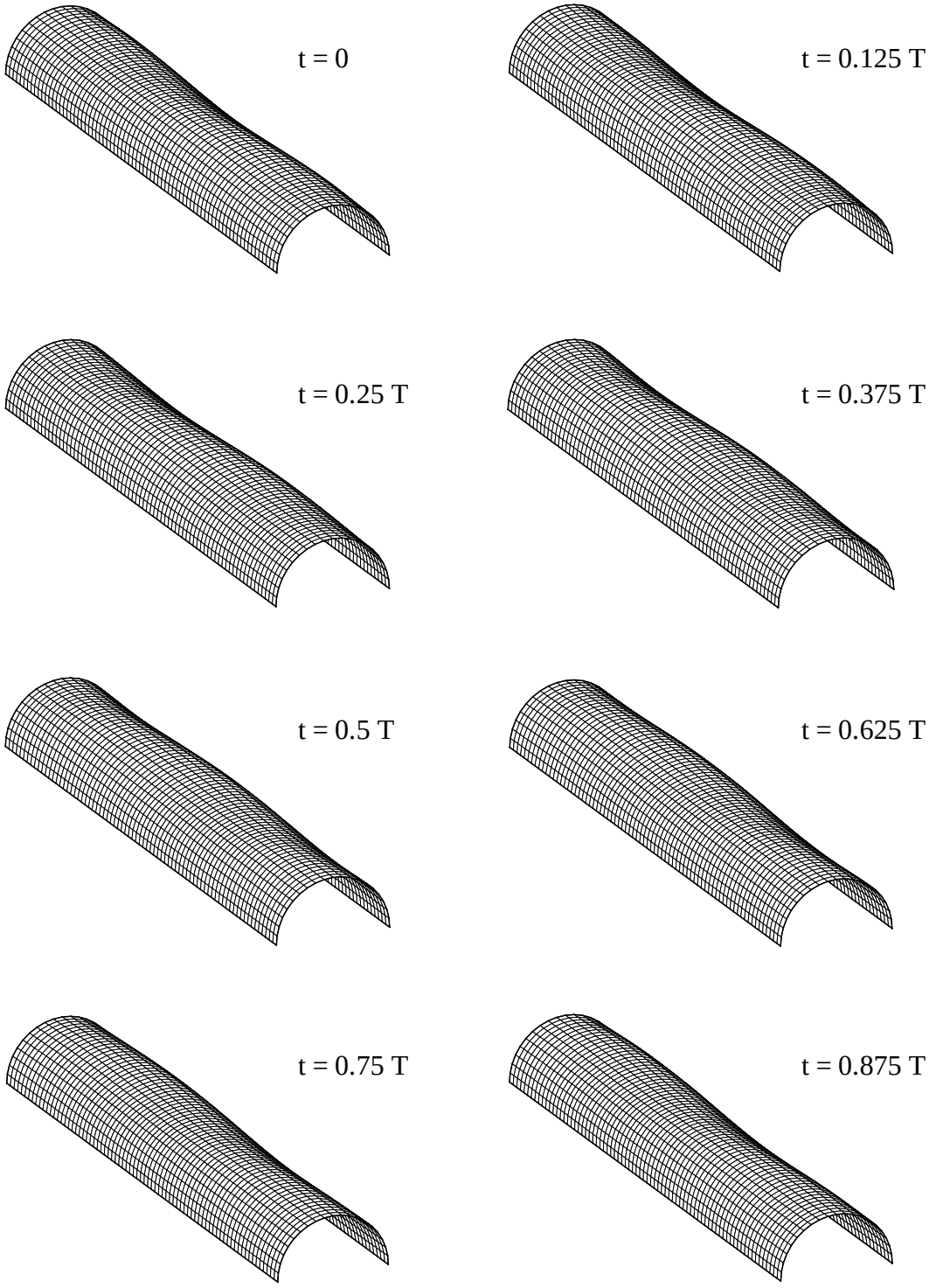

Figure 5.38 Displacements of structure over time for $A_{\text{incident}} = 1$ ($\omega = \frac{\pi}{4}$, $\beta = 30°$).

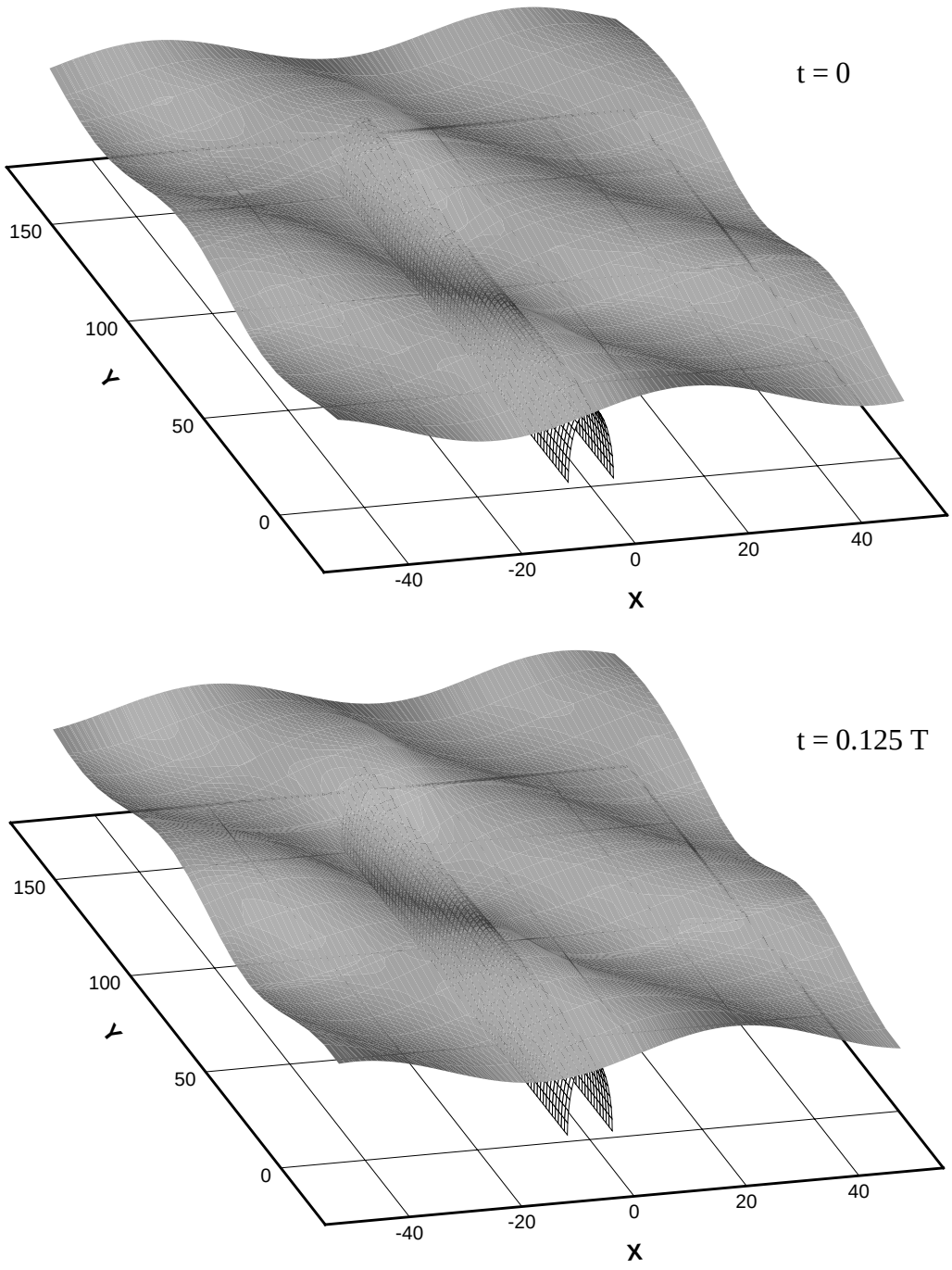

Figure 5.39.a Free surface elevation ($\omega = \frac{\pi}{4}$, $\beta = 30°$).

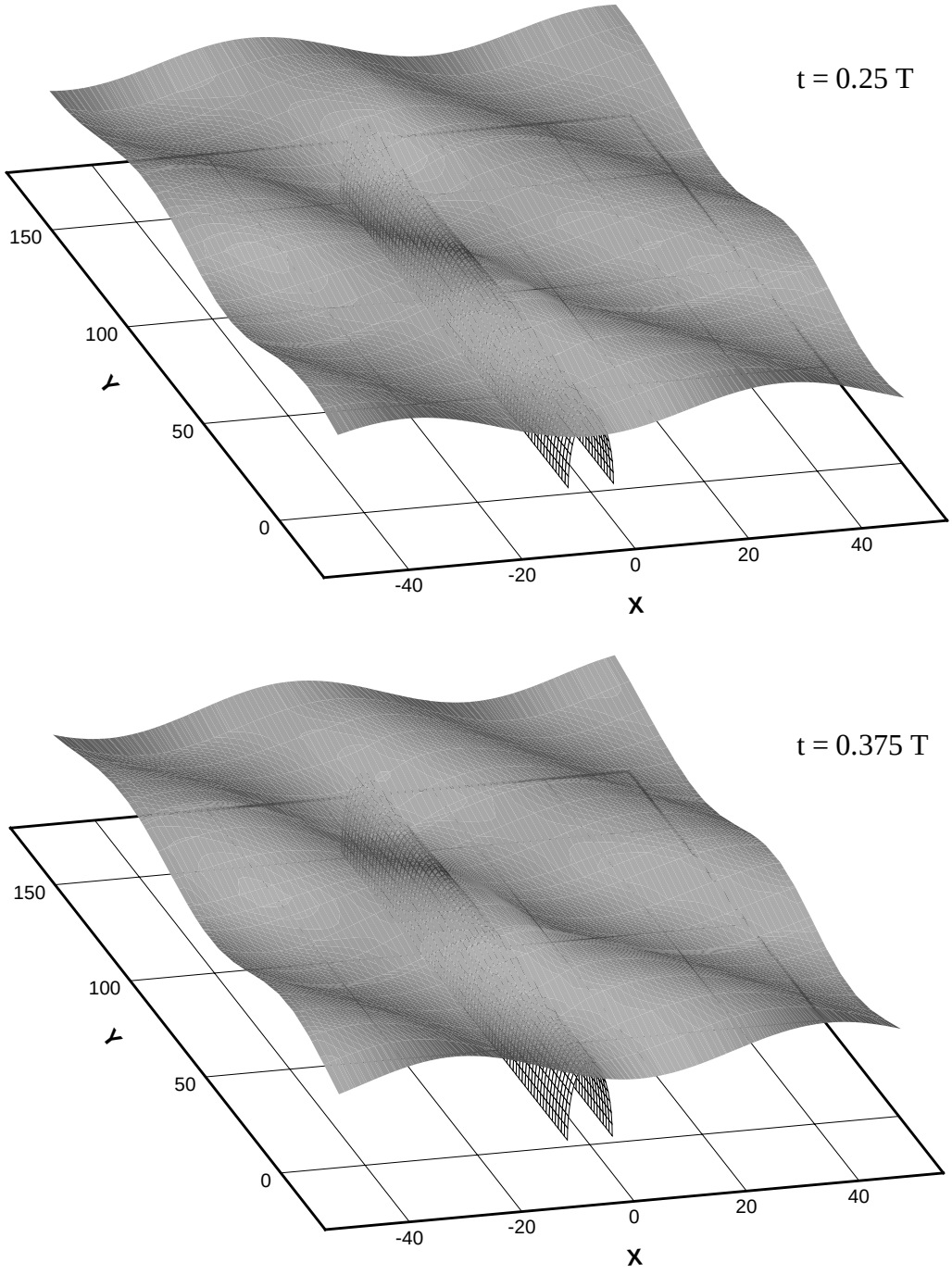

Figure 5.39.b Free surface elevation ($\omega = \frac{\pi}{4}$, $\beta = 30°$).

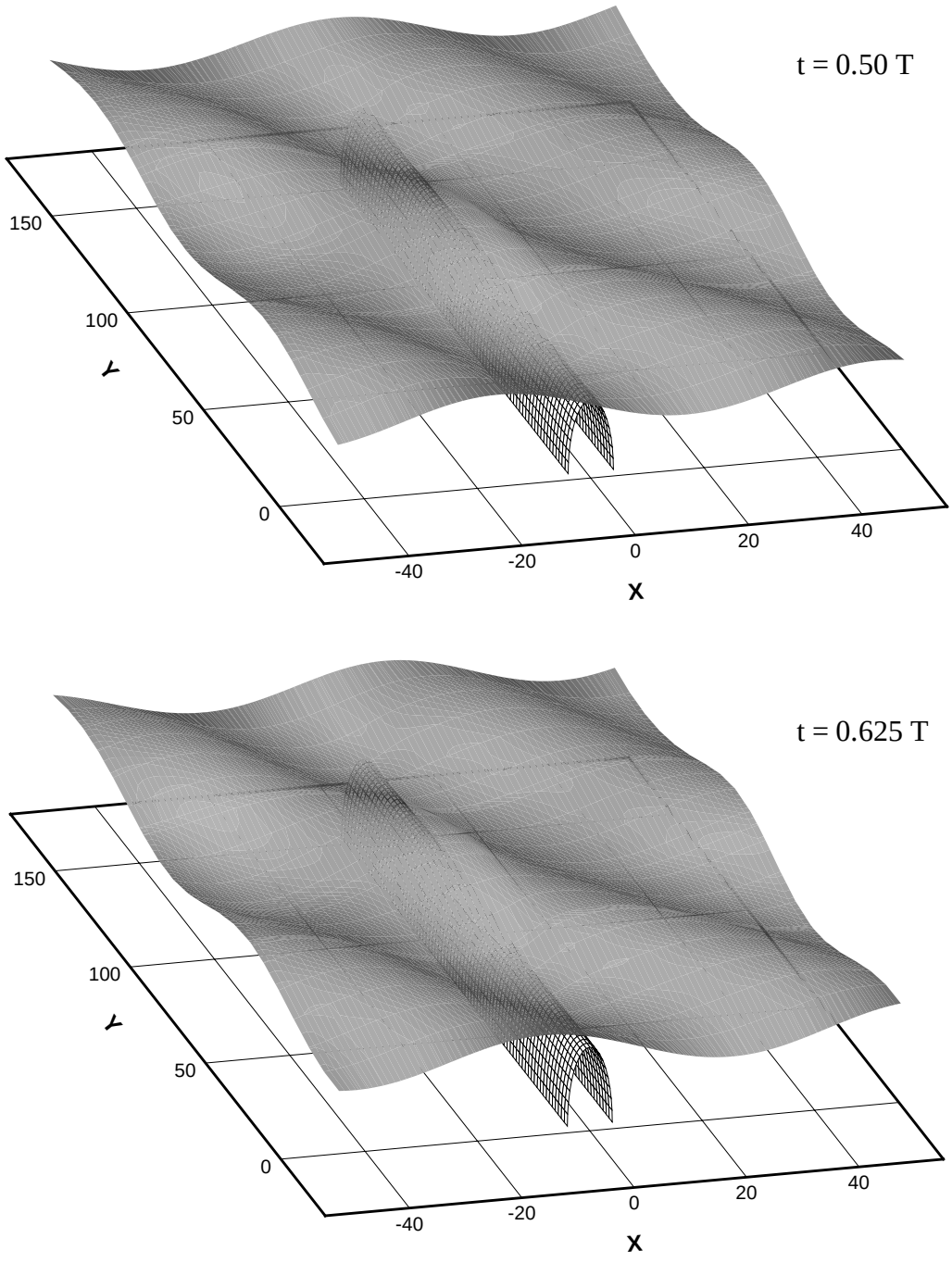

Figure 5.39.c Free surface elevation ($\omega = \frac{\pi}{4}$, $\beta = 30°$).

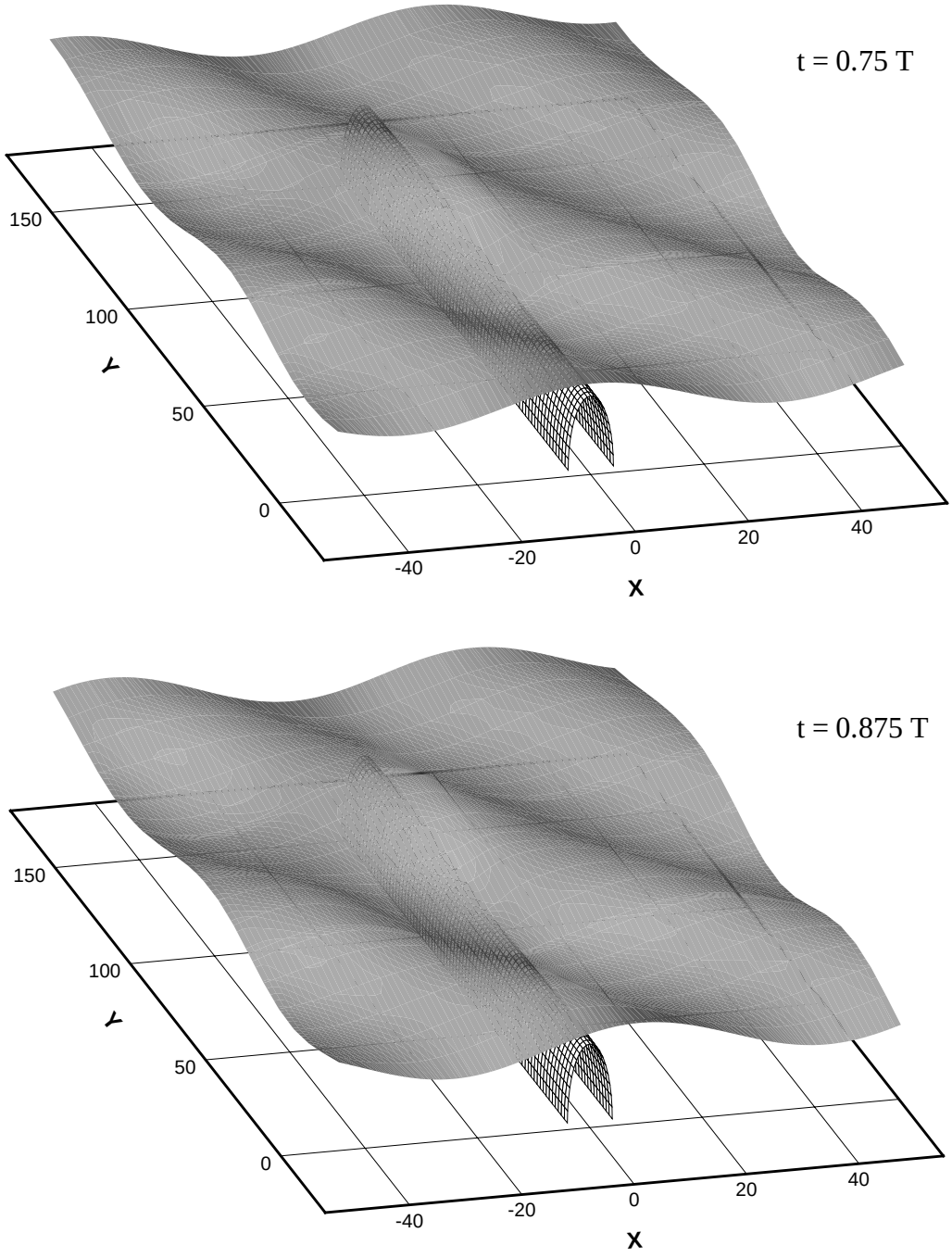

Figure 5.39.d Free surface elevation ($\omega = \frac{\pi}{4}$, $\beta = 30°$).

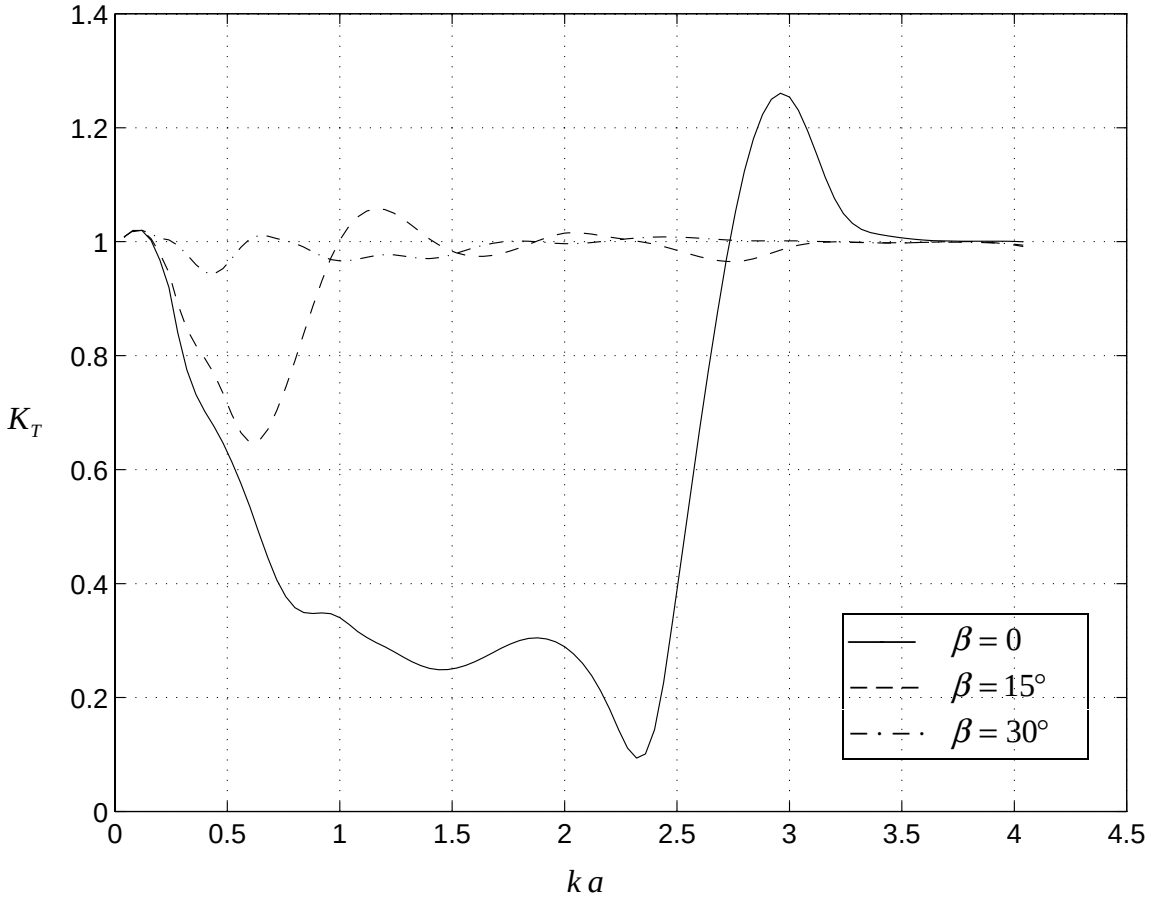

Figure 5.40 Transmission coefficients.

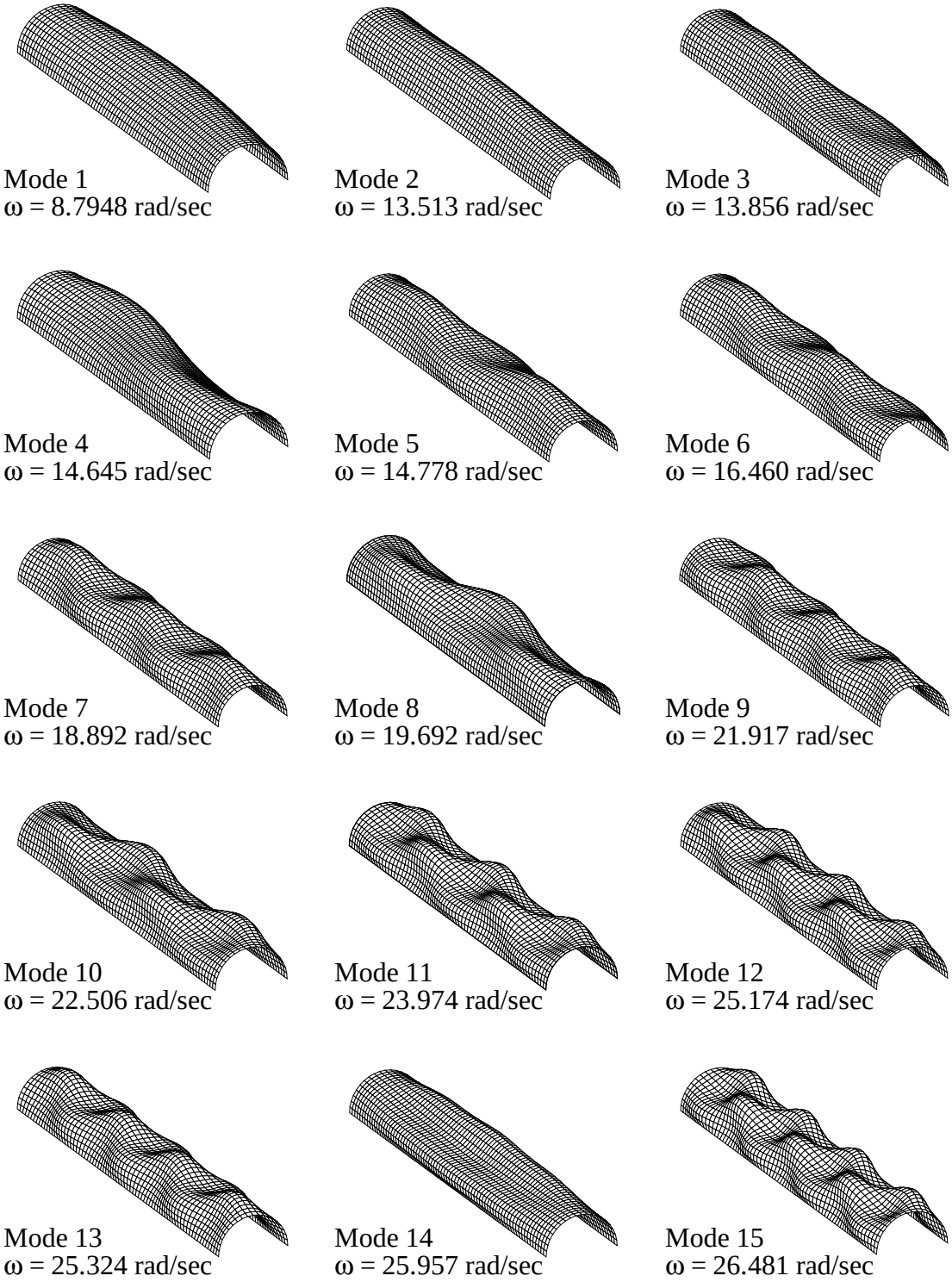

Figure 5.41 Natural “dry” mode shapes and frequencies (water depth = 5 m).

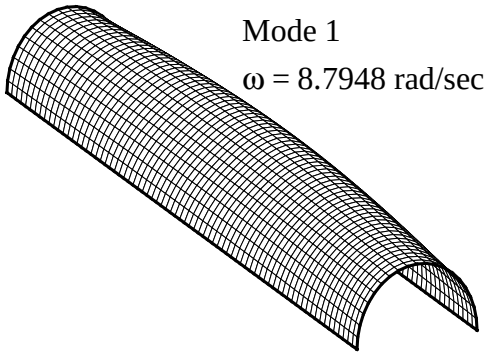

Mode 1
ω = 8.7948 rad/sec

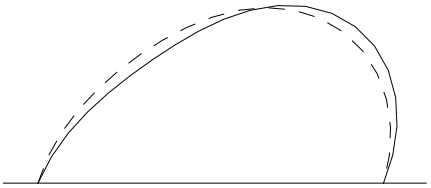

Cross sections at:
L/2 —
L/4 – –

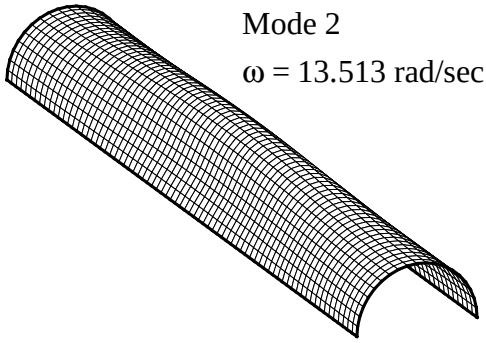

Mode 2
ω = 13.513 rad/sec

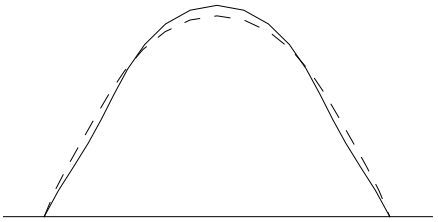

Cross sections at:
L/2 —
L/4 – –

Figure 5.42.a Natural “dry” mode shapes 1-2.

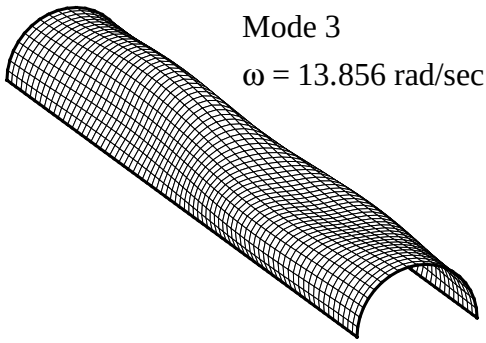

Mode 3
ω = 13.856 rad/sec

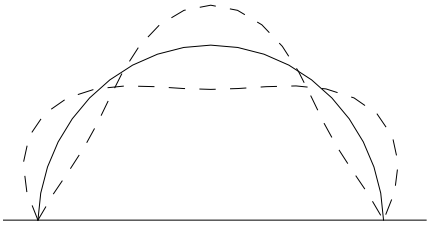

Cross sections at:
L/2 —
L/4 – –

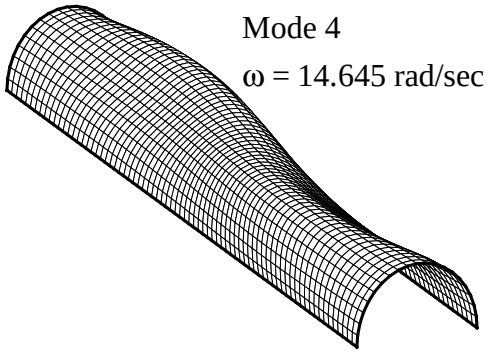

Mode 4
ω = 14.645 rad/sec

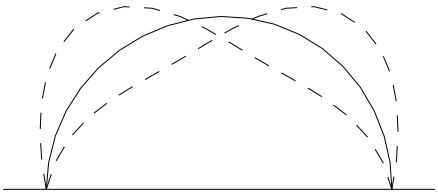

Cross sections at:
L/2 —
L/4 – –

Figure 5.42.b Natural “dry” mode shapes 3-4.

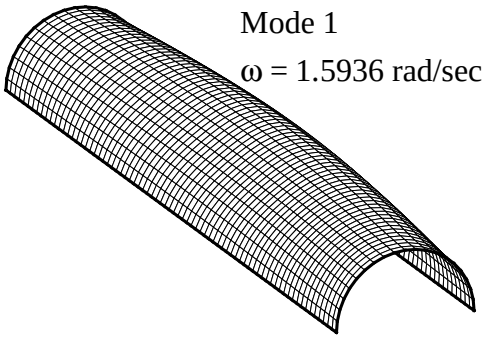

Mode 1
ω = 1.5936 rad/sec

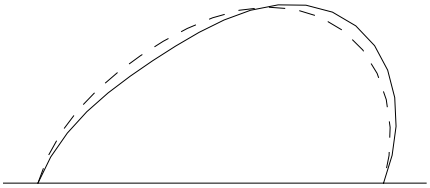

Cross sections at:
L/2 —
L/4 – –

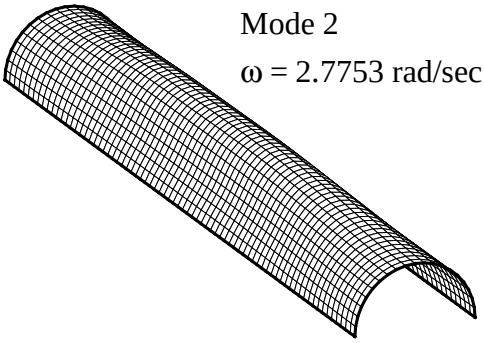

Mode 2
ω = 2.7753 rad/sec

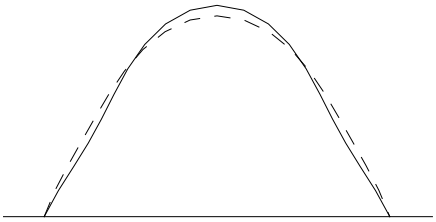

Cross sections at:
L/2 —
L/4 – –

Figure 5.43.a Natural “wet” mode shapes 1-2.

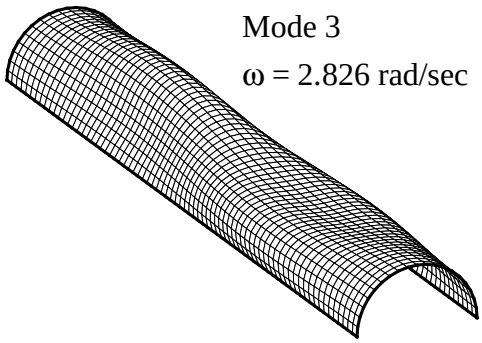

Mode 3
ω = 2.826 rad/sec

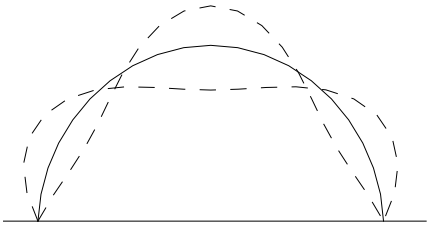

Cross sections at:
L/2 —
L/4 – –

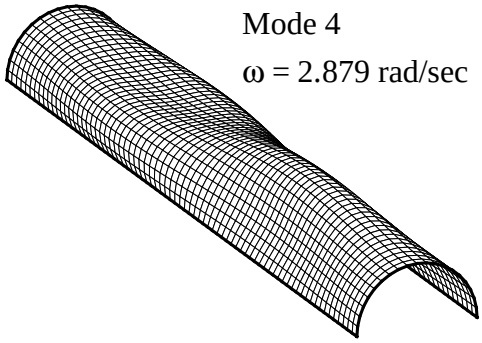

Mode 4
ω = 2.879 rad/sec

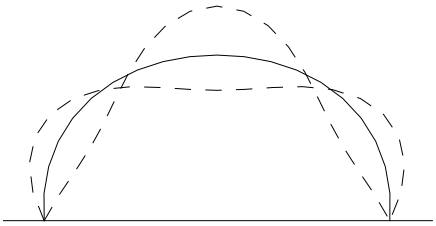

Cross sections at:
L/2 —
L/4 – –

Figure 5.43.b Natural “wet” mode shapes 3-4.

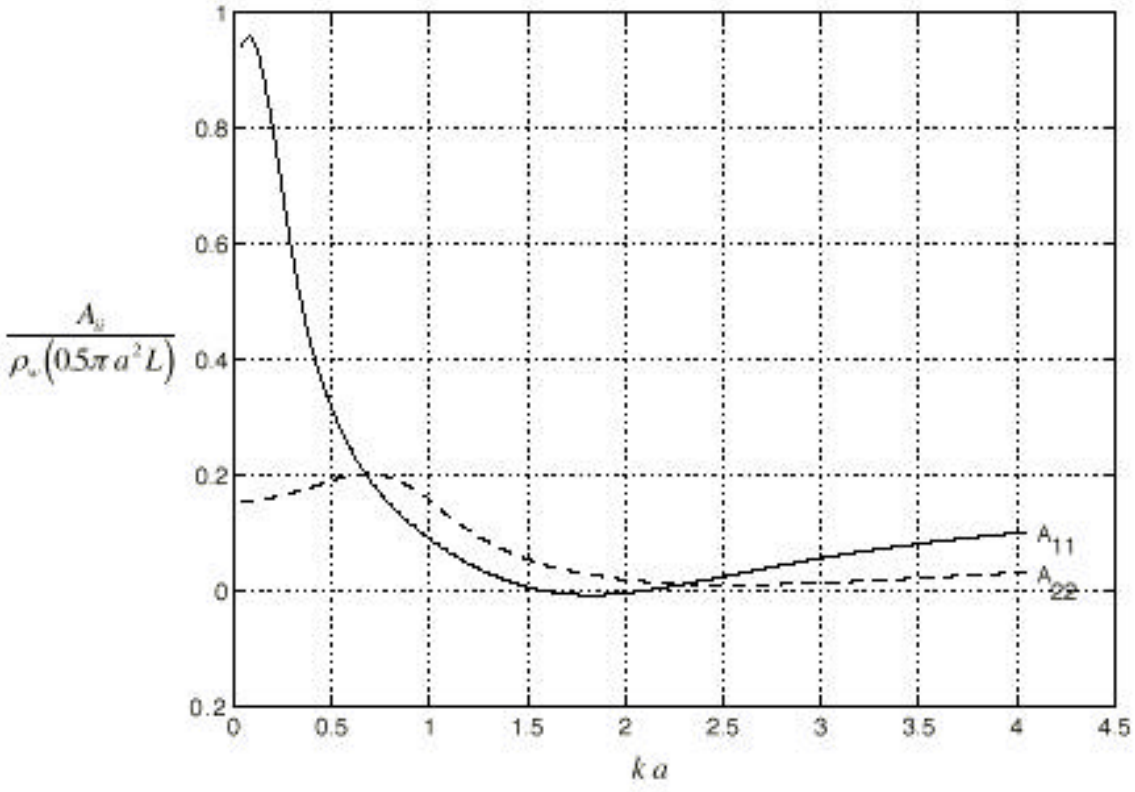

Figure 5.44 Non-dimensional added mass coefficients.

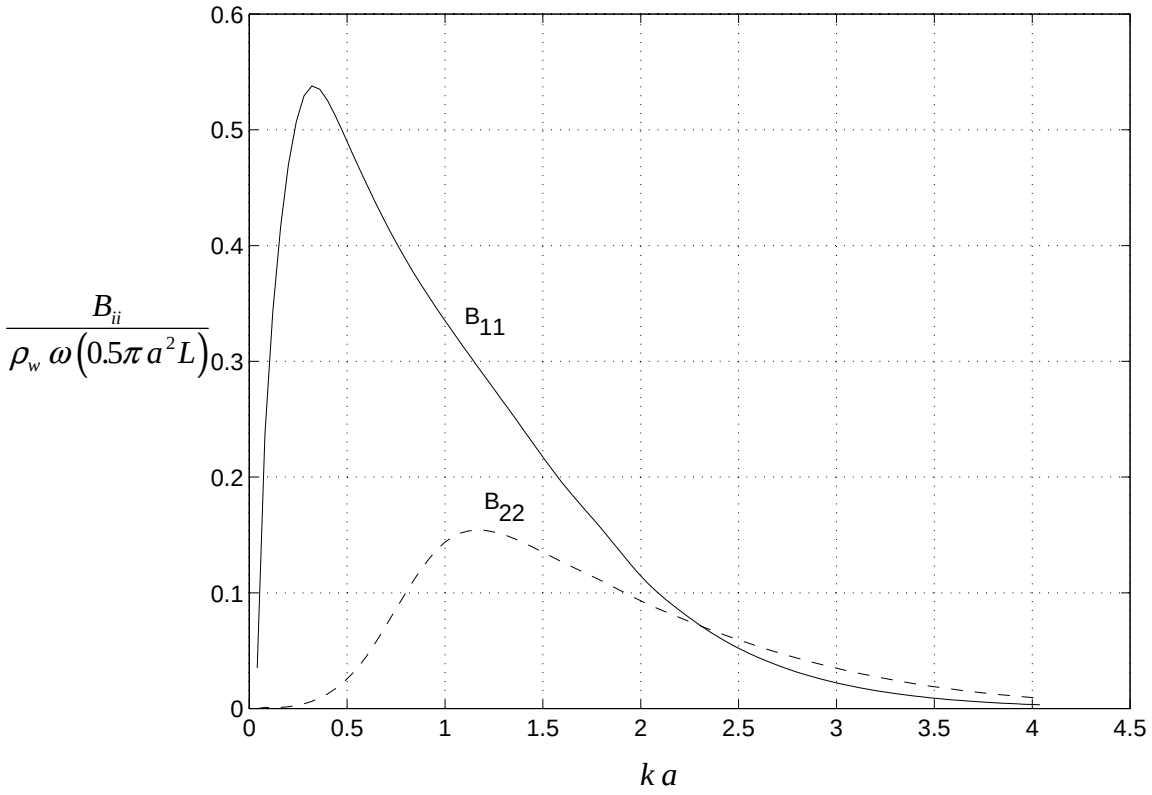

Figure 5.45 Non-dimensional damping coefficients.

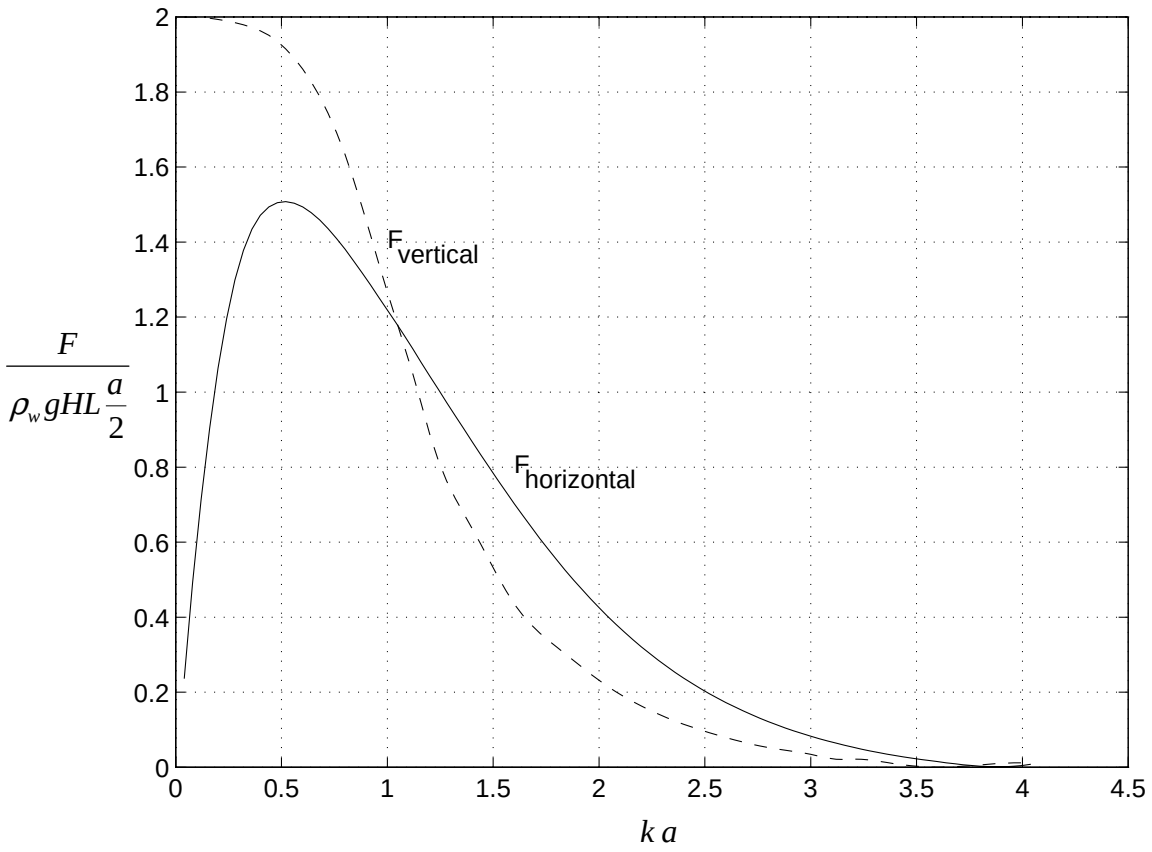

Figure 5.46 Hydrodynamic forces for the case of normal incident waves, $\beta = 0$.

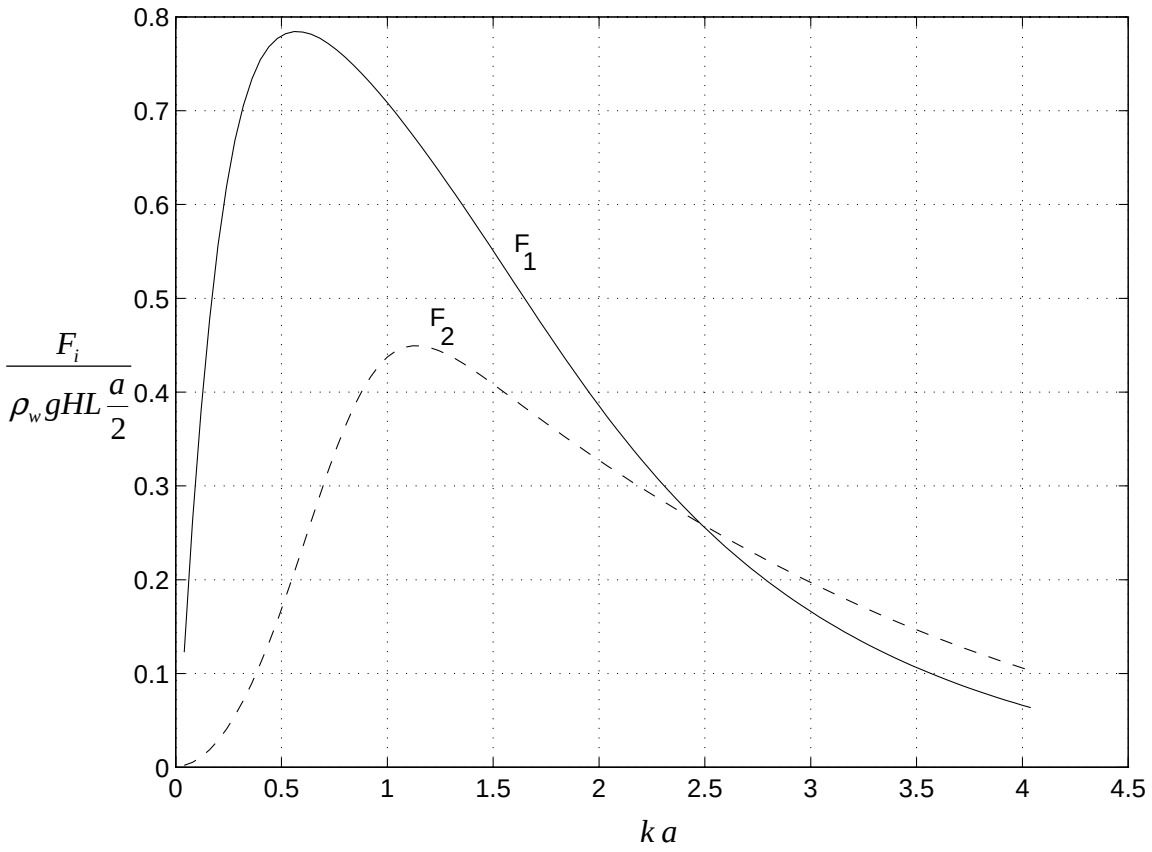

Figure 5.47 Hydrodynamic forces for modes 1 and 2 ($\beta = 0$).

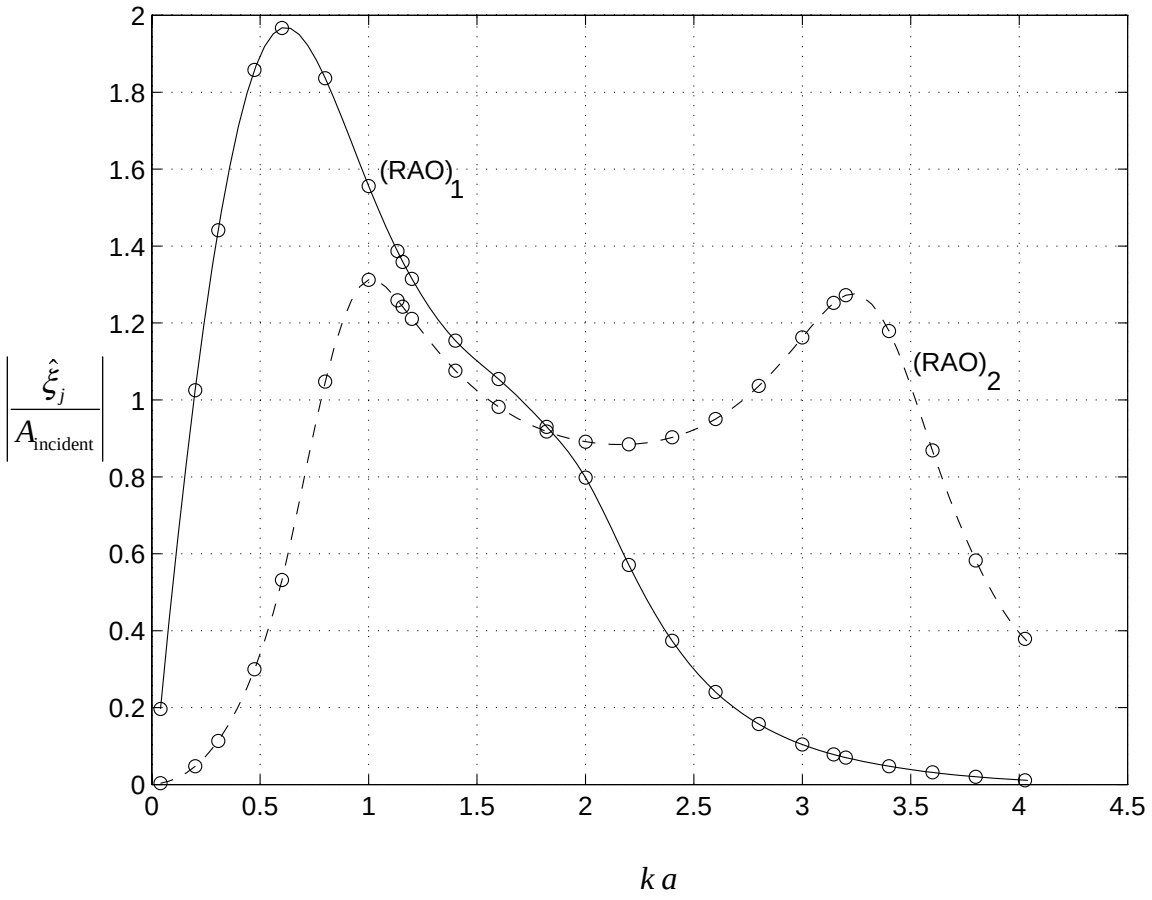

Figure 5.48 RAO for the case of normal incident waves ($\beta = 0$).

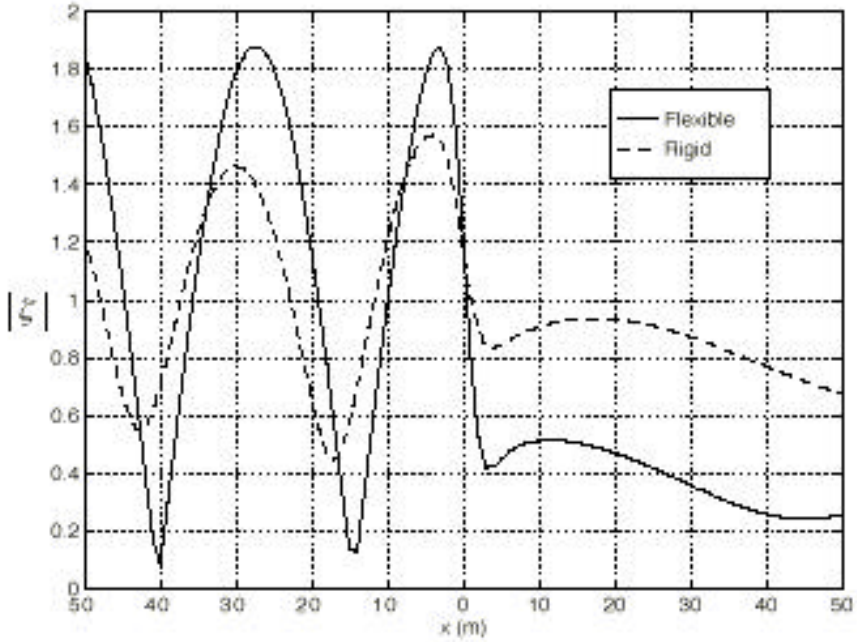

Figure 5.49.a Wave amplitude at the middle of the structure, $\omega = \frac{\pi}{4}$ rad/sec.

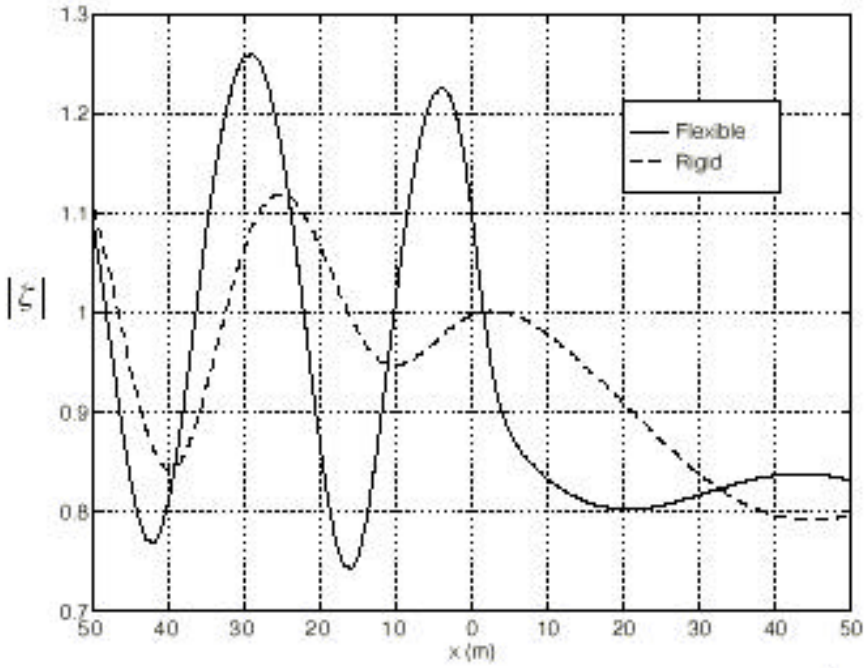

Figure 5.49.b Wave amplitude at the ends of the structure, $\omega = \frac{\pi}{4}$ rad/sec.

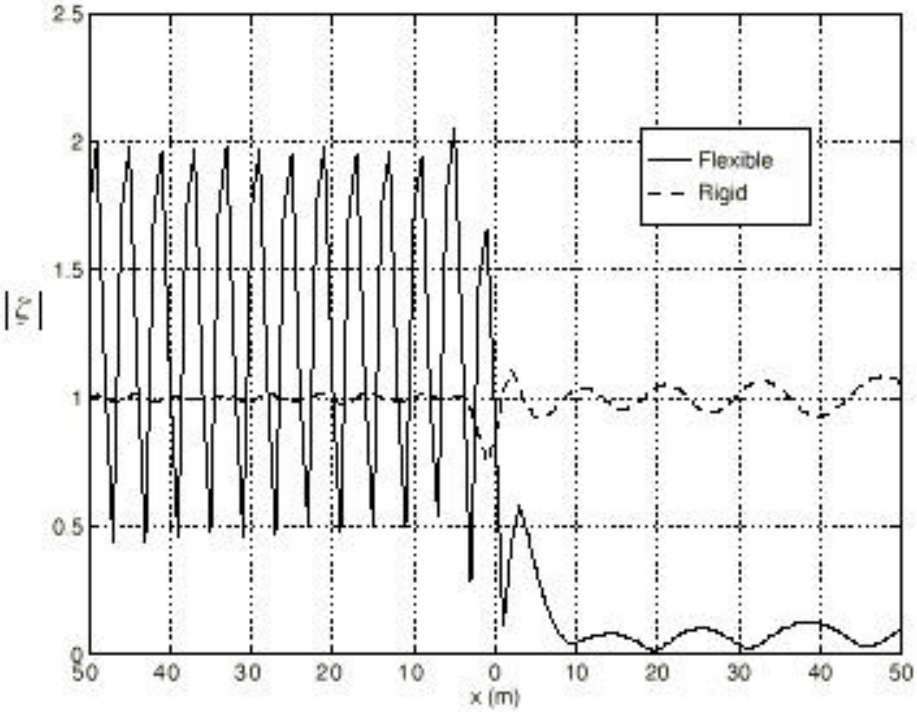

Figure 5.50.a Wave amplitude at the middle of the structure, $\omega = \omega_{n_{--}}$

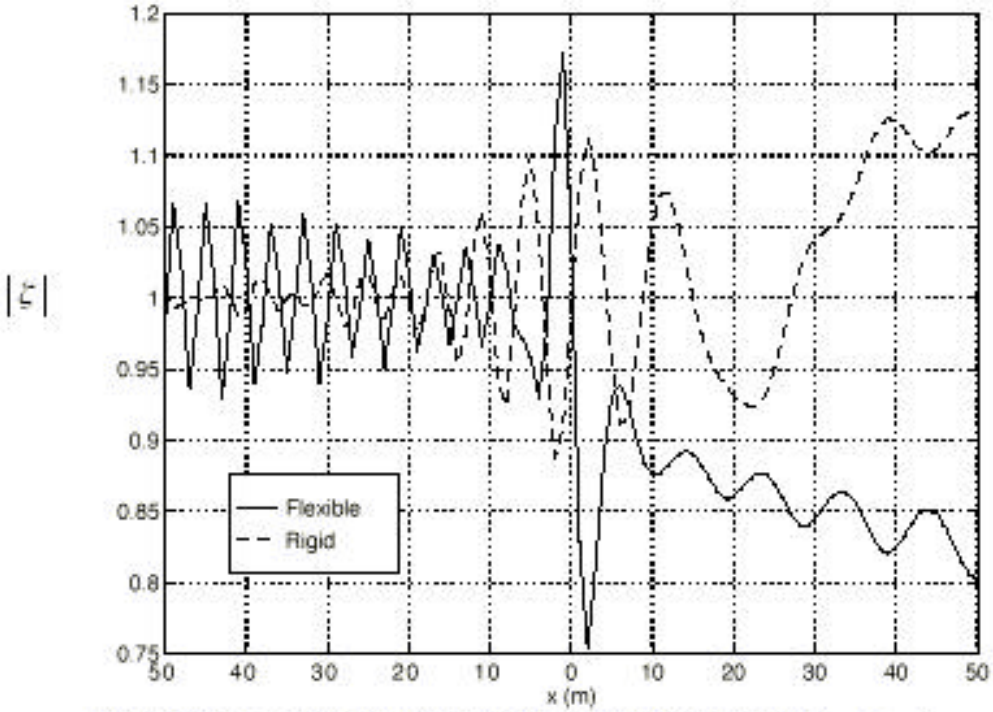

Figure 5.50.b Wave amplitude at the ends of the structure, $\omega = \omega_{n_{--}}$

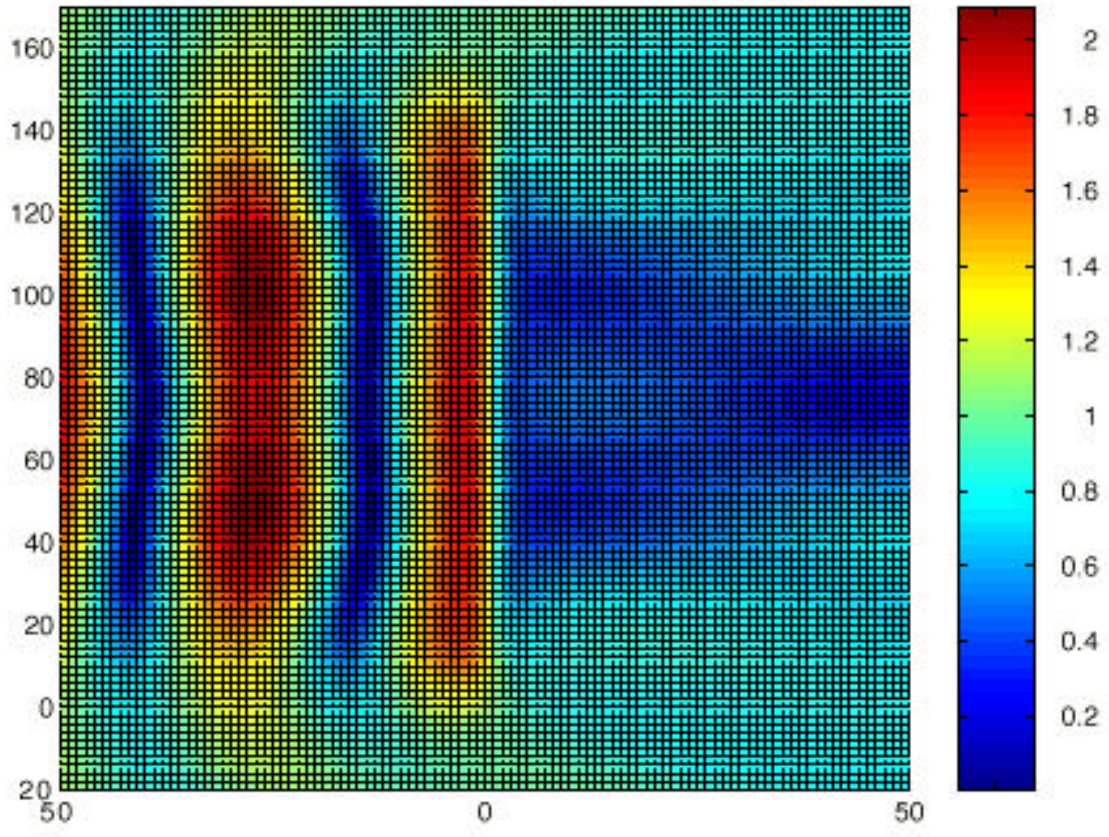

Figure 5.51 The amplitude of the free surface elevation for $\omega = \frac{\pi}{4}$ $(\beta = 0)$.

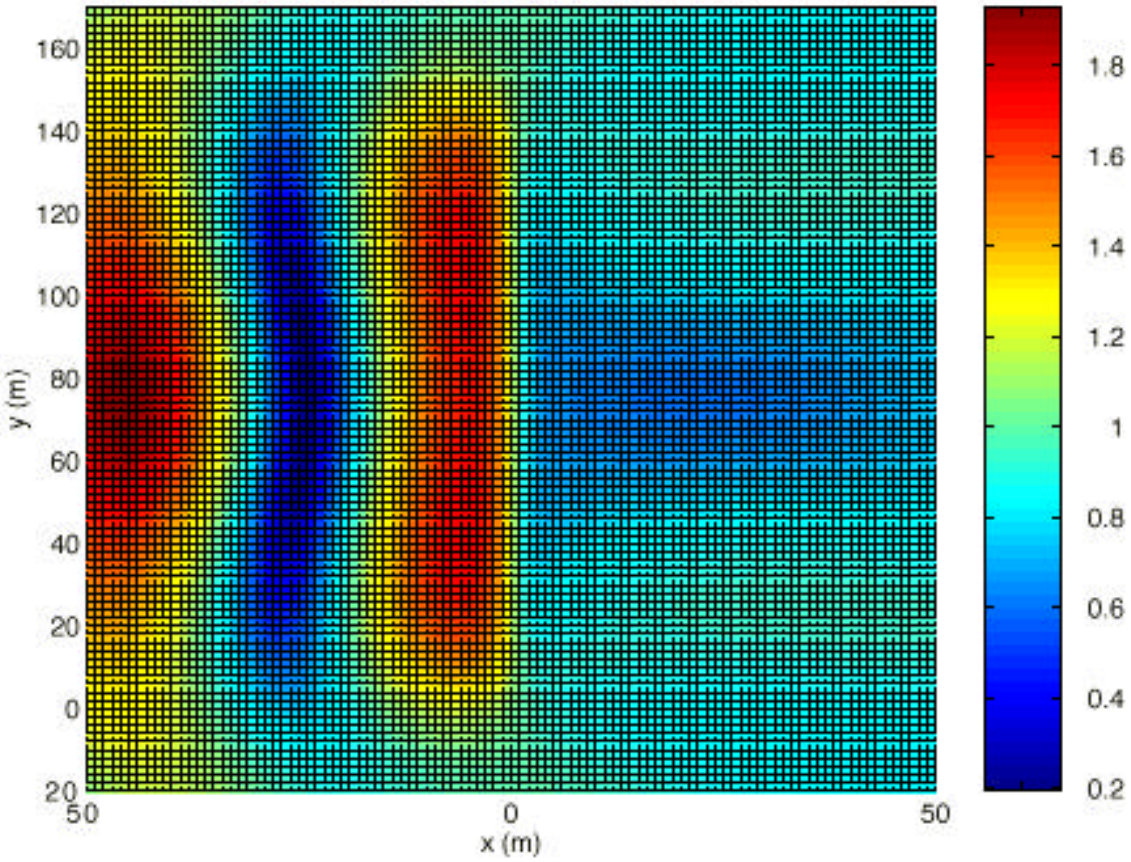

Figure 5.52 The amplitude of the free surface elevation for $\omega = \frac{\pi}{6}$ $(\beta = 0)$.

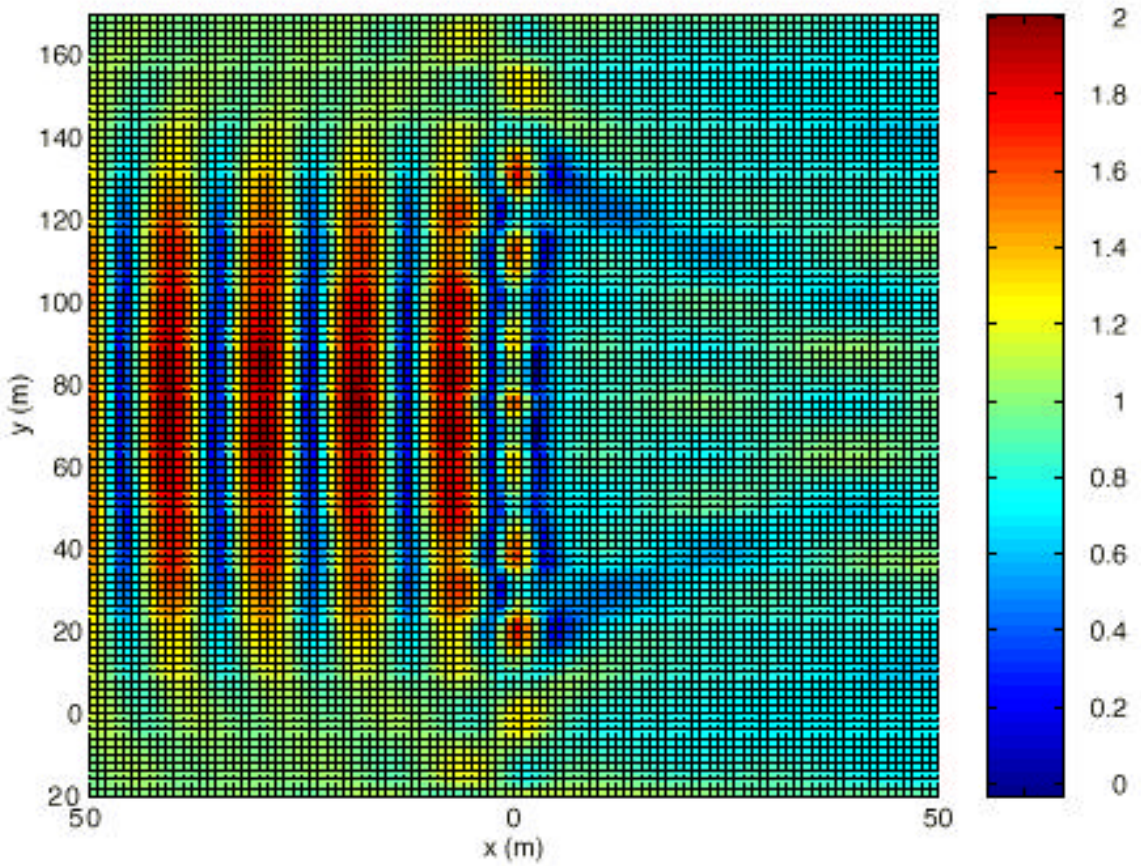

Figure 5.53 The amplitude of the free surface elevation for $\omega = \frac{\pi}{2}$ $\left(\beta = 0\right)$.

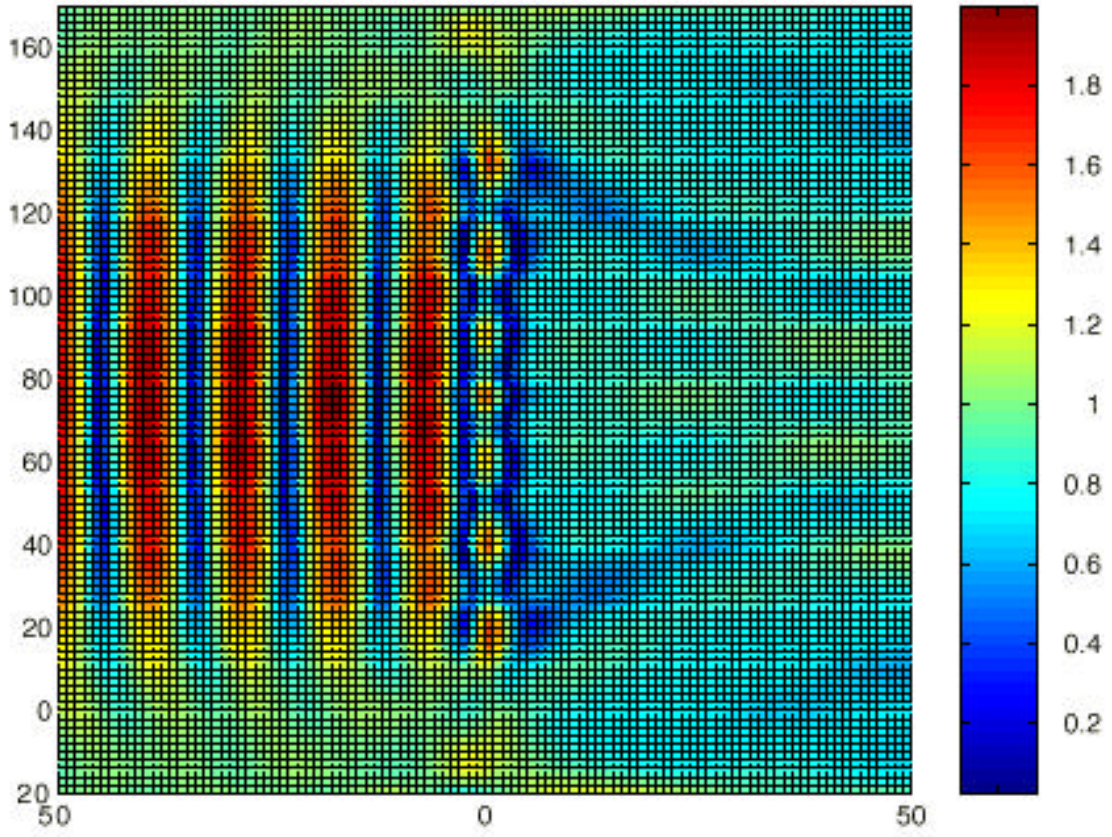

Figure 5.54 The amplitude of the free surface elevation for $\omega = \omega_{n=}\left(\beta = 0\right)$.

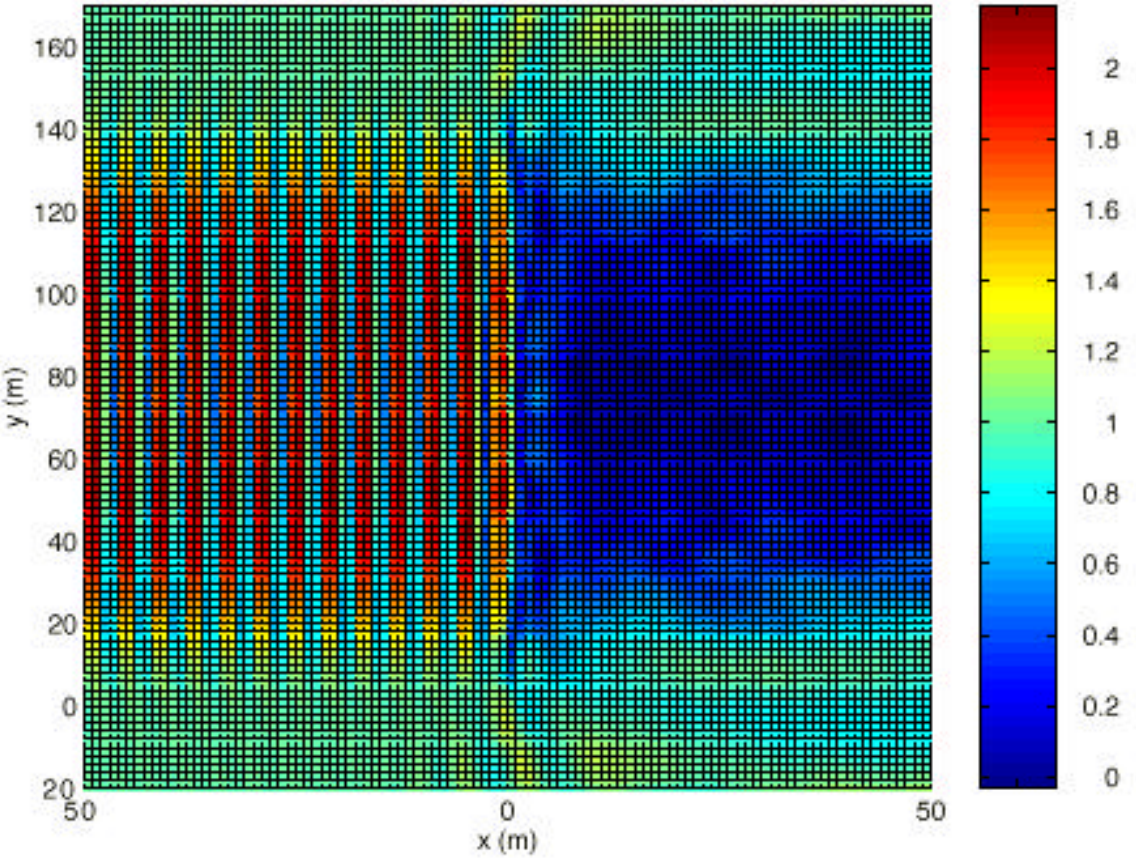

Figure 5.55 The amplitude of the free surface elevation for $\omega = \omega_{n_{max}} (\beta = 0)$.

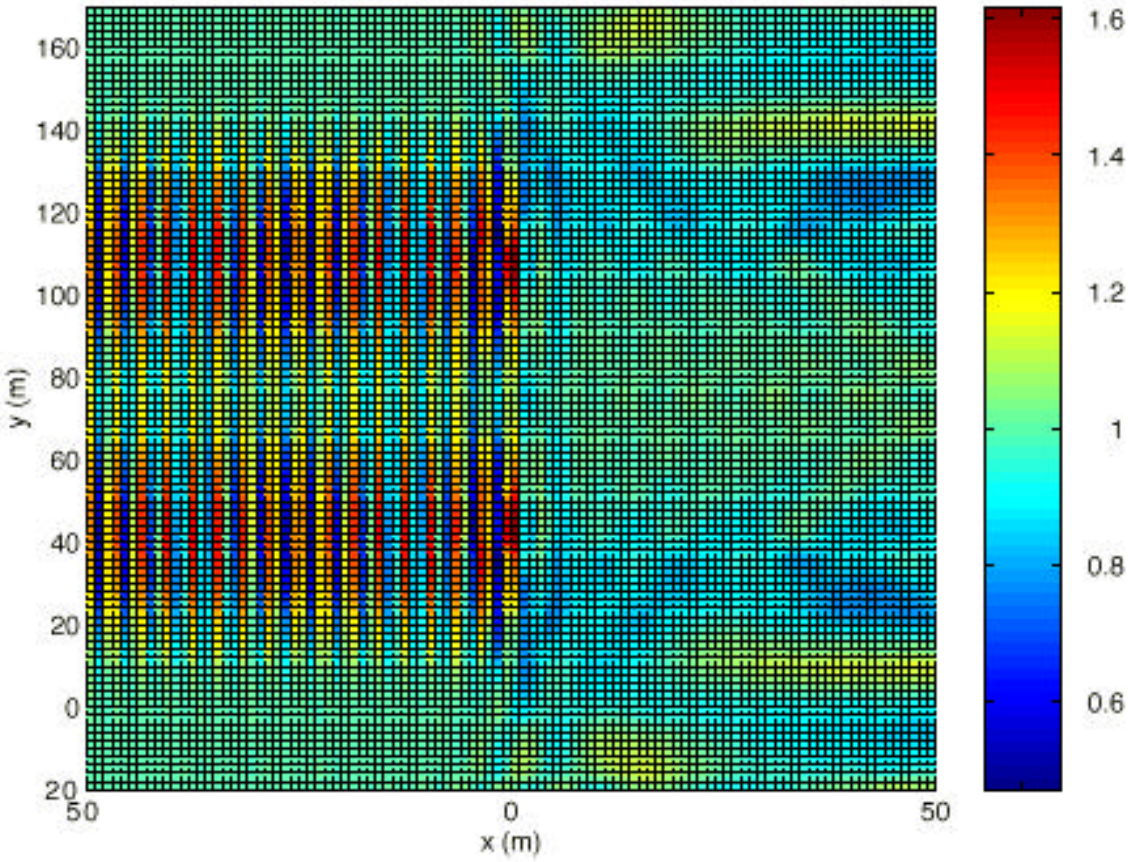

Figure 5.56 The amplitude of the free surface elevation for $\omega = \pi$ $(\beta = 0)$.

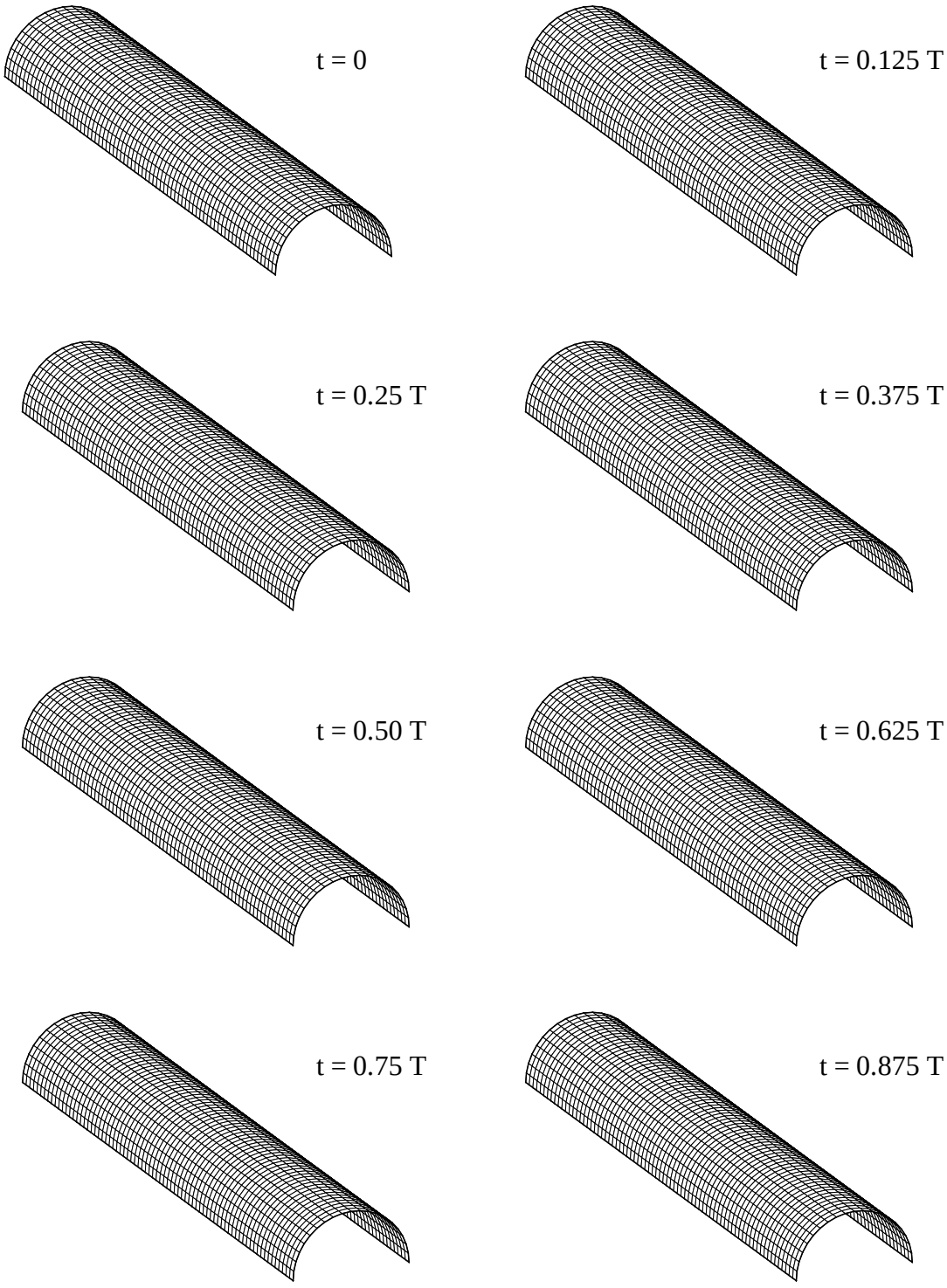

Figure 5.57 Displacements of structure over time for $A_{\text{incident}} = 1$ ($\omega = \omega_{n_1}$, $\beta = 0$).

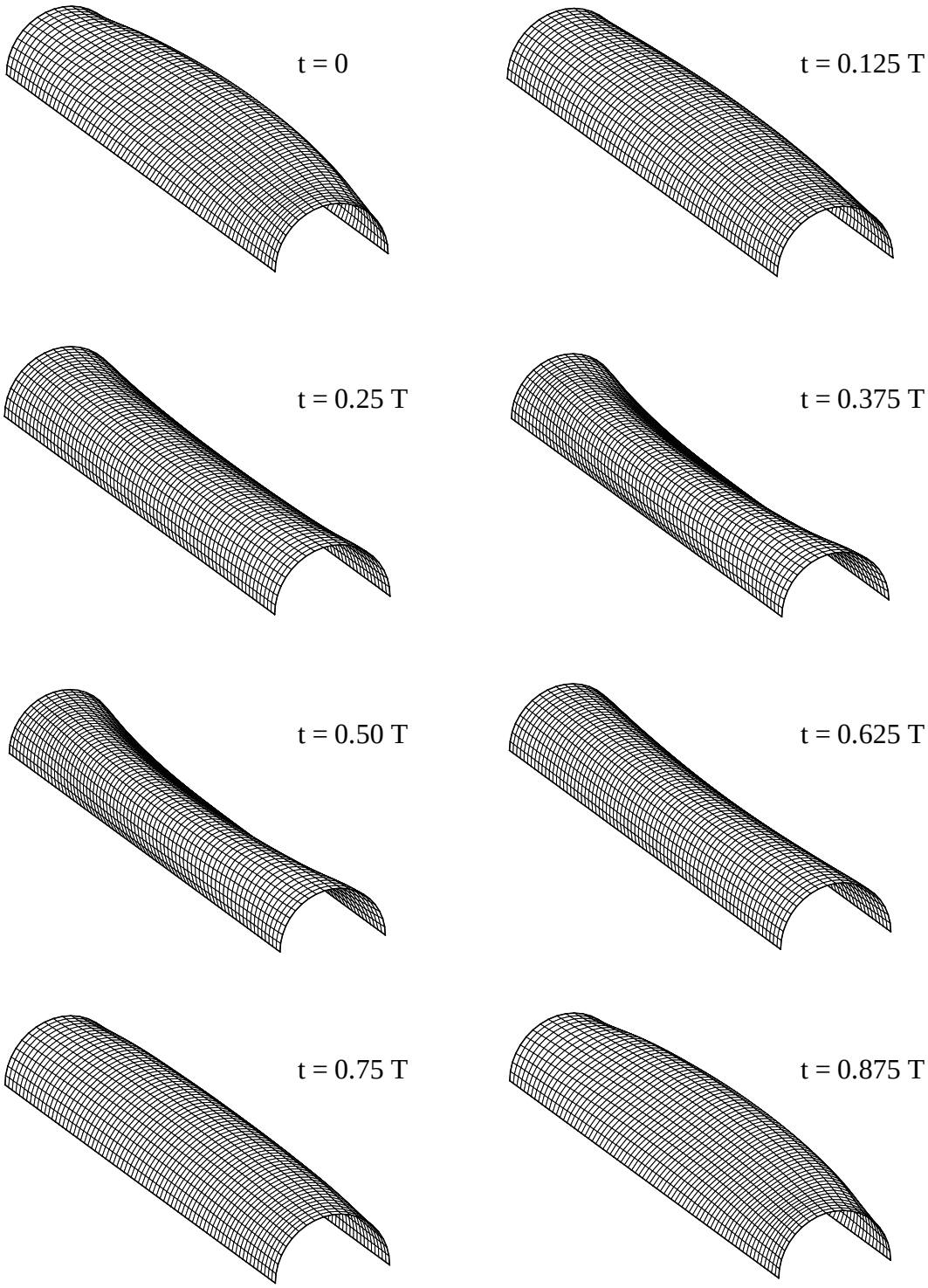

Figure 5.58 Displacements of structure over time for $A_{\text{incident}} = 1$ ($\omega = \frac{\pi}{4}$, $\beta = 0$).

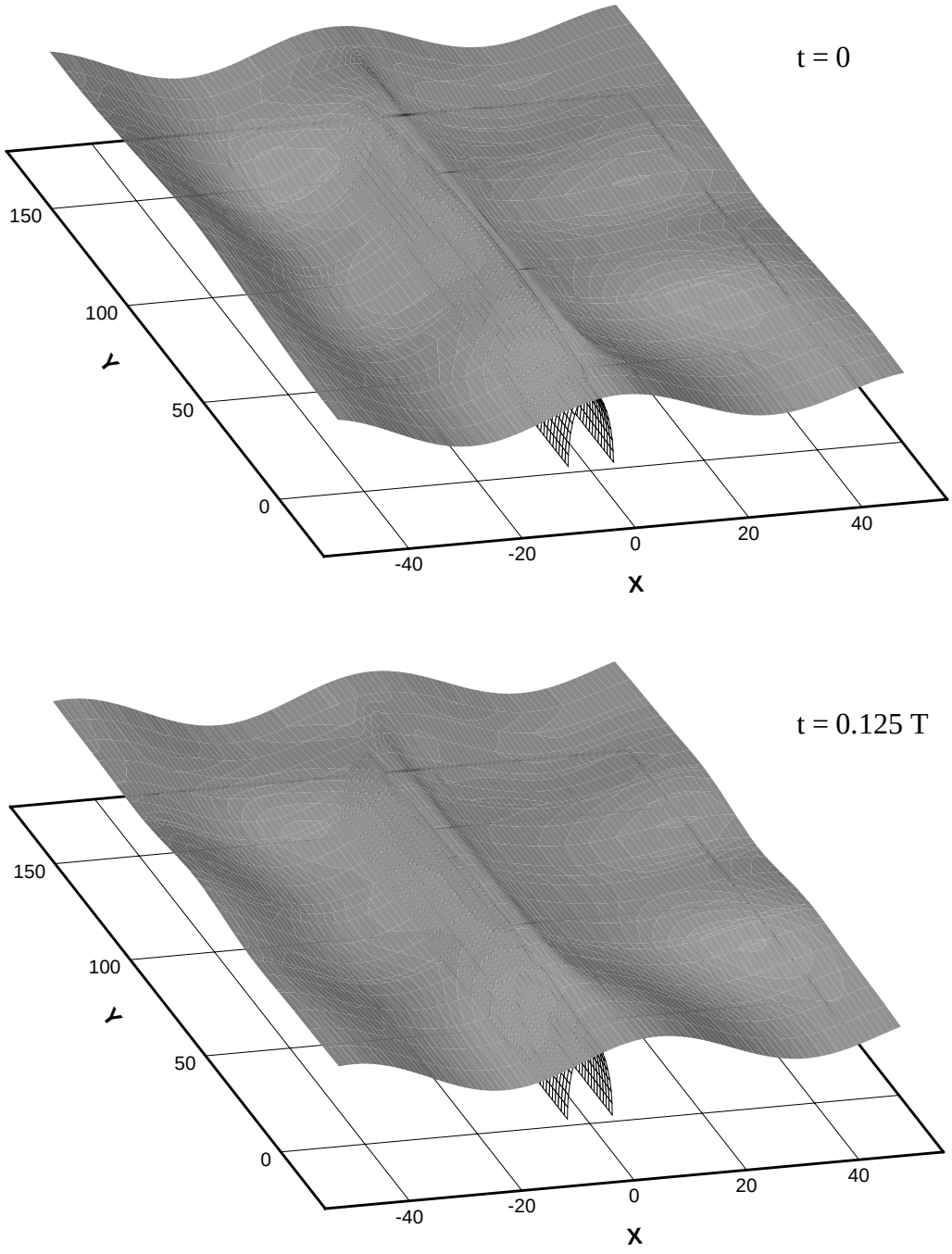

Figure 5.59.a Free surface elevation ($\omega = \frac{\pi}{4}$, $\beta = 0$).

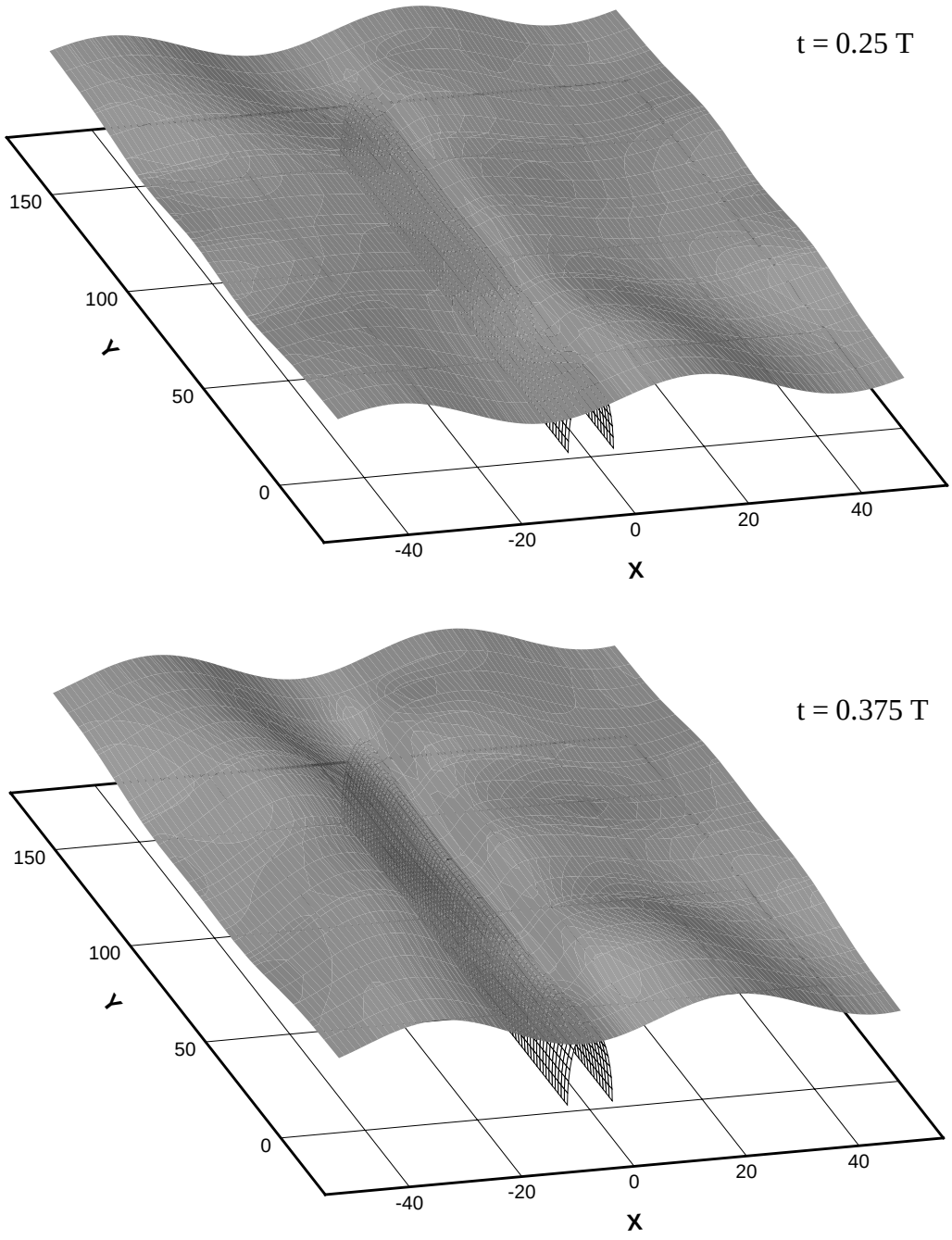

Figure 5.59.b Free surface elevation ($\omega = \frac{\pi}{4}$, $\beta = 0$).

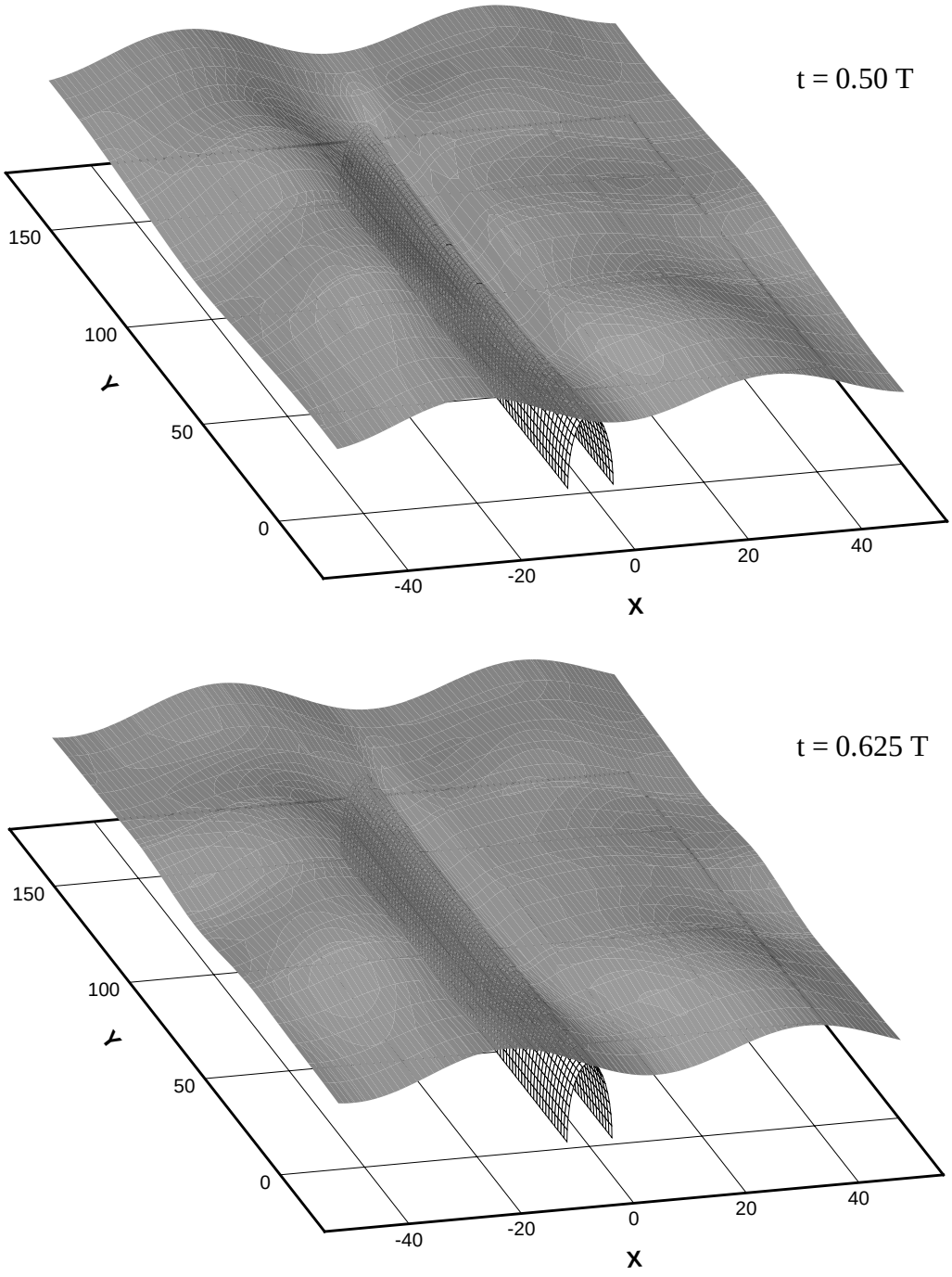

Figure 5.59.c Free surface elevation ($\omega = \frac{\pi}{4}$, $\beta = 0$).

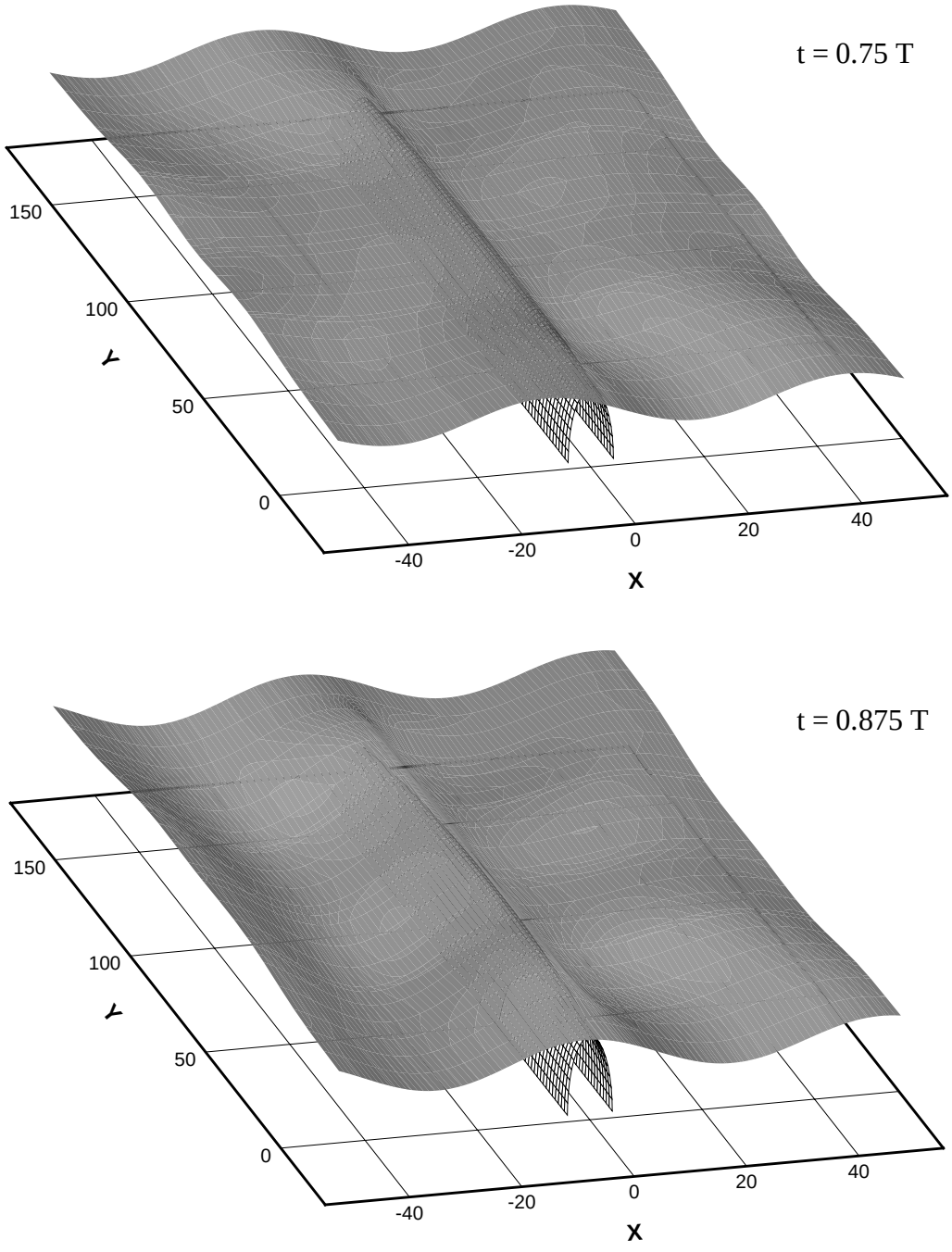

Figure 5.59.d Free surface elevation ($\omega = \frac{\pi}{4}$, $\beta = 0$).

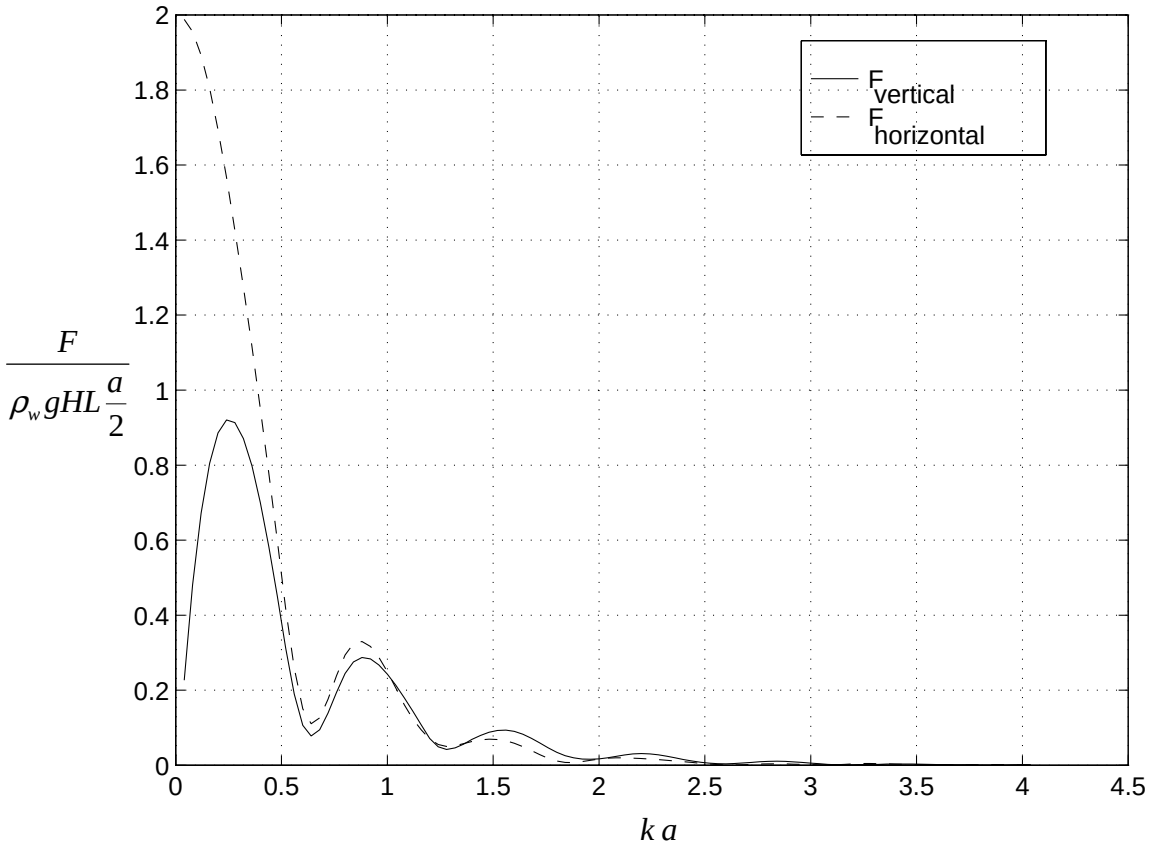

Figure 5.60 Hydrodynamic forces for the case of oblique incident waves, $\beta = 15°$.

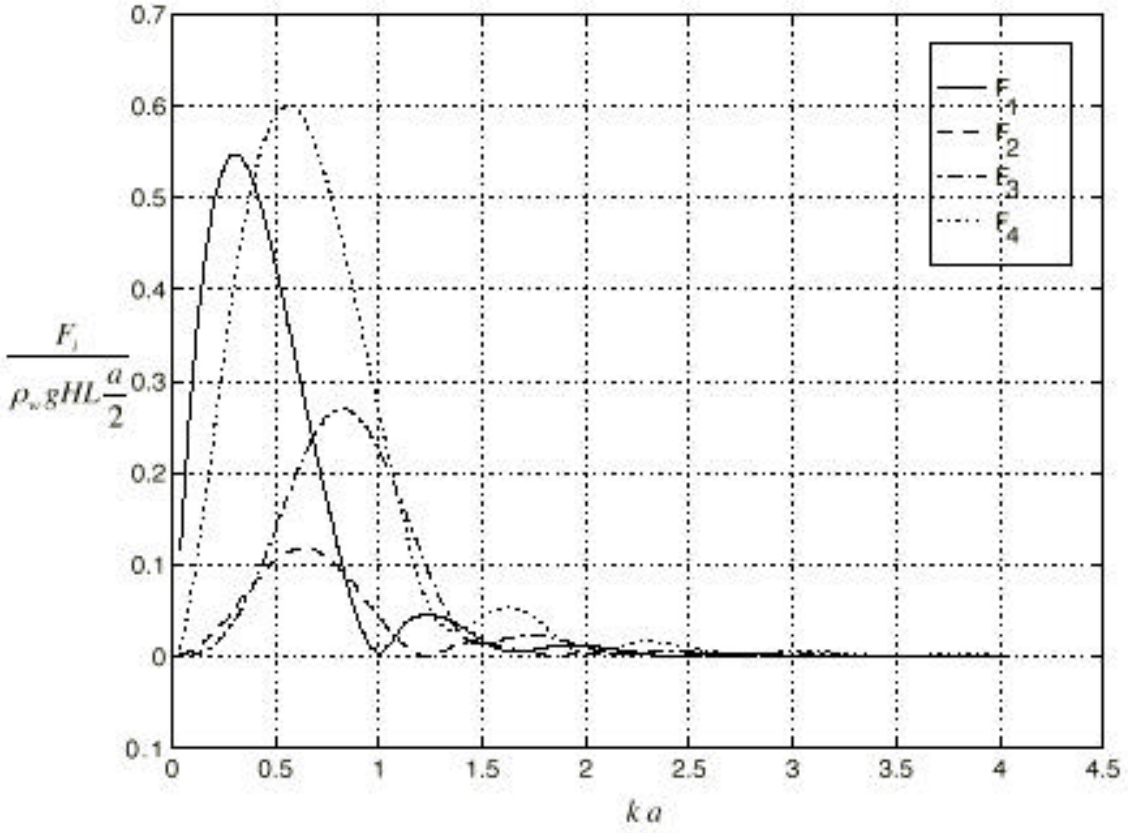

Figure 5.61 Hydrodynamic forces for modes 1, 2, 3 and 4 ($\beta = 15°$).

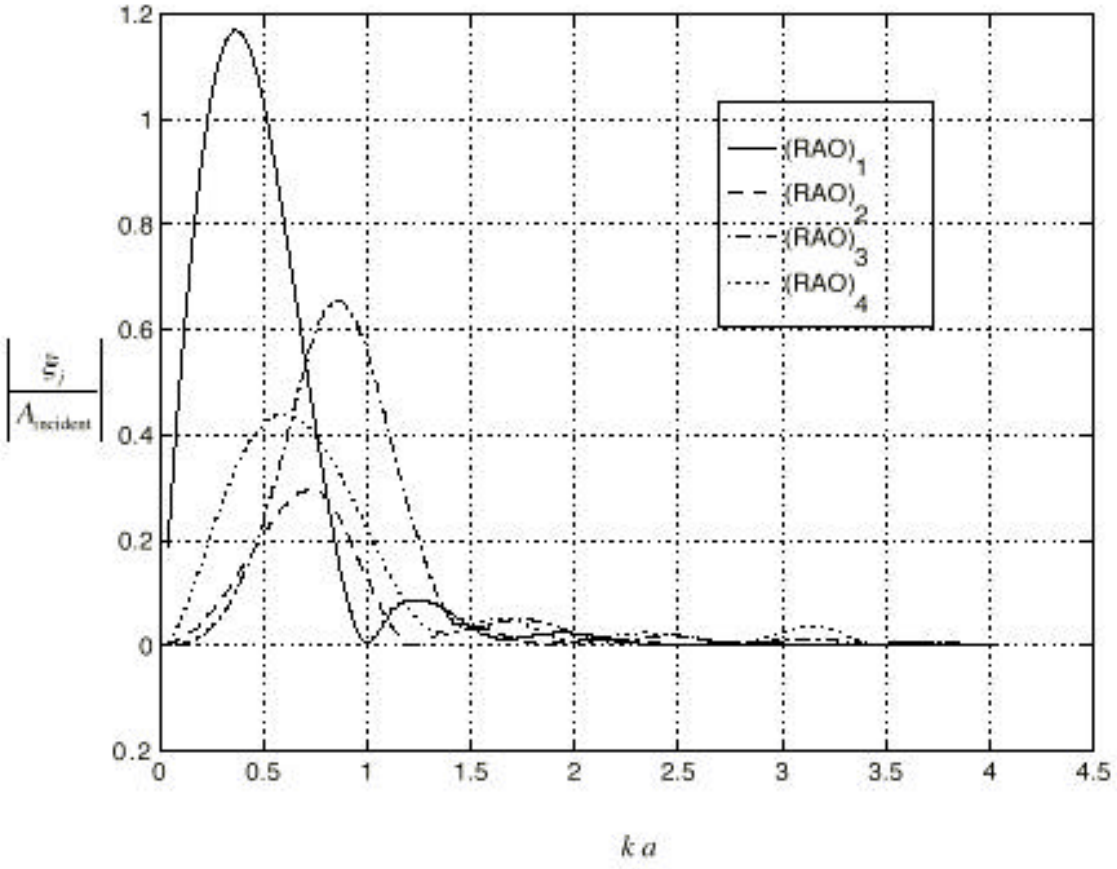

Figure 5.62 RAO for the case of oblique incident waves ($\beta = 15°$).

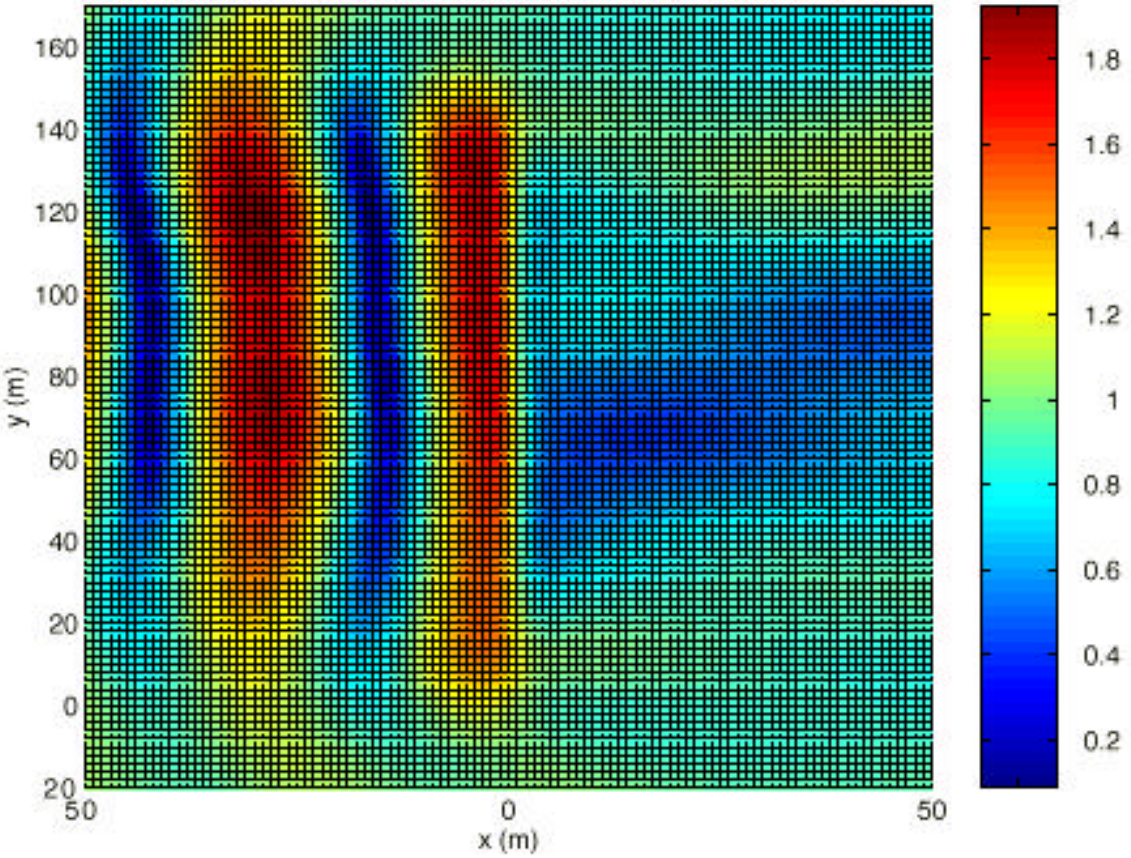

Figure 5.63 The amplitude of the free surface elevation for $\omega = \frac{\pi}{4}$ $(\beta = 15^{\circ})$.

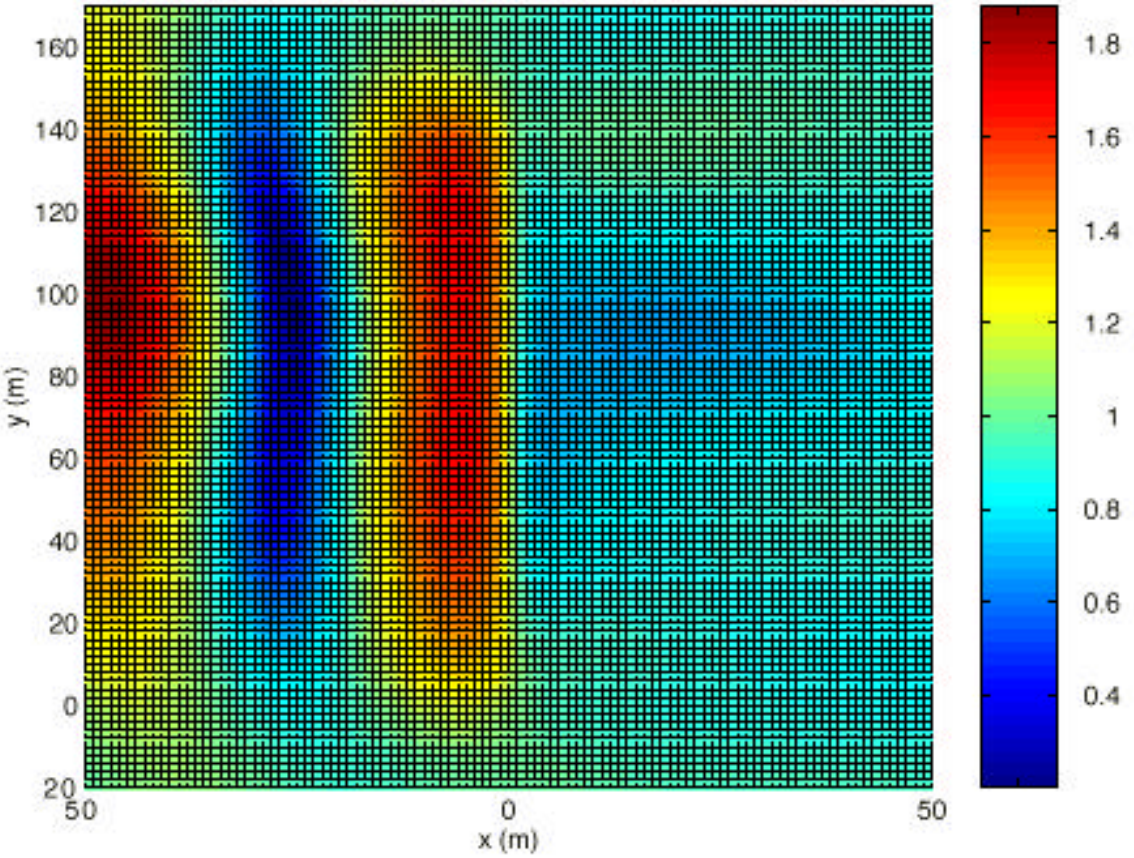

Figure 5.64 The amplitude of the free surface elevation for $\omega = \frac{\pi}{6}$ $(\beta = 15^{\circ})$.

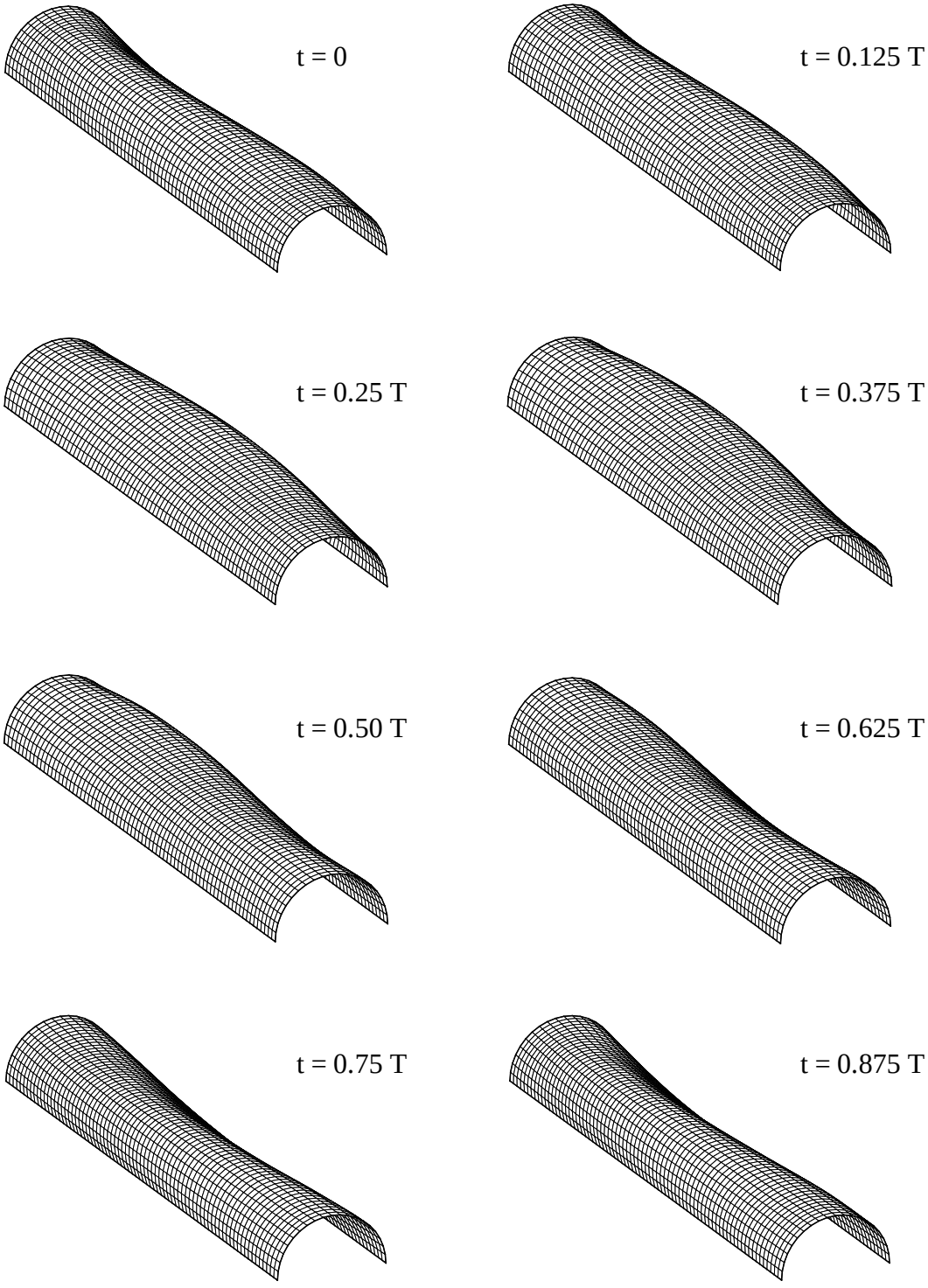

Figure 5.65 Displacements of structure over time for $A_{\text{incident}} = 1$ ($\omega = \frac{\pi}{4}$, $\beta = 15°$).

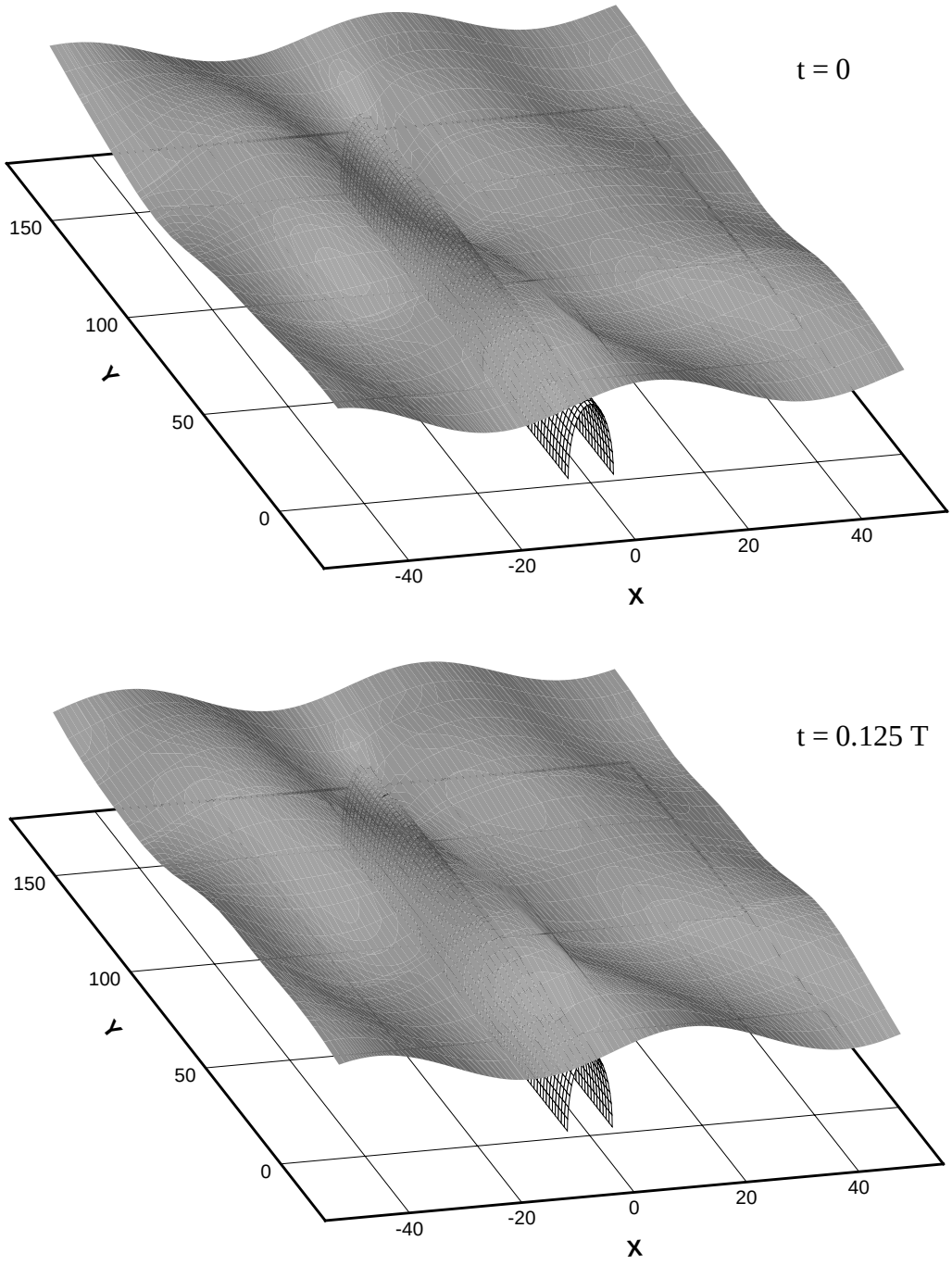

Figure 5.66.a Free surface elevation ($\omega = \frac{\pi}{4}$, $\beta = 15°$).

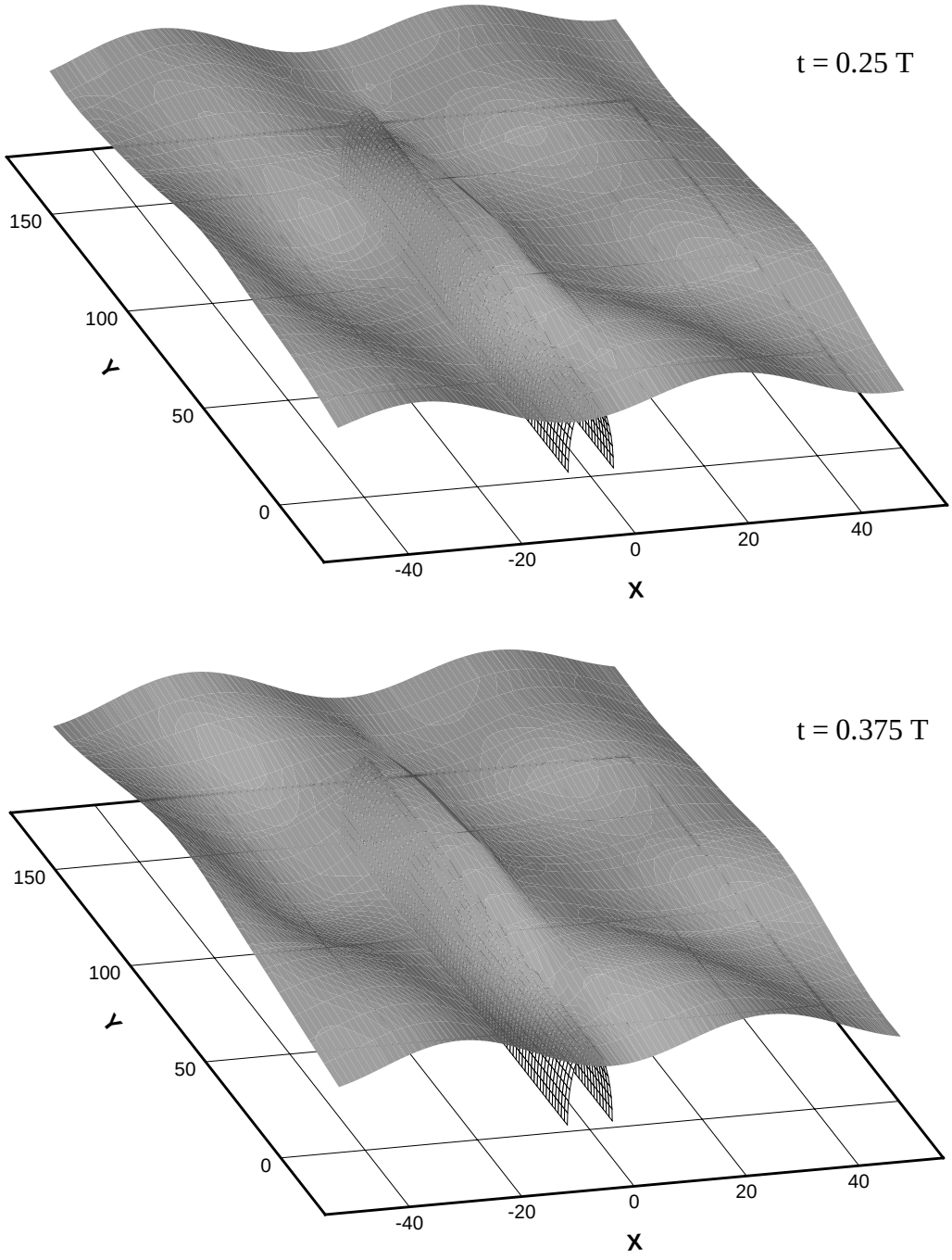

Figure 5.66.b Free surface elevation ($\omega = \frac{\pi}{4}$, $\beta = 15°$).

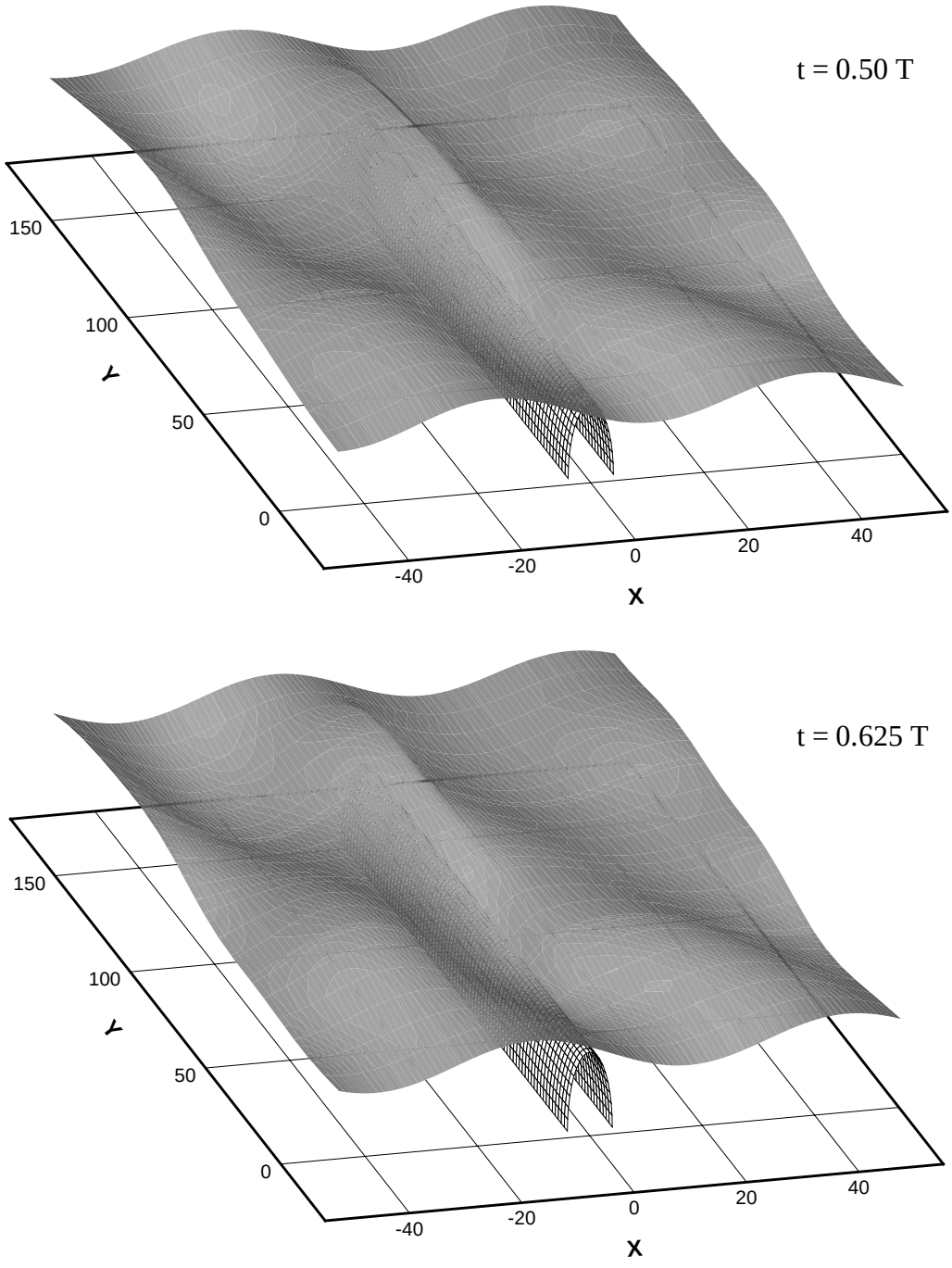

Figure 5.66.c Free surface elevation ($\omega = \frac{\pi}{4}$, $\beta = 15°$).

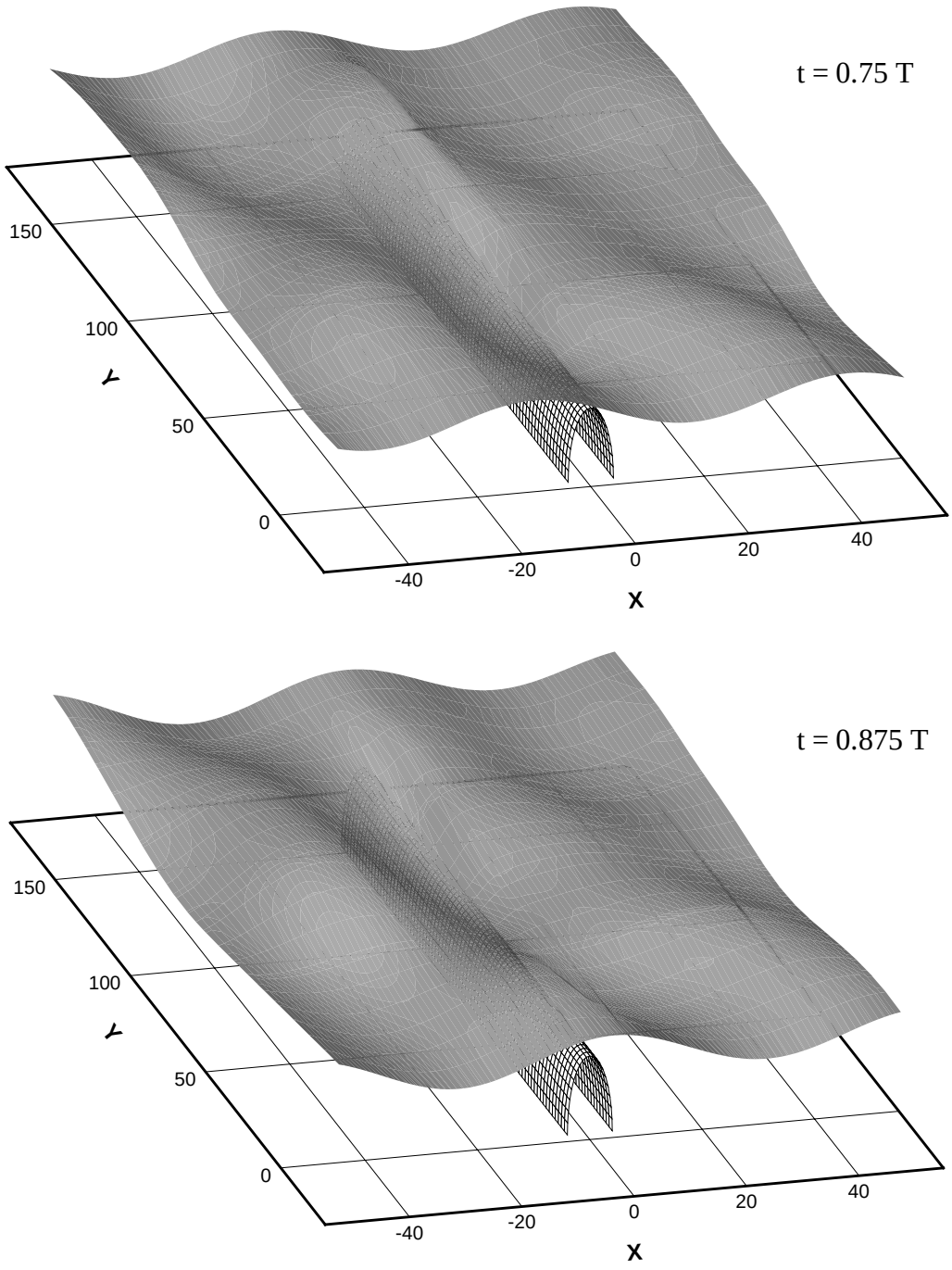

Figure 5.66.d Free surface elevation ($\omega = \frac{\pi}{4}$, $\beta = 15°$).

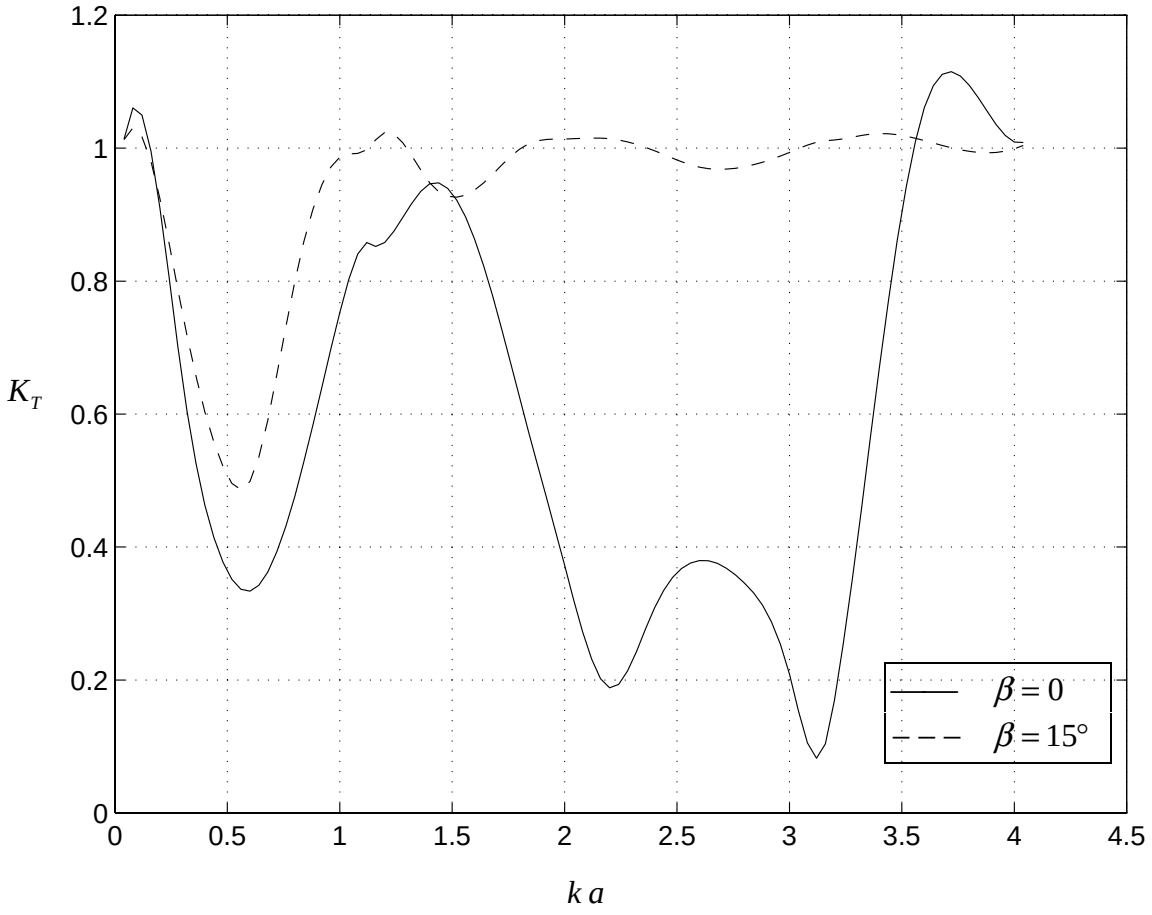

Figure 5.67 Transmission coefficients

CHAPTER 6 CONCLUSIONS

A three-dimensional numerical analysis has been performed to investigate the effectiveness of a flexible structure as a breakwater. Two different water depths, 6 m and 5 m, were considered. For each depth, the response to normal and oblique incident waves was analyzed.

The structure is an anchored hemicylinder filled with water. It was modeled as an elastic shell using the finite element program ABAQUS. For the analysis of the external and internal fluid flow, a boundary integral method was utilized and the integral equation was solved numerically by a panel method. The fluid was assumed to be inviscid and incompressible.

Vibration analysis of the structure was performed both in the absence and presence of water. It was found that the effect of water (e.g. added mass) is significant in reducing the magnitude of the natural frequencies. The mode shapes, however, do not change substantially.

For the case of a water depth of 6 m and normal incident waves, the flexible structure performs effectively in reducing the wave intensity for a wide range of wave frequencies. The reduction is found to be as much as 80% for the wave frequency $\omega = \omega_{n_1} = 1.4605$ rad/sec and 95% for the wave frequency $\omega = \omega_{n_2} = 2.465$ rad/sec. For the case of oblique incident waves, the structure is effective only for a small frequency bandwidth. As the incoming angle increases, the flexible structure becomes less effective.

For the case of a water depth of 5 m and normal incident waves, the structure is effective over certain ranges of wave frequencies. Outside these ranges, the structure does not move enough to generate waves that cancel the incoming waves. The reduction is found to be 80% for the wave frequency $\omega = \frac{\pi}{4}$ rad/sec and 95% for the wave frequency $\omega = \omega_{n_2} = 2.7753$ rad/sec. It is observed again that for the case of oblique incident waves, the structure is effective only for a small frequency bandwidth.

Future work may include changing the design parameters of the structure, such as the shell thickness, modulus of elasticity, or choice of material (e.g. composite material). Different shapes of the structure such as an elliptical cross section as well as a structure partially filled with water may also be considered.

REFERENCES

Broderick, L. L. and Leonard, J. W. (1992). "Nonlinear Water-Wave Structure Interaction," Computers & Structures, Vol. 44, No. 4, pp. 837-842.

Chakrabarti, S. and Naftzger, R. (1989). "Wave Forces on Hemicylinder," Ocean Engineering, Vol. 16, pp. 49-69.

Chidamparan, P. and Leissa, A. W. (1993). "Vibrations of Planar Curved Beams, Rings, and Arches," Applied Mechanics Reviews, Vol. 46, no. 9, pp. 467-483.

Dakshina Moorthy, C. M., Reddy, J. N. and Plaut, R. H. (1995). "Three-dimensional vibrations of inflatable dams," Thin-Walled Structures, Vol. 21, pp. 291-306.

Dean, R. G. and Dalrymple, R. A. (1991). Water Wave Mechanics for Engineers and Scientists, World Scientific, Singapore.

Evans, D. V. and Linton, C.M. (1989). "Active Devices for the Reduction of Wave Intensity," Applied Ocean Research, Vol. 11, No. 1, pp. 26-32.

Fathi, D. E., Lee, C. -H. and Newman, J. N. (1994). "Computation of Wave Induced Motions on a Flexible Container," Hydroelasticity in Marine Technology, O. Faltinsen et al. eds., A. A. Balkema, Rotterdam, pp. 301-308.

Firestone Coated Fabrics Company (1968). "Presenting the Imbertson Fabridam." Akron, Ohio.

Firestone Tire and Rubber Company (1964). "Fabridam General Report." Report No. 654-064-291, Akron, Ohio.

Grue, J. (1992). "Nonlinear Water Waves at a Submerged Obstacle or Bottom Topography," Journal of Fluid Mechanics, Vol. 244, pp. 455-476.

Hales, L. Z. (1981). "Floating Breakwaters: State of the Art Literature Review," Technical Report No. 81-1, Coastal Engineering Research Center, U.S. Army Corps of Engineers, Fort Belvoir, VA, October.

Hibbitt, Karlsson & Sorensen, Inc. (1994). "ABAQUS 1994," Theory Manual, Pawtucket, Rhode Island, Vol. I, Version 5.4.

Jenkins, C. H. and Leonard, J. W. (1991). "Nonlinear Dynamic Response of Membranes: State of the Art," Applied Mechanics Reviews, Vol. 44, pp. 319-328.

Jones, D. (1971). "Transportable Breakwaters - A Survey of Concepts," Technical Report No. R727, U.S. Navy Civil Engineering Laboratory, Port Hueneme, California, May.

Kobayashi, N. And Wurjanto, A. (1989). "Wave Transmission over Submerged Breakwaters," Journal of Waterway, Port, Coastal and Ocean Engineering, Vol. 115, pp. 662-680.

Kwak, M. K. and Kim, K. C. (1991). "Axisymmetric Vibration of Circular Plates in Contact with Fluid," Journal of Sound and Vibration, Vol. 146, pp. 381-389.

Mei, C. C. (1992). The Applied Dynamics of Ocean Surface Waves, World Scientific, Singapore.

Mei, C. and Black, J. (1969). "Scattering of Surface Waves by Rectangular Obstacles in Waters of Finite Depth," Journal of Fluid Mechanics, Vol. 38, pp. 499-511.

Newman, J. N. (1965). "Propagation of Water Waves Past Long Two-Dimensional Obstacles," Journal of Fluid Mechanics, Vol. 23, pp. 23-29.

Newman, J. N. (1985). "Algorithms for the Free-Surface Green Function," Journal of Engineering Mathematics, Vol. 19, pp. 57-67.

Newman, J. N. (1994). "Wave Effects on Deformable Bodies," Applied Ocean Research, Vol. 16, pp. 47-59.

Ohyama, T., Tanaka, M., Kiyokawa, T., Uda, T. and Murai, Y. (1989). "Transmission and Reflection Characteristics of Waves over a Submerged Flexible Mound," Coastal Engineering in Japan, Vol. 32, No. 1, pp. 53-68.

Scott, D. (1976). "Floodproofing Venice with Rubber Dams." Popular Science, Vol. 208, No. 3, March, pp. 76-78.

Shen, S., Shen, M. and Sun, S. (1989). "A Model Equation for Steady Waves Over a Bump," Journal of Engineering Mathematics, Vol. 23, pp. 315-323.

Soedel, W. (1993). Vibrations of Shells and Plates, Marcel Dekker, New York.

Sorensen, R. M. (1993). Basic Wave Mechanics for Coastal and Ocean Engineers, Wiley, New York.

Williams, A. and Darwiche, M. (1988). "Three-Dimensional Wave Scattering by Elliptical Breakwaters," Ocean Engineering, Vol. 15, pp. 103-118.

Wehausen, J. V. and Laitone, E. V. (1960). "Surface Waves", Handbuch der Physik, Vol. 9, pp. 446-778, Springer-Verlag Berlin.

VITA

Fata D.E. Dewi was born on January 13, 1972 in Surabaya, Indonesia. In 1995 she received the Bachelor of Science degree, *Cum Laude*, in Ocean Engineering from the Virginia Polytechnic Institute and State University. In August 1995, she started her master's program in Ocean Engineering at the Virginia Polytechnic Institute and State University under the guideance of Dr. Stergios I. Liapis and Dr. Raymond H. Plaut. Upon completing and receiving the Master of Science degree in August 1997, she will join an offshore structure company, Friede and Goldman, Ltd in New Orleans.